Development, Characterization, and Analysis of Silicon Microstrip Detector Modules for the CBM Silicon Tracking System

Zur Erlangung des akademischen Grades eines
DOKTORS DER NATURWISSENSCHAFTEN (Dr. rer. nat.)

von der KIT-Fakultät für Physik des
Karlsruher Instituts für Technologie (KIT)
angenommene

DISSERTATION

von

M. Sc. Pfistner, Patrick

Tag der mündlichen Prüfung:	02.07.2021
1. Referent:	Prof. Dr. Marc Weber
2. Korreferentin:	Prof. Dr. Alberica Toia

"Look deep into nature, and then you will understand everything better."

Albert Einstein

To my family

Abstract

The future Facility for Antiproton and Ion Research (FAIR) at GSI, Germany, will enable scientists to create tiny droplets of cosmic matter in the laboratory—matter subject to extreme conditions usually found in the interior of stars or during stellar collisions. The Compressed Baryonic Matter (CBM) experiment at FAIR aims to explore the quantum chromodynamics (QCD) phase diagram at high densities and moderate temperatures. Thus, it will complement investigations of the phase diagram at higher temperatures and lower densities conducted by the LHC and RHIC. Astronomically, the only known window into the speculated rich phases of cold and dense QCD are neutron stars and neutron star mergers. By colliding heavy ions at relativistic beam energies, the conditions inside these supermassive objects can be recreated for an exceptionally short amount of time. The CBM detector is a fixed-target multi-purpose detector designed for measuring hadrons, electrons and muons in elementary nucleon and heavy-ion collisions over the full FAIR beam energy range delivered by the SIS100 synchrotron.

One of the core detectors of CBM is the Silicon Tracking System (STS), responsible for measuring the momentum and tracks of up to 700 charged particles produced in a central nucleus-nucleus collisions. Due to the required momentum resolution of $\Delta p/p \approx 2\,\%$, the material budget of the STS must be minimized. Therefore, the readout electronics and the cooling and mechanical infrastructure are placed out of the detector acceptance. The double-sided silicon microstrip sensors are connected to the self-triggering frontend electronics using low-mass flexible microcables with a length of up to 50 cm. The technology of choice are fine-pitch aluminium-based microcables, which are a hightech product that is uncommon in industry. Hence, providing a sufficient microcable yield and throughput for series production is a non-trivial task. Consequently, the STS team was looking for alternative solutions.

The main goal of this thesis was to develop an alternative high-density interconnection technology based on copper microcables. We developed a low-mass double-layered copper microcable at the edge of modern fabrication technology. Despite the high mass of copper, the material budget of the copper microcable is only marginally larger compared to the aluminium microcable, while expressing a comparable parasitic capacitance. Based on the copper microcable, we developed a novel high-density interconnection technology, comprising fine-grain solder paste printing on the microcable and gold stud bumping on the die. The gold stud–solder technology combines a high automation capability with good mechanical and electrical properties, making it an interesting technology also for future detector systems. Building on the gold stud–solder technology, a fully customized bonder machine was developed and constructed in hardware and software. Its main purpose is the realization of the challenging interconnection between the microcable and the sensor. Key components of the machine are four step motors with a sub-micron step resolution, a dual-camera pattern recognition

system, a heatable, temperature-controlled bond head and sensor plate, as well as tailor-made mechanical supports for the STS detector modules. With the help of this bonder machine, a full-scale STS detector module in the copper technology was built. The noise performance of the copper module was evaluated in a bias voltage scan. Very low noise levels below 700 e^- were observed, in line with expectations. The channel yield of the module was estimated to be approximately 95 %. Measurements of the absolute value of the signal with a radioactive ^{241}Am-source allowed us to estimate the signal-to-noise ratio ($\sim$ 22) and charge collection efficiency ($\sim$ 91 %) of the module. The results of these measurements give us confidence that STS modules based on the copper technology can achieve a satisfying performance comparable to the modules built in the aluminium technology.

Besides the microcable, another essential component of the STS detector module is the frontend electronics chip. During this work, the version 2.1 of the STS-XYTER readout ASIC was extensively characterized. Noise discrepancies between odd and even channels and increasingly higher noise towards the higher channel numbers had been observed in the predecessor chip. Our measurements of the STS-XYTER2.1 verified that both issues were successfully resolved. Furthermore, the noise behavior of the ASIC with respect to input load capacitance was studied. This is essential to parametrize expected noise levels for the many kinds of detector modules employed in the STS, to which the measured noise levels can then be compared. Measurements of the noise levels as a function of shaping time showed that the overall noise level is practically independent of shaper peaking time. Radiation tests with 50 MeV protons and a total ionizing dose of 10 kGy were performed with copper microcables connected to the ASIC in a non-powered state. No indications of damage to the chip and interconnects could be observed.

Finally, a complete STS detector module in aluminium technology was subjected to a pencil-like monochromatic beam of 2.7 GeV/c protons at the Cooling Synchrotron at the research center Jülich. Several essential performance criteria of the detector module were evaluated. The best coincidence between the STS and the reference fiber hodoscopes was established based on time information. An excellent time resolution of a few nanoseconds could be demonstrated. Based on the best coincidence, the spatial resolution of the full system was determined to be a few hundred µm. This is in line with expectations, as the resolution is limited by the fiber hodoscope resolution. Charge distributions of 1-strip clusters showed a clear separation between the noise and the proton signal peak, with a signal-to-noise ratio above 20 for the p– and n-side. The charge collection efficiency of the module was estimated to be $\sim$ 96 %. The COSY beamtime enabled a first-time evaluation of the full analysis software chain with real data and the evaluation of the full electronic readout chain of STS. The experience gained at COSY is immensely helpful for commissioning and data analysis in more complex beam environments such as mCBM, where a subsample of the CBM detectors is exposed to the particles created in a heavy-ion collision in run-time scenarios closely resembling the final CBM environment.

Acknowledgements

"No act of kindness, no matter how small, is ever wasted."
Aesop

With this, a challenging and formative period of my professional and personal life is coming to an end. First and foremost, thank you Sina. Thank you for your immeasurable support and enduring me during those not always ordinary times. I am forever grateful that you helped me become the person I am today. Thanks to my family for teaching me—among other things—the values of hard work, personal responsibility, honesty, and enjoyment.

I want to thank Prof. Dr. Marc Weber for giving me the opportunity to conduct this PhD thesis, the trust in my work, and the valuable comments on my writings. Thanks to Michele and Thomas for being role models in dedication and helping me to grow as a person. Thanks to my students for contributing to this project and allowing me to guide them during their time at IPE. Thank you Lars for numerous enlightening discussions, be it on a professional or very personal level. Thank you Michael for always exciting conversations.

To Johann Heuser and the whole STS team at GSI, I appreciate how you received me and made my integration into the team easy and uncomplicated. I am highly grateful for the welcoming nature of Prof. Dr. Alberica Toia and her sustained and detailed efforts to support me in the COSY beamtime data analysis. To the Cuban office in KBW. It was such a pleasure to meet you. Osnan and Anton, thank you for sharing the time and your help in the detector lab. Anton, thank you for reading parts of the manuscript. Adrian, there is not enough space here to describe how much you contributed in so many ways to this. Without you, this work would not be the same. Gracias, chamaco!

For the technical support at IPE, I must thank Benjamin Leyrer, Bernhardt Osswald, Tibor Piller, and Peter Schöck. Thanks to Pia Steck for quick and uncomplicated wire bonding support while the IPE bonding machine was broken. For the technical assistance at GSI and the coordination of supply and transport of essential material to KIT, many thanks to Carmen Simons.

Finally, to the people I forgot to mention that helped me walk this walk in visible and not so visible ways, thank you.

Contents

1 The Physics of CBM—A Brief Introduction

Understanding the creation and evolution of the universe is one, if not the, fundamental question at the heart of science. To our current knowledge, there are four fundamental forces of nature: the strong, weak, electromagnetic, and gravitational force. Nowadays, the combination of theoretical advances and increasingly sophisticated particle detectors enables the quantitative description of physical phenomena spanning a length scale of 40 orders of magnitude—a remarkable achievement thanks to many generations of scientists. Apparently, all matter is made from tiny fundamental building blocks—the elementary particles—whose interaction is governed by the four fundamental forces. Still, the majority of the universe is invisible to us, unexplicable with current theories—the mysterious dark matter and dark energy.

Beyond that, nuclear matter at high densities and moderate temperatures is still poorly understood. Astronomically, the only known window which allows studying this phase space region is neutron stars and neutron star mergers. Fortunately, cold and high-density matter can be created in the laboratory by colliding heavy ions at relativistic beam energies. The CBM experiment will perform systematic multi-differential measurements of almost all particles produced in nuclear collisions with unprecedented statistics. The dominant force determining the system evolution in such collisions is the strong force, which is described by quantum chromodynamics (QCD).

This chapter briefly introduces QCD and the QCD phase diagram in section 1.1, followed by the description of nuclear matter at high densities in section 1.2. The evolution of a heavy-ion collision is detailed in section 1.3. The FAIR research center is presented in section 1.4. Finally, the chapter is completed by portraying the physics program of CBM in section 1.5.

1.1 QCD and the QCD phase diagram

The Standard Model of elementary particle physics comprises the current state of knowledge of particle physics. It is a quantum field theory that includes all known elementary particles as well as three fundamental interactions—the electromagnetic, weak, and strong interaction. The relatively weak gravitation is not described.

Quantum chromodynamics (QCD) is the modern theory of the strong interaction [1]. QCD is a quantum field theory based on the non-Abelian gauge group SU(3). The fundamental degrees of freedom are quarks and gluons, together called partons. Partons carry color (greek:

chroma) charges, giving the theory its name. Color confinement binds the partons into color-neutral baryons (three quarks, qqq) and mesons (quark–antiquark, q$\bar{q}$), together called hadrons. Gluons are the massless gauge bosons of QCD. Gluons are fundamentally different to the photon, the gauge boson of the electromagnetic interaction, in that the gluons carry color charge whereas photons do *not* carry electric charge [1]. Hence, the gluons self-interact, which ultimately results in the non-commutative nature of QCD and makes QCD quite more involved than QED. A unique feature of the strong interaction is the so-called running coupling 'constant', which to the first order is given by [2]

$$\alpha_s = g^2/4\pi = \frac{4\pi}{\beta_0 \ln \frac{Q^2}{\Lambda^2_{QCD}}} . \tag{1.1}$$

Here, Λ_{QCD} is the QCD scale parameter which depends on the chosen renormalization scheme [2]. Indeed, α_s is not constant but shows an inverse logarithmic dependence on the resolution scale or momentum transfer Q. The β-function controls the scale dependence of the strong coupling and can be expressed as a perturbative series with coefficients β_n. The value of the first term in the series is $\beta_0 = 11 - \frac{2}{3}n_f$, with the active number of quark flavors n_f at the scale Q^2. The negative overall sign), combined with the fact that $\beta_0 > 0$ (for $n_f < 16$), leads to the famous result that the QCD coupling effectively decreases with energy [3].

Figure 1.1 displays a summary of measurements of α_s [4]. At a given order in a given renormalization scheme, $\alpha_s(Q^2)$ can be fully characterized either by giving the value of α_s at a conventional scale, usually the Z boson mass $Q^2 = M_z^2$, or by giving the value of Λ_{QCD}. At low energies or correspondingly large distances the coupling increases. This is the non-perturbative sector of QCD. Towards higher energies (shorter distances), the coupling ultimately becomes small enough to allow an expansion of the QCD Lagrangian in orders of α_s, and apply perturbation theory. For $Q^2 \longrightarrow \infty$, QCD will asymptotically transition into a field-free theory, i.e. the quarks can be seen as asymptotically free particles. The discovery of asymptotic freedom in the early 1970s was rewarded with a Nobel Prize in 2004 [5, 6].

Experimental verifications of QCD include that partons are indirectly observed in deep inelastic scattering, the corresponding structure functions show scaling violation, and partons manifest themselves through jet production. Yet, the theory is still poorly understood in the non-perturbative regime at low energies or large distances [7]. There, due to the non-negligible value of α_s, perturbative methods are no longer applicable.

In order to describe the states of strongly interacting matter, it is helpful to look at the QCD phase diagram, illustrated in Figure 1.2 on page 4. Here, the temperature T is plotted versus the baryochemical potential μ_B, a measure of the net-baryon density, i.e. baryon density minus antibaryon density. In the lower left, at low T and low μ_B, partons are bound to form hadronic matter. Hadrons have an intrinsic size with a radius $r_h \approx 1\,\mathrm{fm}$, occupying a corresponding volume $V_h \approx 4\pi/3 \cdot r_h^3$. Hence, from simple geometrical considerations results a nuclear saturation density of $n_0 \approx 0.16\,\mathrm{fm}^{-3}$. At 0 K, nucleons are present only above $\mu_B \sim m_N = 0.938\,\mathrm{GeV/c^2}$—the nucleon mass.

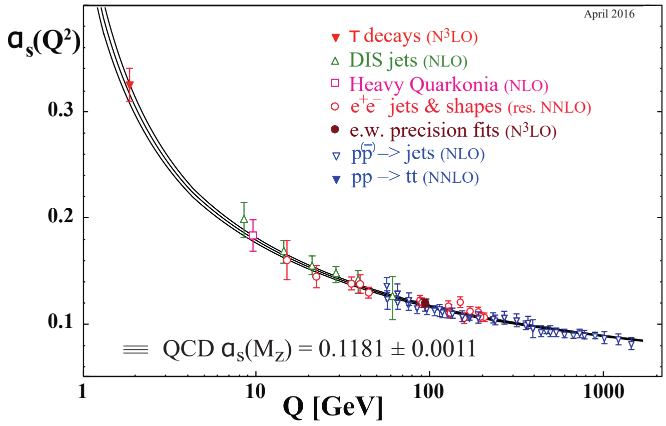

Figure 1.1: Summary of measurements of α_s as a function of the energy scale Q. The QCD prediction uses the world average of α_s, measured at the Z boson mass. From [4].

The upper left part of the phase diagram resembles the situation a few microseconds after the Big Bang, with extremely high temperatures and equal number of baryons and antibaryons, $\mu_B \approx 0$. For vanishing μ_B, QCD can be evaluated on a regularized lattice with Lattice QCD (LQCD) methods [7]. LQCD predicts a smooth 'crossover' phase transition (PT) from confined hadronic matter to a deconfined color-conducting quark–gluon plasma (QGP) at around 154 MeV [8], coincident with chiral symmetry restoration. Experiments at BNL-RHIC (7.7 GeV $< \sqrt{s_{NN}} <$ 200 GeV) and CERN-LHC ($\sqrt{s_{NN}} \leq$ 5.5 TeV) have investigated this phase space region and successfully created a QGP [9, 10, 11]. The extracted freeze-out temperatures for LHC data are 156 MeV, in perfect agreement with the LQCD predictions [12].

For finite μ_B, LQCD suffers from the fermionic sign problem, the standard Monte Carlo methods are not applicable and no clear predictions on PTs are possible [13]. At finite μ_B, effective-model calculations predict a rich structure in the phase diagram. These include a first-order PT merging into a critical endpoint [14]. The right panel of Figure 1.2 shows the expected PT region as probed by various experiments. Next to the confinement–deconfinement PT, a chiral PT is predicted [15]. At low T and low μ_B, chiral symmetry breaking is caused by the chiral condensation of paired quarks and antiquarks with different chirality. The chiral condensate is characterized most simply by a non-vanishing chiral condensate $\langle \bar{q}q \rangle$ (q is the quark field). It is largely responsible for the hadron masses and the existence of the nearly massless Nambu–Goldstone bosons, such as the pion and kaon [16].

In the deconfined phase at high enough temperatures, chiral symmetry restoration is expected, albeit only approximately. QCD matter at high densities will be discussed in more detail in the following section.

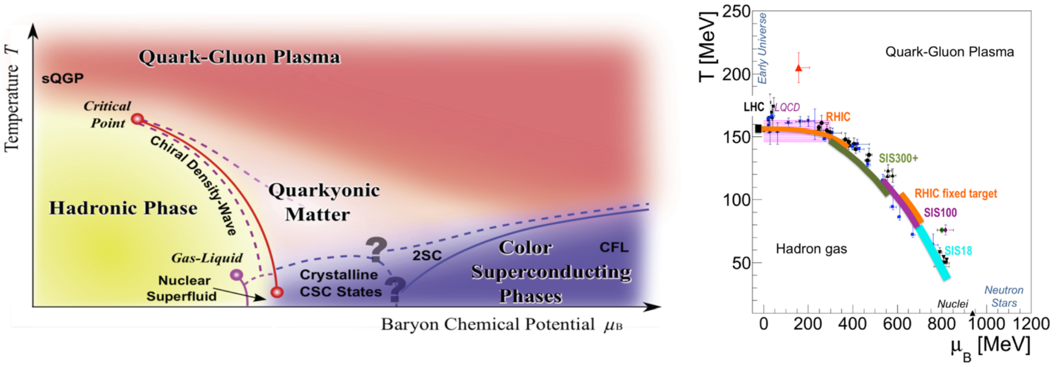

Figure 1.2: Left: The QCD phase diagram. Figure taken from [17]. Right: The PT region as probed by various heavy ion collision experiments. The region of applicability of LQCD is indicated by the purple band. The red triangular data point is from the NA60 collaboration and corresponds to a measurement of fireball temperature extracted from a dilepton invariant mass spectrum. Figure taken from [18].

1.2 QCD matter at high densities

As mentioned above, for finite net-baryon densities, or finite μ_B, and small to moderate temperatures, the QCD phase diagram is predicted to exhibit a rich structure. This includes a first-order PT between the partonic and hadronic phase ending in a conjectured critical endpoint, where strong fluctuations of physical parameters are expected to occur. Theory also speculates about exotic intermediate phases such as quarkyonic matter which has properties of both high-density baryonic matter and deconfined, chirally symmetric quark matter [19].

Staying on the chemical potential axis while going to higher densities (compression without heating) leads into yet another unexplored region in phase space. Even at very low temperatures, sufficiently dense matter cannot be thought of as well-separated nucleons. QCD color-magnetic interactions favor the formation of a diquark condensate of quark pairs—characterized by a non-vanishing expectation value $\langle qq \rangle$—similar to the condensate of electron pairs in a superconductor, hence forming a color superconductor [20, 21].

Astronomically, high net-baryon densities occur in neutron star cores or during neutron star mergers. Matter in neutron stars lives essentially along the chemical potential axis ($T \sim 0$). The exception is during neutron star births in supernovae, where temperatures can be of the order of 10 MeV, and in final gravitational mergers where temperatures could reach 102 MeV [22]. Thus, neutron stars are the only known window into the rich structure of cold and dense QCD, providing a vast testing ground for microscopic theories of dense nuclear matter. Neutron stars provide a complementary approach to probing dense matter at increasingly high temperatures in relativistic to ultrarelativistic heavy ion collision (HIC) experiments at the future CBM experiment at FAIR, and existing facilities such as RHIC or LHC.

The existence of massive neutron stars has important implications for dense matter in QCD. For example, they require a stiff equation of state and at the same time impose severe constraints

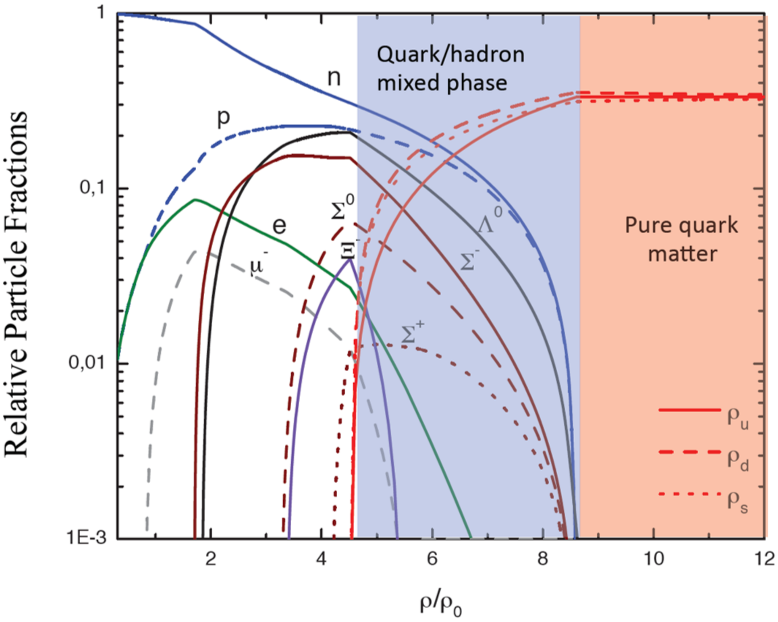

Figure 1.3: Particle population in a neutron star calculated with a n3NJL model with repulsive vector interactions. Besides the hadronic phase and the quark matter phase, a mixed phase is expected for intermediate densities. Figure taken from [23].

on the possible phases of dense QCD matter. In particular, massive neutron stars are difficult to explain in the context of hadronic models of neutron star matter in which the emergence of strange hadrons around twice nuclear saturation density softens the equation of state and limits the maximum stable star mass.

Figure 1.3 shows the relative particle fractions over density in a neutron star, calculated with a Nambu Jona-Lasinio model [23] (n3NJL, replacing the full QCD interactions with effective quark-quark interactions, while at the same time suppressing explicit gluonic degrees of freedom) with repulsive vector interactions [23]. The model predicts a mixed phase of hadrons and quarks in the intermediate-density regime ($4.5\,\rho_0 < \rho < 8.5\,\rho_0$) in between hadronic matter at low densities and pure quark matter at very high densities. Moving from low to high densities one expects in dense matter a gradual onset of quark degrees of freedom not accounted for by nucleons interacting via static potentials. Figure 1.4 illustrates how, at a sufficiently high density, the matter should percolate in the sense that their quark constituents are able to propagate throughout the system [24, 25, 26].

1.3 Heavy-ion collisions as a means to study QCD matter

The terrestrial means to generate sufficiently high–energy density and high-temperature matter for creation of the QGP is to collide heavy ions at relativistic (0.1 AGeV < E_{beam} < 10 AGeV) or ultrarelativistic (E_{beam} > 10 AGeV) energies. The space-time picture of the

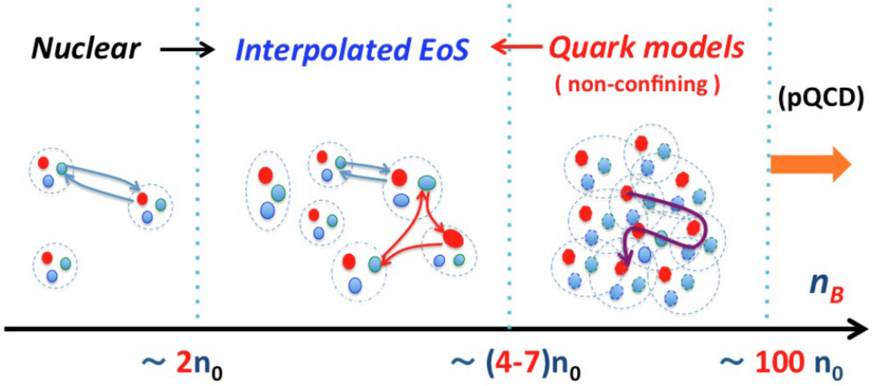

Figure 1.4: Schematic picture of the deconfinement phase transition with increasing density. (i) For $n_B \lesssim 2n_0$, the dominant interactions occur via a few ($\sim 1-2$) meson or quark exchanges and description of the matter in terms of interacting nucleons is valid; (ii) for $2n_0 \lesssim n_B \lesssim (4-7)n_0$, many-quark exchanges dominate and the system gradually changes from hadronic to quark matter; (iii) for $n_B \gtrsim (4-7)n_0$, the matter is percolated and quarks no longer belong to specific baryons. A perturbative QCD description is valid only for $n_B \gtrsim (10-100)n_0$. From [22].

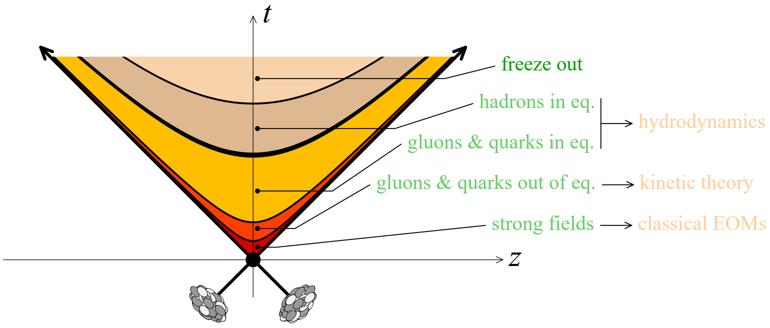

Figure 1.5: The expected space-time picture for a relativistic heavy-ion collision showing the successive stages of system evolution and the most widely used approaches to describe each stage. From [27].

evolution of a heavy-ion collision is shown in Figure 1.5. It is important to note that the dynamics of the system evolution strongly depend on the center-of-mass energy $\sqrt{s}$. For top RHIC energies and beyond ($\sqrt{s_{NN}} \geq 200$ GeV), the incoming nuclei are highly Lorentz-contracted and move in opposite directions at almost the speed of light. For these extreme beam energies, each incoming nucleus can be looked upon as a coherent cloud of partons or a color-glass-condensate (CGC) plate [28]. At proper time $\tau = \sqrt{t^2 - z^2} = 0$, the two nuclei have the first contact. The collision results in shattering of the two CGC plates. A significant fraction of the incoming kinetic energy is deposited in the central region. This leads to a high–energy density fireball—a highly non-equilibrium state called glasma [28, 29]. At top RHIC energies, the target-projectile interpenetration time is $2R/\gamma = 0.12\,\mathrm{fm/c}$ ($R \propto A^{1/3}$, $\gamma \sim 100$) [7]. The initial hard parton-parton collisions ($Q^2 >> \Lambda_{QCD}$) occur at very early times $\tau \approx \sqrt{1/Q^2}$ and lead to inelastic perturbative QCD (pQCD) shower multiplication. This pQCD shower formation by hard parton scattering settles at about 0.25 fm/c. The next phase, often called pre-equilibrium phase, is where the bulk of the (softer) initial parton-parton collisions occur. It is characterized by a pile-up of partonic energy density at mid-rapiditiy. The collisions among partons lead to a locally thermalized medium with deconfined quarks and gluons, the QGP. This happens at a time of the order of $\tau \approx 1$ fm/c. The pre-equilibrium phase and the mechanism that leads to rapid thermalization is still not fully understood and might happen through instabilities in the weakly coupled, strongly interacting glasma [30]. In Pb–Pb collisions at $\sqrt{s_{NN}} = 5.5$ TeV at the LHC, the initial valence quarks amount to only 5 % of the total quark density, so μ_B is very small [7].

Moving to lower collision energies, the picture changes drastically. At top SPS energy ($\sqrt{s_{NN}} = 17.3$ GeV), global interpenetration takes as long as 1.5 fm/c, much longer than microscopic shower formation time. Hard QCD mechanisms are thus convoluted with this interpenetration phase. Only after 2–3 fm/c one can think of global states such as local or global equilibrium, shortly before bulk hadronization. At SPS energies and below, hard particles are essentially only produced in the primary collisions between the projectile and target nucleons; the bulk of the produced particles have transverse momenta below 2 GeV/c and are too soft to produce hard particles via secondary collisions. At SPS energies, the 'hardest' particles which can be produced and well identified by their distinctive decay pattern are $c\bar{c}$ pairs [31]. In a heavy-ion collision with a center-of-mass energy $\sqrt{s_{NN}} = \mathcal{O}(10\,\mathrm{GeV})$, the created fireball consists of about an equal number of newly created quark-antiquark pairs and initial valence quarks [7]. Hence, there is a considerable net-baryon density, or μ_B.

Once local thermal equilibrium has been established, the further evolution can be described hydrodynamically. Most simply, the fireball can be described as an ideal fluid if the microscopic scattering time scale is much shorter than any macroscopic time scale associated with the fireball evolution [31]. More realistically, the subsequent evolution of the system proceeds as per relativistic imperfect fluid dynamics [32]. This involves expansion, cooling, and dilution. During this expansion, the initial anisotropic collision geometry transforms into a momentum anisotropy leading to a azimuthal modulation of particle production. The energy density and the temperature decrease until hadronization occurs at the critical temperature T_c. At this time, the energy density of the system has dropped to about 1 GeV fm^{-3}. Even below T_c, this hadron gas is still very dense, with a mean free path of the hadrons much smaller than the system size, so it can be described by hydrodynamics as well. Hadrons continue to collide among themselves elastically, which changes their momenta, as well as inelastically, which alters abundances of individual species.

Chemical freeze-out occurs when inelastic processes stop. Possibly, the hadron abundances are fixed already at (or very close to) the phase transition. Kinetic freeze-out happens when elastic scatterings cease, too. These late stages of evolution, when the system is no longer in local equilibrium, are simulated using the relativistic kinetic theory framework. Hadrons decouple from the system approximately 10 fm/c to 20 fm/c after the collision and travel towards the surrounding detectors. After the chemical freeze-out, decays of resonances and unstable particles occur. These decays continue to happen even after the kinetic freeze-out. Particles that reach the detector consist of directly produced hadrons and hadrons from decays.

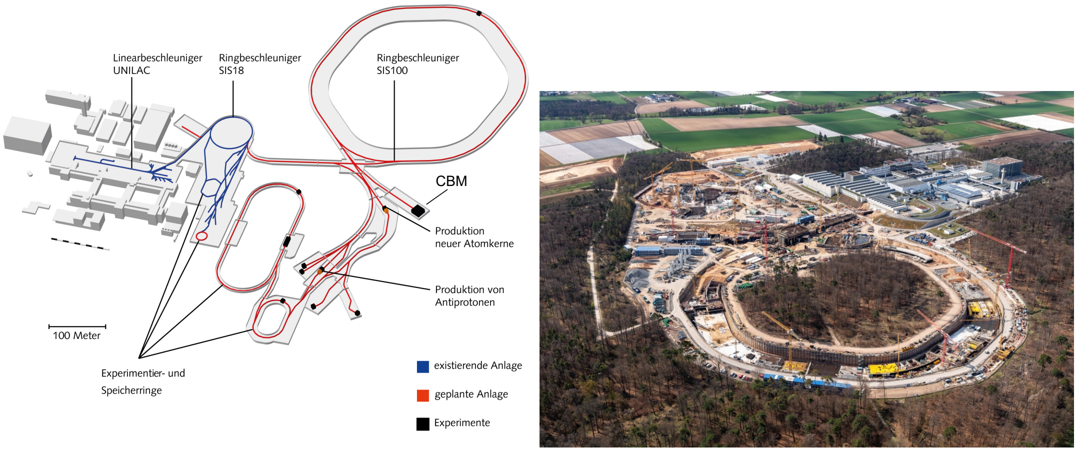

Figure 1.6: Left: Sketch of the future FAIR facilities. Image: GSI/FAIR. Right: Aerial view of the FAIR construction site in April 2020. Image: D. Fehrenz/GSI/FAIR.

1.4 FAIR

The future Facility for Antiproton and Ion Research (FAIR) will be the leading research center in accelerator-based fundamental science and applications for the coming decades. It is currently under construction at the Gesellschaft für Schwerionenforschung GmbH (GSI) in Darmstadt, Germany. A sketch of the planned facility including the existing GSI premises is shown in Figure 1.6. Also shown is an aerial view of the state of construction in April 2021. According to current planning, installation and commissioning of the experiments is planned during the years 2022–2024, while FAIR should be fully operational in 2025 [33].

The FAIR research program covers hadron and nuclear physics, atomic and plasma physics, and applications in the fields of materials research and radiation biophysics including novel medical treatments and space science [34]. FAIR will be able to provide particle beams of all chemical elements and their ions, as well as protons and antiprotons. High-intensity primary beams of protons with kinetic energies of up to 29 GeV, Uranium beams with energies of up to 11 AGeV, and beams of $N = Z$ nuclei with energies of up to 15 AGeV will be delivered by the SIS100 synchrotron. The accelerator tunnel construction allows FAIR to accommodate a second synchrotron, the SIS300. (The numerical values in SIS100 and SIS300 refer to their respective magnetic rigidities of 100 T m and 300 T m.)

Primary heavy-ion beams will be converted into secondary beams of rare isotopes by a large-acceptance Superconducting Fragment Separator. The properties of short-lived neutron-rich or neutron-deficient isotopes will be studied by the subsequent experimental facilities of the NUSTAR (**Nu**clear **St**ructure, **A**strophysics, and **R**eactions) collaboration, in order to explore the nucleosynthesis in the universe. The High-Energy Storage Ring will accelerate and cool intense secondary beams of antiprotons which will be used for hadron physics experiments with PANDA (anti-**P**roton **An**ihilation at **Da**rmstadt).

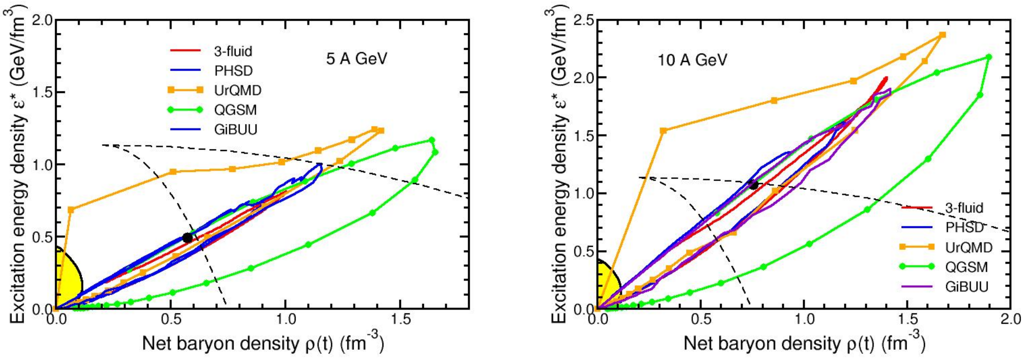

Figure 1.7: Excitation energy density versus net-baryon density in the center of the fireball for simulations of central Au–Au collision at beam energies of 5 AGeV (left) and 10 AGeV (right) [15, 35].

This thesis evolves around the **C**ompressed **B**aryonic **M**atter (CBM) experiment which will investigate the QCD phase diagram at high baryon densities and still moderate temperatures by means of high-energy nucleus-nucleus collisions. Due to the slow beam extraction, the CBM beam will be continuous (non-bunched). This allows for a high collision rate since the beam particles will be distributed uniformly in time. A beam intensity of up to 1×10^9 ions/s results in an interaction rate of up to 10 MHz using a target with a 1 % interaction probability. The rich and exciting physics program of CBM will be introduced in section 1.5, while the CBM experimental setup will be discussed in detail in chapter 3.

1.5 The CBM physics program

The physics program of the CBM experiment aims to explore the QCD phase diagram at high net-baryon densities and still moderate temperatures with high-energy nucleus-nucleus collisions [15]. CBM at SIS100 will run at a center-of-mass energy of $\sqrt{s_{NN}} = 2.7$ GeV to 4.9 GeV ($E_{beam} = 4$ AGeV to 13 AGeV), thus exploring the QCD phase diagram at densities corresponding to $\mu_B \cong 500$ MeV to 800 MeV.

Simulations of central Au–Au collisions with several models at typical CBM beam energies are shown in Figure 1.7. According to the simulation results, the density in the center of the fireball will be greater than $6 \cdot \rho_0$ at 5 AGeV ($\sqrt{s_{NN}} = 3.1$ GeV) and greater than $8 \cdot \rho_0$ at 10 AGeV ($\sqrt{s_{NN}} = 4.3$ GeV) [15, 35].

The discovery of a first-order PT accompanied by the conjectured critical endpoint would represent a breakthrough in the understanding of the physics of the strong interaction in the non-perturbative sector. Increased insight into fascinating phenomena such as the origin of hadron masses, chiral symmetry restoration, or the structure of neutron star cores can be expected from such a discovery. The CBM physics program will address the following fundamental questions [13]:

- The equation of state (EOS) of QCD matter and the relevant degrees of freedom at high net-baryon densities. Is there a phase transition from hadronic to quark–gluon matter, or a region of phase coexistence? Do exotic QCD phases exist? Is there a critical point?
- To what extent are the properties of hadrons modified in dense baryonic matter? Are we able to find indications of chiral symmetry restoration?
- How far can we extend the chart of nuclei towards the strange dimension by producing single– and double-strange hypernuclei? Does strange matter exist in the form of heavy multi-strange objects?

CBM will measure the respective physical observables with high rates and high precision. The most promising probes, expected to shed light on the posed questions, are briefly discussed in the following.

Collective flow Collective flow describes the collective motion of final-state hadrons created in a HIC. The flow has isotropic as well as anisotropic components. The isotropic radial flow aids in the characterization of the system at kinetic freeze-out. Anisotropic flow results from anisotropies in the initial parton density distributions that transform into pressure gradients.

The evolution of flow in response to the pressure gradients is controlled by the stiffness $\partial p/\partial e$ (p is the pressure and e is the comoving energy density) of the EOS [36]. Due to the limited number of particles emitted from a single event, statistically precise measurements of the anisotropic flow coefficients v_n and their associated flow angles Ψ_n can only be obtained from particle distributions that have been averaged over many events. One defines the mean flow coefficient $\bar{v}_n$ and the mean flow angle $\bar{\Psi}_n$ through a Fourier decomposition of the experimentally determined, event-averaged particle distribution

$$\frac{d\bar{N}}{d\varphi} = \frac{\bar{N}}{2}\left(1 + 2\sum_{n=1}^{\infty} \bar{v}_n \cos(n(\varphi - \bar{\Psi}_n))\right) . \tag{1.2}$$

Here, $\bar{N}$ is the mean number of particles of interest per event and φ is the azimuthal angle of the transverse momentum vector p_T of the emitted particle in the laboratory frame.

The directed flow v_1 is sensitive to details in the description of the initial state and the softening of the EOS [37]. The elliptic flow v_2 is a fundamental observable since it directly reflects the rescattering among the produced particles. It is a hadronic signature that is sensitive to the hot and dense QGP stage before hadronization sets in [38], providing access to the fundamental thermalization time scale in the early stages of a relativistic HIC. The CBM experiment will dramatically improve the data situation by measuring the flow of identified particles in the FAIR energy range, including multi-strange hyperons and dileptons.

Dilepton spectroscopy Virtual photons are radiated off during the whole time evolution of the HIC. Once produced, they decouple from the collision zone and materialize as muon or electron pairs. Since they do not further interact with the surrounding medium, they present a unique opportunity to investigate the hot and dense medium at the time of their production. The excess yield of lepton pairs in the low-mass range ($M \leq 1\,\mathrm{GeV/c^2}$) is sensitive to both the temperature of the created matter and its space-time extension [39]. A consequence of chiral symmetry restoration is that chiral partners such as the $\rho-$ and a_1-meson are degenerate in mass. While the a_1 is difficult to measure, the in-medium ρ spectral function can be probed in the low-mass regime, because this meson saturates the hadronic current in a hadron resonance gas [40].

Figure 1.8 shows the invariant-mass spectrum of $\mathrm{e^+e^-}$–pairs radiated off from a central Au–Au collision at 20 AGeV [13]. The slope of the dilepton invariant-mass distribution in the region $1\,\mathrm{GeV/c^2} < M < 2.5\,\mathrm{GeV/c^2}$ directly reflects the average temperature of the fireball [41]. The true temperature T_s (no blue shift) of the emitting source can be extracted from a fit of the acceptance-corrected thermal spectra with $M^{3/2}\exp(-M/T_s)$. This opens the unique possibility to measure the caloric curve, which would be the first direct experimental signature for phase coexistence in high-density nuclear matter. Figure 1.9 shows this caloric curve, i.e. the fireball temperature extracted from intermediate dilepton mass distributions ($M = 1.5 - 2.5\,\mathrm{GeV/c^2}$). It shows a mild plateau above $T = 150\,\mathrm{MeV}$, which could be an indication for the onset of deconfinement. The black data points show the results of two temperature measurements performed with the above-described procedure, conducted by the HADES and NA60 collaborations.

So far, no dilepton data have been measured in HICs at beam energies between 2 AGeV to 40 AGeV. The CBM experiment will perform pioneering multi-differential measurements of lepton pairs over the whole range of invariant masses emitted from a hot and dense fireball. The experimental challenges include very low signal cross sections in a high combinatorial background and decay probabilities of $O(1 \times 10^{-4})$.

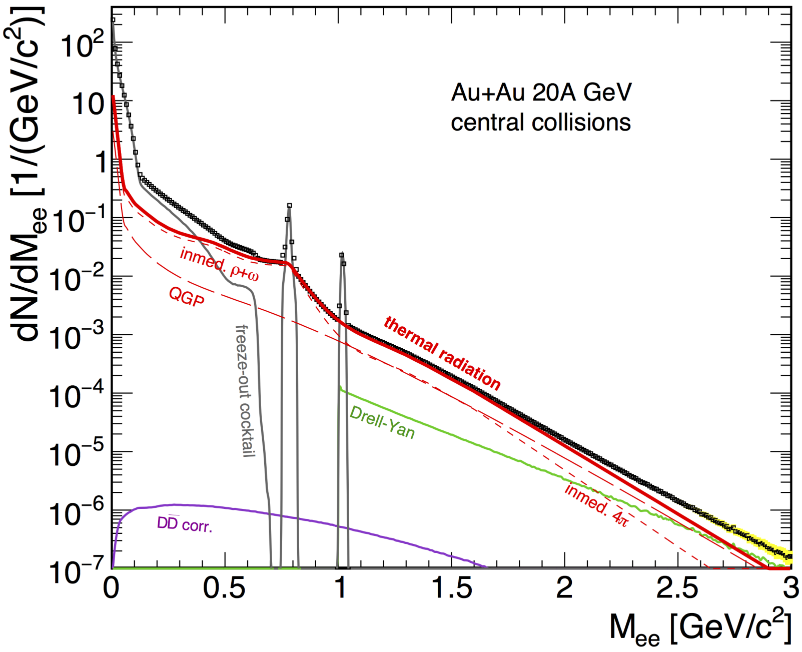

Figure 1.8: Invariant-mass spectrum of e$^+$e$^-$ pairs radiated from a central Au–Au collision at 20 AGeV [13].

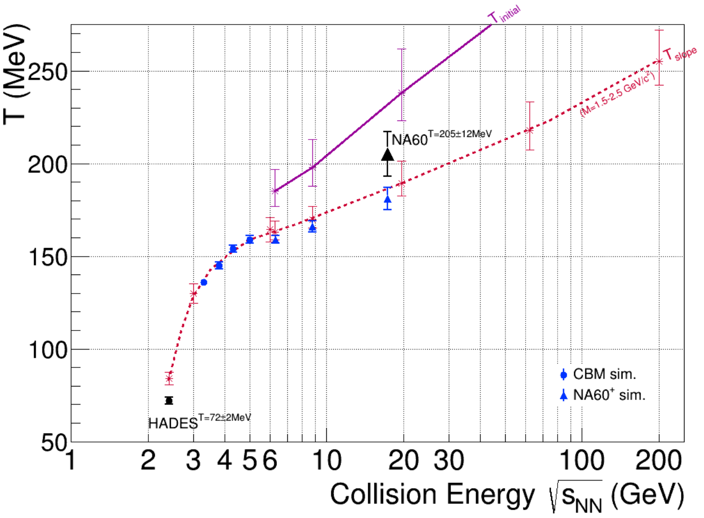

Figure 1.9: Excitation function of fireball temperature extracted from intermediate dilepton mass distributions ($M = 1.5 - 2.5\,\mathrm{GeV/c^2}$) (red dotted curve) and initial temperature (solid violet curve) [41, 42]. The black triangles correspond to temperature measurements by the NA60 collaboration at CERN-SPS and the HADES collaboration at GSI. The blue squares and triangles show simulated values for CBM and NA60$^+$ collision energies, respectively. Figure taken from [43].

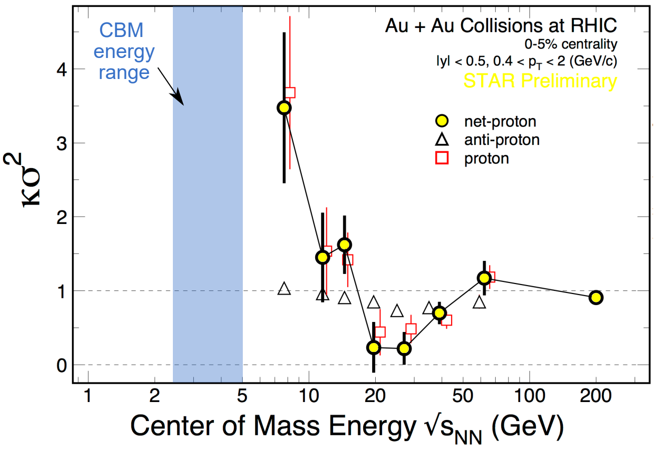

Figure 1.10: Energy dependence of excess kurtosis times variance of the net-proton multiplicity distribution (yellow circles) for top 0-5% central Au–Au collisions [44, 45]. The dotted line is the Poisson expectation at $\kappa\sigma^2 = 1$. Deviations from 1 indicate critical behavior. Adapted from [13].

Event-by-event fluctuations Event-by-event fluctuations of conserved quantities such as baryon number, strangeness, and electrical charge can be related to the thermodynamical susceptibilities and hence provide insight into the properties of matter created in high-energy nuclear collisions [13]. Non-Gaussian moments (cumulants) of these fluctuations are expected to be sensitive to the proximity of the critical point since they are proportional to powers of the correlation length.

Figure 1.10 shows a set of measurements of the volume-independent product of kurtosis (second order cumulant) times variance carried out by the STAR collaboration, showing a deviation from unity, as expected for a critical behaviour. To date no higher-order event-by-event fluctuations have been measured at SIS100 energies, calling for CBM to complement the existing measurements in search of the elusive critical point.

Strangeness and hypernuclei Strange particles are important probes of the excited medium created in the HIC. High-precision measurements of excitation functions of multi-strange hyperons in symmetric nucleus-nucleus collisions at SIS100 energies will allow to study the degree of equilibration of the fireball. According to hadronic transport models, multi-strange (anti-)hyperons are produced in sequential collisions involving kaons and lambdas and, therefore, are sensitive to the density in the fireball. A hypernucleus is formed when an up or down quark inside a nucleon is replaced by a strange quark. Thermal model calculations predict that the excitation function of hypernucleus production exhibits its maximum in the SIS100 energy range, see Figure 1.11. The CBM experiment has a substantial discovery potential for light double-Λ hypernuclei. Information about hyperon-hyperon and hyperon-nucleon interaction can be deduced from measuring (double-)Λ hypernuclei and their lifetimes which will further our understanding of the nuclear matter EOS at high densities.

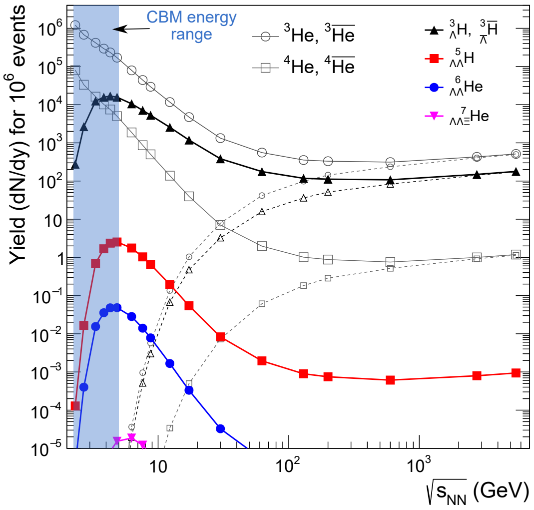

Figure 1.11: Energy dependence of predicted hypernuclei yields at midrapidity for 1×10^6 central collisions. For comparison, the predicted yields of ^{3}He and ^{4}He nuclei are included, together with the corresponding anti-nuclei (dashed lines) Adapted from [46].

2 Silicon Detector Fundamentals

In this chapter, some fundamentals of semiconductor physics will be discussed. The focus lies on silicon and its use as a radiation detector in particle or heavy ion physics. To begin, the energy band model and some essential properties of silicon are discussed briefly, followed by the process of doping and a discussion of the p–n junction. In order to be used as a radiation detector, the p–n junction inside the detector has to be depleted. Radiation damage mechanisms, which are extremely important for the sensors as well as the readout electronics, are discussed before a brief introduction into signal formation in the active sensor volume, the time evolution of the signal, and basic signal acquisition. In order to achieve high spatial resolution and low occupancy in large-area tracking detectors, such as the STS, the active sensor volume has to be segmented into strips or pixels. A brief introduction into silicon microstrip sensors concludes the chapter.

2.1 The energy band model and important properties of silicon

The energy band model describes the allowed energy and reduced momentum levels of an electron inside the semiconductor. However, it cannot give any information about the time evolution or motion of electrons inside the crystal. This can be easily understood by Heisenbergs uncertainty principle $\Delta E \Delta t \geq \hbar$ and $\Delta p_x \Delta x \geq \hbar$. Wavepackets are needed to describe the motion of electrons inside the crystal. A wavepacket is a linear combination of fixed-energy wavefunction solutions which are closely grouped around a center energy. In correspondence with the center of mass of a classical particle moving with velocity v, the wavepackets center moves with a group velocity $v_g = dx/dt$. An external force F acting on the wavepacket yields, after some simple calculations [47]

$$F = m^* \frac{dv_g}{dt} \qquad\qquad m^* \equiv \frac{1}{\frac{1}{\hbar^2}\frac{d^2E}{dk^2}} \,. \tag{2.1}$$

Equation (2.1) simply is Newton's second law of motion with an *effective mass* m^* replacing the classical particle mass. Hence, the motion of an electron inside a crystal can be described quasi-classically. Equation (2.1) illustrates the importance of E–k diagrams (energy over wavevector), as the effective mass is inversely proportional to the curvature of the E–k plot. Typically, the E–k relationship is parabolic near the band edges—the regions in phase space that are populated by charge carriers. Therefore, charge carriers inside the crystal usually have a constant effective mass.

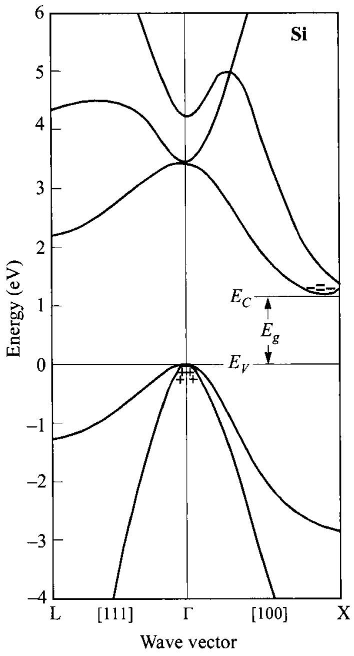

Figure 2.1: Energy band or E–k diagram of Si. Figure taken from [48].

As CBM employs silicon (Si) detectors, from now on the focus will be put on Si rather than semiconductors in general. Still, many of the discussed principles apply to all types of semiconductors. Figure 2.1 shows the band structure of Si. Si is an indirect semiconductor, i.e. the conduction band minimum and valence band maximum have a different wave vector k. Therefore, the excitation of an electron from the valence band into the conduction band requires the simultaneous transfer of energy and momentum. The required momentum is converted into lattice vibrations which are quantized as phonons. The absorption process of incoming signal quanta must conserve energy as well as momentum. For charged particles, a significant amount of the absorbed energy must go into momentum-carrying excitations. Hence, the ionization or excitation energy in Si, $E_I = 3.62\,\text{eV}$, is more than three times higher than the bandgap $E_g = 1.12\,\text{eV}$.

Electrons obey Fermi-Dirac statistics. The probability of an electron to occupy a state with energy E is

$$f_e(E) = \frac{1}{e^{(E-E_F)/kT} + 1} \,. \tag{2.2}$$

The probability of an empty valence state is

$$f_h(E) = 1 - f_e(E) = \frac{1}{e^{(E_F-E)/kT} + 1} \,. \tag{2.3}$$

Here, E_F denotes the Fermi energy, k the Boltzmann constant, and T the temperature. In a pure semiconductor, electron and hole concentrations must be the same, $n = p = n_i$. The

Fermi level lies very close to the middle of the bandgap. It is not located exactly in the center due the slightly unequal effective masses of electrons and holes, m_n and m_p:

$$E_F = \frac{E_C + E_V}{2} + \frac{3kT}{4} \ln(m_p/m_n)\,. \tag{2.4}$$

Here, E_C and E_V denote the conduction band minimum and valence band maximum, respectively. The intrinsic carrier concentration is [49]

$$n_i = \sqrt{N_C N_V} e^{-E_g/2kT}\,, \tag{2.5}$$

with the effective densities of states at 300 K, $N_C = 3.23 \times 10^{19}\ \mathrm{cm}^{-3}$ and $N_V = 1.83 \times 10^{19}\ \mathrm{cm}^{-3}$ [47]. The room temperature atomic density of Si is 4.99×10^{22} atoms/cm^3. The thermal energy kT at 300 K is 25.85 meV, around 50 times smaller than the bandgap of Si. For $kT = 25$ meV, the probability of an electron to occupy a state in the conduction band is only 1.87×10^{-10}. However, due to the high density of states one arrives (see eq. (2.5)) at an intrinsic carrier concentration of $n_i = 9.51 \times 10^{9}\ \mathrm{cm}^{-3}$.

2.2 Doping and the p–n junction

A semiconductor with an insignificant concentration of impurity atoms is called an *intrinsic* semiconductor. Electron and hole carrier concentrations are always equal. In pure Si, the resistivity at room temperature is around 400 kΩ cm. Due to crystal imperfections and impurities, realistically achievable resistivities are one to two orders of magnitude lower. These resistivities are too low to realize an electric field large enough for efficient charge collection. This becomes clear with the following example: Considering a 320 µm thick sensor with an area of 36 cm^2 (approximate STS sensor dimensions) with a resistivity of 5 kΩ cm, the sensor would have a resistance of 4 Ω. Applying a voltage of 40 V across the sensor would lead to a current flow of 10 A and a power dissipation of 40 W, rendering it useless as a radiation detector with typical signal currents of O(µA). Moreover, the electron and hole populations and associated properties such as the resistivity of intrinsic semiconductors are highly temperature-dependent.

These difficulties can be mitigated by a process called *doping*, the purposeful implementation of impurity atoms into the Si crystal. Typical doping concentrations are 10^{12}–$10^{18}\ \mathrm{cm}^{-3}$. Si is a column-IV element, i.e. it has four valence electrons. If a column-V atom such as phosphorus (P) is introduced into the crystal lattice, one of its five valence electrons is unable to form a bond. The P atom donates an extra electron to the lattice; thus being called a donor. The donor electron is only loosely bound. In the case of P, its energy level is 45 meV below E_C, as sketched in Figure 2.2. Hence, the thermal energy at room temperature ($kT \sim 25$ meV) is sufficient to excite a significant amount of electrons from the donor level into the conduction band. The charge carrier is negative, therefore the material is called *n-type*.

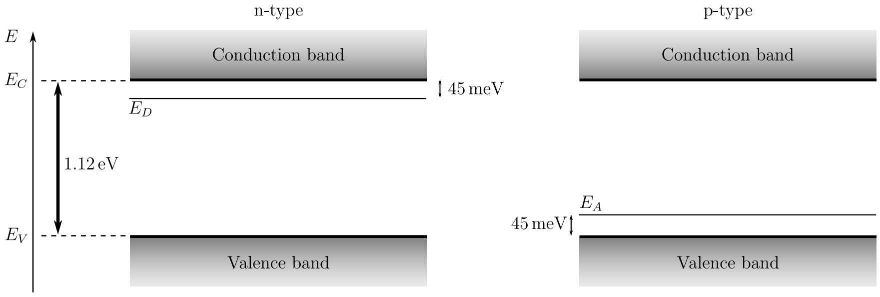

Figure 2.2: Energy band scheme for n-type (left) and p-type (right) Si. The doping process introduces shallow energy levels close to the conduction band minimum and valence band maximum, respectively.

If a column-III atom such as boron (B) is introduced, it readily accepts an electron from a nearby Si–Si bond, therefore being called an acceptor. The borrowed electron is loosely bound again, as the B nucleus only has a charge of 3. In case of B, the introduced energy level sits 45 meV above E_V (Figure 2.2). The thermal energy at room temperature is sufficient to excite a significant amount of electrons from the valence band into the acceptor level, leaving behind mobile positive charge states, called holes. As the charge carrier is positive, the material is called *p-type*.

As described above, the majority of introduced donor and acceptor levels are excited at room temperature, making their contribution to the charge transport nearly independent of temperature around room temperature. The contribution to the charge transport by band-to-band generation is negligible. Hence, in a properly-doped semiconductor conductivity is basically independent of temperature around room temperature and its value is controlled by the fabrication process [50].

The introduction of other types of impurity atoms into the semiconductor can give rise to deep-level states inside the bandgap more than a few tenths of an eV from the band edges. These levels are also called traps or recombination-generation centers and are undesirable in a radiation detector.

In order to be usable as a radiation detector, one must bring an n-type and p-type semiconductor into contact, forming a p–n junction. Additionally, the p–n junction needs to be reverse-biased, which will be discussed in section 2.3. If a p-type and n-type region are brought into contact, thermal diffusion drives electrons into the p-region and holes into the n-region. This leaves behind negatively and positively charged atomic cores that build up a restraining potential, which in turn limits the diffusion. In thermal equilibrium, a built-in potential V_{bi} establishes across the junction. The diffusion of charge carriers leaves a region devoid of mobile charge carriers across the junction—the *depletion region.*

In n-type material, the increased electron concentration shifts the Fermi level from midgap closer to the conduction band, whereas in p-type material the Fermi level is shifted closer to the valence band. In thermal equilibrium, the Fermi level must be constant throughout the device. Hence, the energy bands must bend across the p–n junction, as illustrated in Figure 2.3

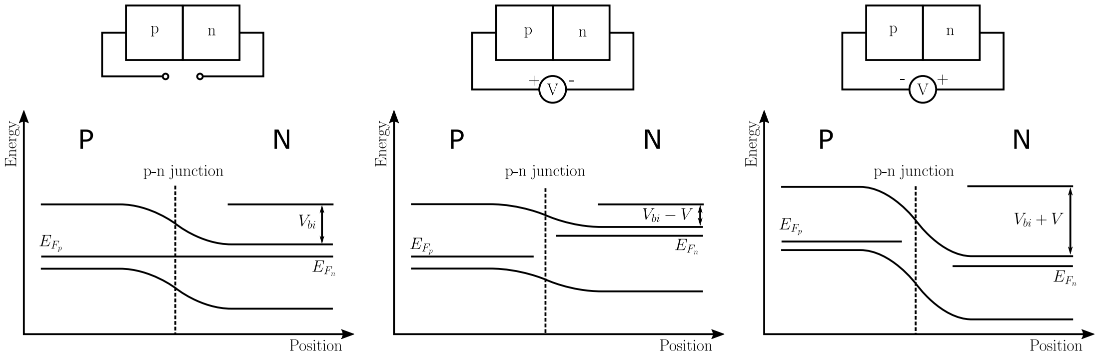

Figure 2.3: Energy band diagram of a p–n junction for different biasing schemes. Left: Unbiased. Middle: Forward bias. Right: Reverse bias as used in a radiation detector.

on the left. The potential difference between the n– and p-region is equal to the difference in Fermi levels of the regions in isolation, $V_{bi} = E_{F_n} - E_{F_p}$. The built-in voltage depends on the doping levels N_a and N_d [48]

$$V_{bi} = \frac{kT}{e} \log\left(\frac{N_a N_d}{n_i^2}\right). \tag{2.6}$$

Assuming doping levels of N_a and $N_d = 10^{12}\,\mathrm{cm^{-3}},\ 10^{15}\,\mathrm{cm^{-3}}, and 10^{18}\,\mathrm{cm^{-3}}$ and $n_i = 9.51 \times 10^{9}\,\mathrm{cm^{-3}}$, the built-in potentials at 300 K are 0.24 V, 0.60 V, and 0.95 V, respectively.

There are two options for biasing the p–n junction. In *forward bias*, positive potential is applied to the p-region and negative potential to the n-region. The potential barrier is reduced and the current flow across the junction increases. As this biasing scheme has no applications in a tracking detector, it will not be discussed any further. In *reverse bias*—as used in particle detectors—the positive potential is applied to the n-region and the negative potential to the p-region. This increases the width of the depletion zone which reduces the majority charge carrier current. Thereby, it allows us to detect small signals generated by the passage of charged particles through the sensitive sensor volume. The effect of both biasing schemes on the energy bands is shown in Figure 2.3.

2.3 Depletion inside a radiation detector

The starting point for the determination of the depletion width in a reverse-biased diode is Poisson's equation

$$\frac{d^2V}{dx^2} + \frac{Ne}{\epsilon_0 \epsilon_{Si}} = 0\,, \tag{2.7}$$

where N is the dopant concentration, e the elementary charge, $\epsilon_0 = 8.854 \times 10^{-12}\,\mathrm{F\,m^{-1}}$ the vacuum permittivity, and $\epsilon_{Si} = 11.7$ the dielectric constant of Si. Integrating eq. (2.7) twice, respecting the boundary conditions at the p–n interface as well as net charge neutrality, one arrives at the following expressions for the depletion widths on the n– and p-side

$$x_n = \sqrt{\frac{2\epsilon_0\epsilon_{Si}V_b}{eN_d(1+N_d/N_a)}} \qquad x_p = \sqrt{\frac{2\epsilon_0\epsilon_{Si}V_b}{eN_a(1+N_a/N_d)}}\,. \tag{2.8}$$

Here, V_b is the applied bias voltage, and N_d and N_a the donor and acceptor concentrations. The junction potential at the p–n interface is

$$V_j = \left(\frac{N_d}{N_a}\right)\frac{V_b}{(1+N_d/N_a)}\,. \tag{2.9}$$

In the case of unequal doping concentrations, e.g. $N_d << N_a$, eq. (2.9) simplifies to

$$V_j \approx \frac{N_d}{N_a}V_b\,. \tag{2.10}$$

The junction potential is negligible compared to the bias voltage, so it is basically equal to the potential of the p-contact. Therefore, all of the bias voltage develops across the n-region. In radiation detectors, this property is exploited to make the depletion region develop across the lightly doped bulk in comparison to the more heavily doped implants.

According to eq. (2.8), the depletion width increases with increasing bias voltage. This increases the sensitive volume and reduces the sensor capacitance. Hence, in a radiation detector, a high bias voltage is desired in order to minimize the capacitance and thus the noise of the readout circuit connected to it. An upper limit for the bias voltage is set by power consumption, coupling capacitor breakdown, and most importantly *avalanche breakdown* of the bulk. If the electric field is high enough, electrons are accelerated to such high energies that they can create secondary e–h pairs via impact ionization. Another type of breakdown, called Zener breakdown, happens through quantum tunneling effects at lower voltages. Assuming $N_d << N_a$, eq. (2.8) reduces to

$$\omega \approx x_n = \sqrt{\frac{2\epsilon_0\epsilon_{Si}V_b}{eN_d}}\,. \tag{2.11}$$

Doping concentrations can be expressed as the feasibly measurable resistivities

$$\rho_n = \frac{1}{e\mu_n N_d} \qquad \rho_p = \frac{1}{e\mu_p N_a}\,. \tag{2.12}$$

Typical RT-mobilities in Si with doping levels of $N_d = 1\times10^{14}\,\mathrm{cm^{-3}}$ and $N_a = 1\times10^{14}\,\mathrm{cm^{-3}}$ are $\mu_n = 1360\,\mathrm{cm^2\,V^{-1}\,s^{-1}}$ and $\mu_p = 460\,\mathrm{cm^2\,V^{-1}\,s^{-1}}$ [47]. Inserting eq. (2.12) into eq. (2.11) gives

$$\omega = \sqrt{2\epsilon_0\epsilon_{Si}\mu_n\rho_n V_b}\,. \tag{2.13}$$

The fully depleted bulk is free of mobile charge and forms a capacitor

$$C = \frac{\epsilon_0\epsilon_{Si}A}{\omega} = A\sqrt{\frac{\epsilon_0\epsilon_{Si}eN}{2(V_b+V_{bi})}}\,. \tag{2.14}$$

Leakage current A low total leakage current is one of the major criteria for the quality and functionality of a microstrip detector. Leakage current is caused by thermally excited e–h pairs in the Si bulk in the presence of an electric field, representing a source of noise in the final readout system. It is proportional to the depletion layer thickness which in turn is proportional to $\sqrt{V_b}$. The leakage current should be constant after reaching full depletion. Deviations from this rule are direct indications of sensor flaws such as variations in processing [51]. Bulk sensor currents are direct indications for bulk impurity concentrations, defining the charge carrier lifetime and thus the current. High current, especially a localized one, is also a defect signature. When measuring the global leakage current, bulk current must be distinguished from surface currents deriving from interface traps (which cannot be avoided) and/or "bad" oxides, scratches, and/or process errors. Bulk leakage currents are, in contrast to surface currents, strongly temperature-dependent [51]. During radiation, mid-gap defects are constantly produced. They are efficient electron-hole pair generators and therefore increase the leakage currents [51]. The effects of radiation on silicon sensors and readout electronics is discussed in more detail in the following section.

2.4 Radiation damage and radiation resistance

Radiation-tolerant detectors and readout electronics are becoming increasingly critical in high energy physics (HEP), as beam intensities are ever-growing. In this section, common radiation damage mechanisms in Si are discussed briefly before introducing possible mitigation techniques. There are two basic radiation damage mechanisms in semiconductor devices, namely *displacement damage* and *ionization damage*.

Displacement damage. Displacement damage occurs when a crystal atom is displaced from its lattice site, changing the electrical characteristics of the material. Displacement damage depends on the non-ionizing energy loss (NIEL) [52], i.e. momentum and energy transfer to atoms of the crystal, which in turn depends on the mass and energy of the incoming particles. Therefore, it must be specified for the specific particle type and energy. Figure 2.4 shows the displacement damage cross section as a function of energy for neutrons, protons, pions, and electrons normalized to 1 MeV neutrons. For displacement damage, the details of defect formation are important. For example, a 1 MeV neutron transfers around 60 keV to 70 keV to the primary Si atom, which in turn can displace 1000 further atoms from their lattice sites. It creates a highly clustered vacancy distribution. In contrast, a 10 MeV proton creates a much more uniform defect distribution. Si detectors for applications in HEP are tested with particles at energies much different from the actual conditions in the experiments in which they will run. The correlation of the results is typically done with the NIEL scaling hypothesis which describes the proportionality between NIEL and the resulting damage effects. However, the application of the NIEL scaling hypothesis has its limits [58] and its validity is questioned by a microscopic analysis [59]. There are three main consequences of displacement damage:

- Formation of states close to the band edges which facilitate trapping.

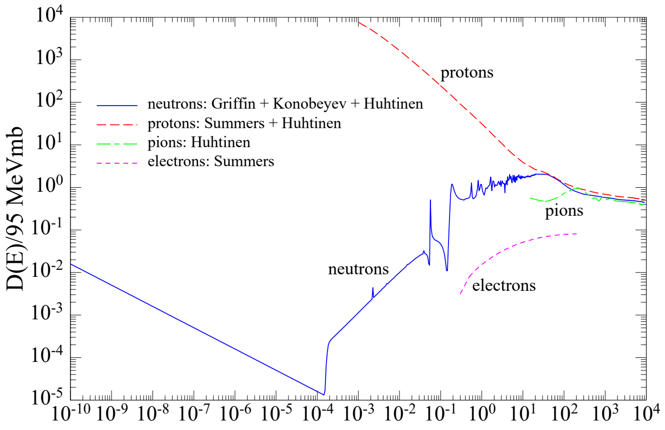

A. Vasilescu & G. Lindstroem

Figure 2.4: Displacement damage in Si for electrons, protons, neutrons, and pions normalized to 1 MeV neutrons. Data are taken from [53, 54, 55, 56, 57].

- Formation of states in the middle of the band gap which facilitate transitions between the valence and the conduction band, thus leading to an increase in leakage current.
- Change in effective donor and acceptor densities.

Si is an indirect semiconductor, which makes direct transitions between the bands highly unlikely. The transition probabilities are Boltzmann-distributed, i.e. they are exponentially dependent on the energy difference between the initial and final state ($\propto \exp\left(-\Delta E/kT\right)$). The mid-gap states caused by displacement damage provide additional pathways to cross the bands, leading to an increase in recombination and generation processes. In a reverse-biased diode, generation dominates, because the conduction band is underpopulated in a depleted region. The increase in leakage current leads to increased electronic shot noise and a risk of thermal run-away.

Defect energy levels close to the band edge cause trapping, where charge is captured and released after a certain time. Trapping results in signal loss while the charge crosses the depletion region. While defects can act as donors, acceptors, or be neutral, the predominant charge states formed in Si are acceptor-like. A sufficient concentration of defects can lead to a change in space charge in the active region which then requires adjustments in the bias voltage to achieve full charge collection.

Ionization damage. Ionization damage describes effects caused by ionization in insulating layers, usually SiO_2, Si_3N_4, or a combination of both. Ionization effects are independent of the type of radiation and depend primarily on the absorbed energy. At typical energies in HEP experiments, ionization is the dominant absorption mechanism. Hence, it is proportional to the dose (energy absorption per unit volume), expressed in rad or gray. It is important to note that the liberated charge per dose is dependent on the absorber material.

Ionizing radiation creates e–h pairs in the oxide ($E_i = 18\,\mathrm{eV}$). While the electrons move quickly to the positive electrode, the holes move by a complex and slow hopping mechanism with a relatively higher probability of being trapped. If the holes reach the oxide-silicon interface they can be captured by interface traps which are caused by the lattice mismatch and impurities. Trapped oxide charges are non-static. Their distribution especially depends on the evolution of the electric field in the oxide, thus it varies with changes in applied voltage. Additionally, the charge states anneal. The resulting damage effects of ionizing radiation are a complex function of dose rate, applied voltages, temperature, and variations in the radiation itself [60].

Generally, radiation effects should be tested for displacement *and* ionization damage. Tracking detectors, such as the STS, are reverse-biased diodes with large depletion depths of several hundreds of microns. Therefore, they are highly susceptible to bulk damage which affects the detector leakage current, doping profiles, and charge collection efficiency.

2.5 Signal formation

Signal formation in a semiconductor or gaseous tracking detector is based on the ionization of the medium by the passage of charged particles. The ionization process is visualized in Figure 2.5. The average energy loss of a heavy charged particle in matter is described by the Bethe formula

$$-\frac{dE}{dx} = 4\pi N_\mathrm{A} r_e^2 m_e c^2 z^2 \frac{Z}{A}\frac{1}{\beta^2}\left[\frac{1}{2}\ln\frac{2m_e c^2\beta^2\gamma^2 T_{max}}{I^2} - \beta^2 - \frac{\delta(\gamma)}{2}\right] \quad \left[\mathrm{MeV\,g^{-1}\,cm^2}\right]. \tag{2.15}$$

Here, z is the charge of the incident particle, T_{max} the maximum kinetic energy which can be imparted to a free electron in a single collision, I the mean excitation energy (173 eV in Si), Z the atomic number, A the atomic mass, N_A Avogadro's number, m_e and r_e the electron mass and classical electron radius, c the speed of light, $\beta = v/c$, $\gamma = \frac{1}{\sqrt{1-\beta^2}}$, and δ the density-effect correction.

The Bethe function expresses a minimum around $\beta\gamma = 3$. The detector noise level must be significantly below this minimum deposited energy to detect the corresponding minimum-ionizing particles (MIPs). The absorbed energy divided by the excitation energy gives the average number of created signal quanta $N = E/E_i$. This number is subject to quantum-statistical fluctuations, as the number of collisions in a finite medium as well as the energy transfer per scattering is subject to variation. Hence, the relative energy resolution of the detector is

$$\frac{\Delta E}{E} = \frac{\Delta N}{N} = \frac{\sqrt{FN}}{N} = \sqrt{\frac{FE_i}{E}}\,. \tag{2.16}$$

Here, F is the Fano factor, which is 0.1 for Si [60]. As a result of the statistical fluctuations, the most probable value (MPV) of energy transfer is around 30% below the average energy

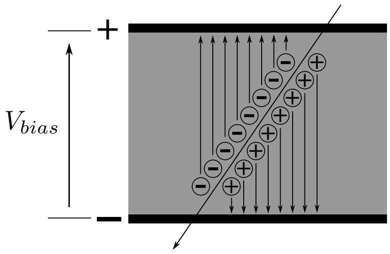

Figure 2.5: Ionization process creating e–h pairs inside a semiconductor. The arrow symbolizes an incoming charged particle. Applying a bias voltage between the two opposite electrodes creates an electric field that helps separating the charges.

transfer. In 1 µm of Si, a MIP creates an average of 108 e–h pairs, while the MPV is 76 e–h pairs.

Considering a 62 mm × 62 mm STS sensor with a thickness of 320 µm, there are 1.78×10^{10} free charge carriers inside the volume. A MIP produces an average of $108\frac{\text{e–h}}{\mu\text{m}} \cdot 320\,\mu\text{m} = 34\,560$ e–h pairs, thus making the need for full depletion of the sensors apparent. The MPV in this example is 24 192 e–h pairs, corresponding to a collected charge of 3.9 fC at either side of the detector. If an electric field is applied across the detector, the collective motion of the created charge carriers induces a change in induced charge on the electrodes which can be measured as a signal current. A high electric field results in a fast response time and high charge collection efficiency.

2.6 Time evolution of the signal current

Moving charges inside the active sensor area give rise to a signal current. This current flow begins instantaneously, not merely when the charge reaches the electrodes. A charge moving from the upper electrode to the lower electrode initially induces most charge on the upper electrode and subsequently more and more charge on the lower electrode as it moves towards it. If the electrodes are connected, the induced charge can be measured as a signal current. Integrating the induced current over the charge collection time yields the difference in induced charge q. A quantitative description is found by Ramo's theorem which applies to all structures with moving charges inside a set of electrodes [61].

Here, only the results will be summarized, a more detailed description can be found in [60]. A charge q, moving from point 1 to point 2, induces on electrode A a net charge

$$\Delta Q_A = q(V(2) - V(1)) \equiv q(\Phi_A(2) - \Phi_A(1)), \tag{2.17}$$

with the potentials at points 1 and 2, $V(1)$ and $V(2)$, and the so-called weighting potential Φ. Φ is electrode-specific and is obtained by setting the electrode to unit potential and all other electrodes to zero potential. The instantaneous current is related to the weighting field $\vec{E}_Q$

$$i_A = -q \cdot \vec{v} \cdot \vec{E}_Q \, . \tag{2.18}$$

2.6.1 Parallel plates with uniform field

A detector operating in large overbias has an approximately uniform electric field. Assuming an e–h pair is created at a distance x from the positive electrode, the charge collection times t_{ce} and t_{ch} are

$$t_{ce} = \frac{x}{v_e} = \frac{xd}{\mu_e V_b} \, , \qquad t_{ch} = \frac{d-x}{v_h} = \frac{(d-x)d}{\mu_h V_b} \, , \tag{2.19}$$

with electron and hole mobilities μ_e and μ_h, the bias voltage V_b, and the distance between the electrodes d. Since they move in opposite directions, electrons and holes induce same-sign charge on a given electrode. The induced charges are

$$Q_e = e\mu_e \frac{V_b}{d^2} \frac{xd}{\mu_e V_b} = e\frac{x}{d} \, , \qquad Q_h = e\mu_h \frac{V_b}{d^2} \frac{(d-x)d}{\mu_h V_b} = e(1 - \frac{x}{d}) \, . \tag{2.20}$$

It should be noted that only integration times larger than the charge collection time of all carriers result in full charge collection. Kirchoff's current law $\Sigma_n i_n = 0$ must be satisfied. For two electrodes, $i_1 = -i_2$. In the case of a strip detector, which will be discussed next, the current on one electrode must balance the sum of all other electrodes. Thus, all signal currents can be different.

2.6.2 Double-sided strip detector

For a double-sided strip detector with a pitch small compared to the sensor thickness, the electric field is similar to the parallel-plate geometry discussed before, if not in the immediate vicinity of the strips. However, the weighting potential is markedly different. It is strongly peaked near the signal electrode. Generally, only charges terminating on the electrode of interest contribute to its signal current. Charges terminating on neighboring strips do induce a signal current on the center electrode, yet the current changes sign while the charge traverses the sensor volume and the current integrates to zero.

Compared to an extensive planar electrode with the same dimensions, current pulse shapes can be significantly different in a double-sided strip detector. The signals on the opposite sides of a double-sided detector have different pulse shape and the net induced charge on any given electrode is not split evenly between electrons and holes. However, even if the signal shapes on opposite sides differ, the same signal charge is obtained when integrating over the full collection time.

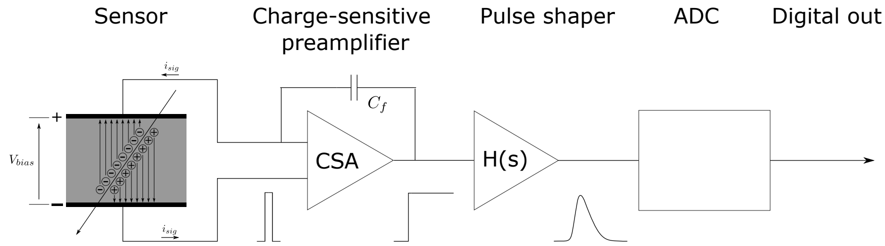

Figure 2.6: Basic signal and readout chain in a charge particle detector system. Incident radiation on the sensor gives rise to a current pulse. The small current signal is amplified, shaped, and finally digitized for storage and analysis.

2.7 Signal acquisition

Figure 2.6 depicts the elementary building blocks of signal acquisition in a radiation detector. The typical signal charge in a high-energy tracking detector such as the STS is quite small—around 4 fC—making signal amplification essential. The magnitude of the signal underlies statistical fluctuations, described by the Landau-Vavilov distribution. Electronic noise further smears the signal. Since the collection time is in the order of nanoseconds, the signal can be described as a Dirac current pulse whose integral equals the total generated charge Q. The generated charge Q is integrated onto the feedback capacitance C_f of a low-noise charge-sensitive amplifier (CSA) resulting in a voltage step with the amplitude Q/C_f at the CSA output. CSAs are in widespread use in particle physics, due to their low noise behavior and insensitivity of the gain to variations of the detector capacitance C_d. A critical noise parameter is the total capacitance seen by the input of CSA, i.e. the sum of detector capacitance, stray capacitances of interconnects, and the input capacitance of the CSA. The individual noise contributions in a detector readout system as used in the STS will be discussed in more detail in chapter 6.

After the CSA has amplified and integrated the signal current, the signal is fed to a pulse shaper. Because the frequency spectra of the signal and the noise differ, a clever shaper design will improve the signal-to-noise ratio (SNR) of the system by favoring signal frequencies over noise frequencies. The noise depends linearly on the bandwidth, thus a shaper stretches the signal pulse in the time domain. An upper bound to the pulse width is set by pile-up. Pile-up occurs when two successive pulses overlap in time which results in a wrong peak-amplitude measurement. Optimum SNR is achieved by a Gaussian-shaped step response. While an ideal Semi-Gaussian filter cannot be implemented in a physical system, a delayed Gaussian waveform is approximated by a CR-(RC)$^{\text{n}}$ filter; a CR high-pass filter followed by n RC low-pass filters. The CR differentiator sets the decay time while the RC integrator increases the rise time to decrease noise bandwidth. The transfer function of such a filter is [62]

$$H(s) = \left(\frac{s\tau_d}{1 + s\tau_d}\right)\left(\frac{A}{1 + s\tau_i}\right)^n , \tag{2.21}$$

where τ_d and τ_i are the time constants of the differentiator and integrator, A is the DC gain of the integrator, and $s = j\omega$. Including the CSA, the total transfer function of the system becomes

$$H(s)_{total} = \left(\frac{A_{csa}}{1 + s\tau_{csa}}\right)\left(\frac{s\tau_d}{1 + s\tau_d}\right)\left(\frac{A}{1 + s\tau_i}\right)^n . \tag{2.22}$$

Finally, the shaped signal is digitized by an analog-to-digital converter (ADC) for subsequent storage and analysis. In designing ADCs, a compromise between resolution and speed, as well as power and speed needs to be found. In general, the optimal design of all described components is a question of the experiments specifications and requirements and hence highly application-specific.

2.8 Silicon microstrip sensors

Segmented strip sensors are the technology of choice for large-area tracking detectors in HEP, in places where highest spatial resolution is not required. For highest spatial resolution in the vicinity of the interaction point one relies on pixelated detectors. Figure 2.7 shows a simplified sketch of an n-type AC-coupled single-sided strip detector. One side of the detector is segmented into strips while the backside is covered by a planar electrode forming an ohmic contact. The implanted strips are read out by segmented aluminum electrodes. A thin insulating layer of oxide, typically SiO_2, Si_3N_4, or a combination of both, provides AC-coupling between the implants and the readout electrodes. Compared to SiO_2, Si_3N_4 offers higher coupling capacitance at the same thickness. To avoid signal loss, the coupling capacitance must be sufficiently high in comparison to the backplane and interstrip capacitance.

N-bulk strip detectors come in two variants, namely p–on–n or n–on–n strips. In p–on–n, the p^+-implants are naturally self-isolating in the n-bulk environment. In n–on–n detectors, the n^+-strips require additional insulation due to the presence of an electron accumulation layer at the Si–SiO_2 interface, which is caused by positive trapped charges in the oxide. Two interstrip isolation techniques are available: p-spray and p-stop. The first is a blanket shallow implantation of a relatively low dose of p-doping to compensate for the positive oxide charge and to prevent electron accumulation. The latter is an implantation of a narrow p^+-line surrounding the n-strip and breaking the electron accumulation layer between individual strips [63]. Both techniques can be combined, which is then called moderated p-spray.

Segmentation is taken to another level by double-sided processing where the detector is segmented on the backside as well, as shown in Figure 2.8. Double-sided readout increases the position information, improves compactness, and minimizes material budget. Again, the n^+-strips need additional insulation [64]. The spatial resolution of a Si strip sensor depends on the strip pitch p and the particular way the sensor is used. In the case of binary hit/no-hit information only, the differences of measured to true positions are Gaussian-distributed with

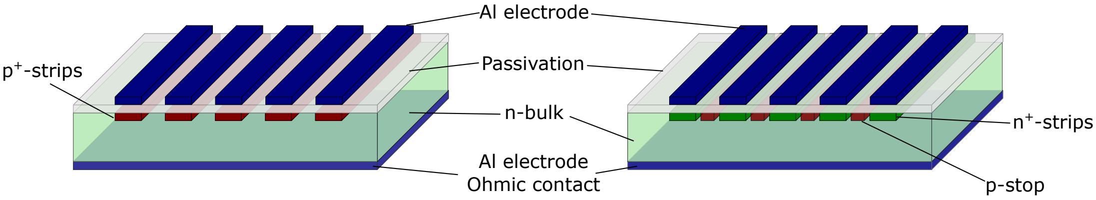

Figure 2.7: Simplified 3D sketch of n-type, AC-coupled single-sided strip detectors. Left: p–on–n sensor. Right: n–on–n sensor. The n-type strips require an additional implanted p-type insulation. Dimensions not to scale.

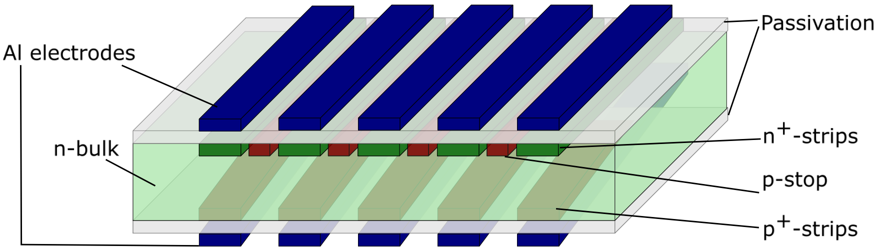

Figure 2.8: Simplified 3D sketch of an n-type, AC-coupled double-sided strip detector with a small stereo angle between n-side and p-side strips, such as used in the STS. Dimensions not to scale.

a standard deviation of

$$\sigma^2 = \int_{-p/2}^{p/2} \frac{x^2}{\Delta x} dx = \int_{-p/2}^{p/2} \frac{x^2}{p} dx = \frac{p^2}{12}, \tag{2.23}$$

so the rms resolution is $p/\sqrt{12}$. In reality, lateral charge diffusion distributes the created charge over multiple strips. Accounting for such charge sharing in analog readout, the optimal resolution is eventually limited by noise and the physics of charge deposition. The obtainable resolution is [65]

$$\sigma = \beta \frac{N}{S} p\,. \tag{2.24}$$

Empiric values for the proportionality constant β are between 4 and 10. The factor $\frac{N}{S}$ denotes the inverse SNR.

3 CBM Silicon Tracking System

The CBM detector is a multi-purpose detector measuring hadrons, electrons, and muons in elementary nucleon and heavy ion collisions over the full FAIR beam energy range of up to 29 GeV for protons, up to 11 AGeV for Uranium beams, and up to 15 AGeV for beams of $N = Z$ nuclei. Most signatures sensitive to dense nuclear matter, which have been discussed in section 1.5, such as dileptons, multi-strange (anti)-hyperons, or charmed particles have a very small production cross section at the relevant beam energies. Moreover, taking data to measure multi-differential cross sections with sufficient precision is extremely statistics-demanding. Hence, rate capability is the critical feature of any experiment investigating dense nuclear matter.

CBM is a fixed-target experiment that will run at interaction rates between 100 kHz up to unprecedented interaction rates of 10 MHz for selected diagnostic probes such as charmonium. The interaction rates of CBM and a variety of other existing or planned HIC experiments are shown in Figure 3.1 as a function of center-of-mass energy. The multiplicity of charged particles is up to 700 per central Au–Au event within the detector acceptance. The experimental

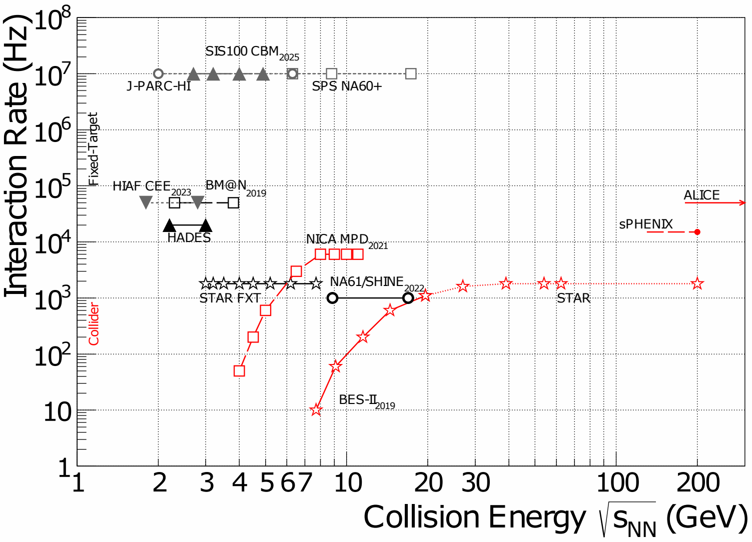

Figure 3.1: Interaction rates of various existing or planned heavy-ion collision experiments as a function of center-of-mass energy. Red symbols show collider experiments, black and grey symbols show fixed-target experiments. From [66].

challenge is to combine a large-acceptance, radiation-hard, and fast detector setup with a high-speed data readout system. Due to complex decay topologies of weakly decaying particles like hyperons or D mesons, no hardware trigger signal can be used. Instead, the full events have to be reconstructed and the decay topology has to be identified online by fast algorithms running on a high-performance computing farm. To utilize maximum rates, the data acquisition is based on self-triggered frontend electronics that deliver time-stamped signals from the individual detector channels without event correlation.

The implementation of the above-mentioned requirements led to the CBM experimental setup, which is briefly described in the following section 3.1. Since this work is based around the detector modules of the STS, the STS will be discussed in more detail in section 3.2, followed by the description of the detector module and its components in section 3.3.

3.1 CBM experimental setup

The full CBM experimental setup, including HADES (High-Angle Di-Electron Spectrometer), is shown in Figure 3.2. Dielectrons and hadrons, including multi-strange hyperons, can be reconstructed with HADES. With its large polar angle acceptance ranging from $18^\circ < \Theta < 85^\circ$, HADES is well suited for reference measurements with proton beams and heavy ion collision systems with moderate particle multiplicities, such as Ni–Ni or Ag–Ag at the lowest SIS100 energies.

The CBM detector system features a fixed-target geometry accepting polar emission angles between $2.5^\circ < \Theta < 25^\circ$ in order to cover midrapidity and the forward rapidity hemisphere for symmetric collision systems at beam energies between 2 AGeV to 40 AGeV. The CBM experimental setup comprises the following components:

- Superconducting 1 T m dipole magnet [67].
- Micro-Vertex Detector (MVD): Four layers of monolithic active pixel sensors (MAPS) inside the magnetic field between the target and the STS. The MVD provides a position resolution of 3.5 µm to 6 µm for high-precision measurements of the primary vertex and of secondary decay vertices close to the target, e.g., from open charm decays ($c\tau =$ 123 µm for D^0) [68].
- Silicon Tracking System (STS): Eight stations of double-sided silicon microstrip sensors arranged inside the magnetic field, located 0.3 m to 1 m downstream of the target to provide charged particle tracking with a relative momentum resolution of $\Delta p/p \approx 1.5\,\%$ at p =1 GeV/c [69].
- Ring Imaging Cherenkov detector (RICH) comprising a CO_2 radiator and a UV photon detector realized with multi-anode photomultipliers for electron and positron identification and pion suppression [70].
- Muon Chamber (MUCH) system for muon identification consisting of five triplets of Gas Electron Multipliers (GEM) sandwiched between hadron absorber plates made of graphite and iron with a total thickness equivalent to 13.5 times the hadronic interaction length λ [71].

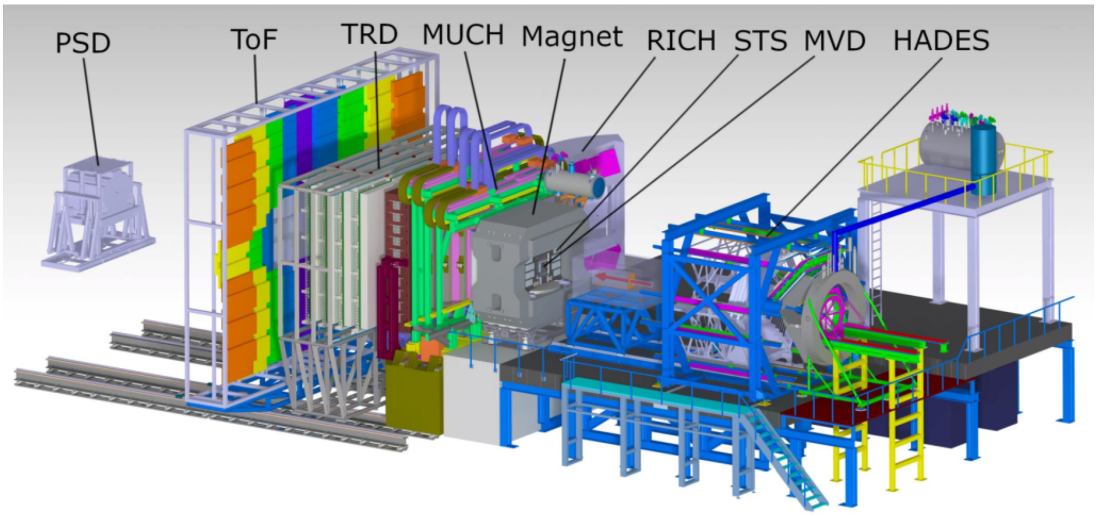

Figure 3.2: The CBM Day−1 configuration (2025) including the HADES detector. The subdetectors of CBM are indicated in the image. Figure courtesy of GSI.

- Transition Radiation Detector (TRD) for pion suppression, particle tracking, and identification of energetic electrons and positrons using specific energy loss [72].
- Time-of-Flight wall (TOF) for hadron identification based on Multi-Gap Resistive Plate Chambers (MRPC) with low-resistivity glass, for high-rate operation (up to 25 kHz cm^{-2} with a time resolution of 50 ps) with an active area of 100 m^2 located about 7 m downstream of the target [73].
- Projectile Spectator Detector (PSD) for measuring non-interacting projectile nucleons for event characterization. The PSD is a forward hadron calorimeter located 10 m downstream of the target and will be used to determine the centrality and the reaction plane angle of the collision [74].
- First-Level-Event-Selection (FLES) system for online event reconstruction and selection. Track reconstruction is based on parallel track finding and fitting algorithms, implementing the Cellular Automaton and Kalman Filter methods [75].

The RICH detector and the MUCH system will be used interchangeably within the muon-hadron or electron-hadron configuration, respectively. All detector systems are equipped with self-triggered readout electronics. After data compression and conversion into optical signals, the data are delivered via about 100 m long fibres to the FAIR high performance computing cluster ("Green-IT cube"), where the event selection will be performed. At high-rate operation, a data volume of about 1 Tbyte/s will be delivered to the FLES and about 1 Gbyte/s will finally be recorded.

The readout electronics generate a timestamp for each signal, which is used, together with the 3D position information, to reconstruct first the particle tracks and then the events. Finally, the particles will be identified based on the track topology, the time-of-flight information, and, in case of the leptons, using the particle ID information from RICH, TRD, and MUCH. The

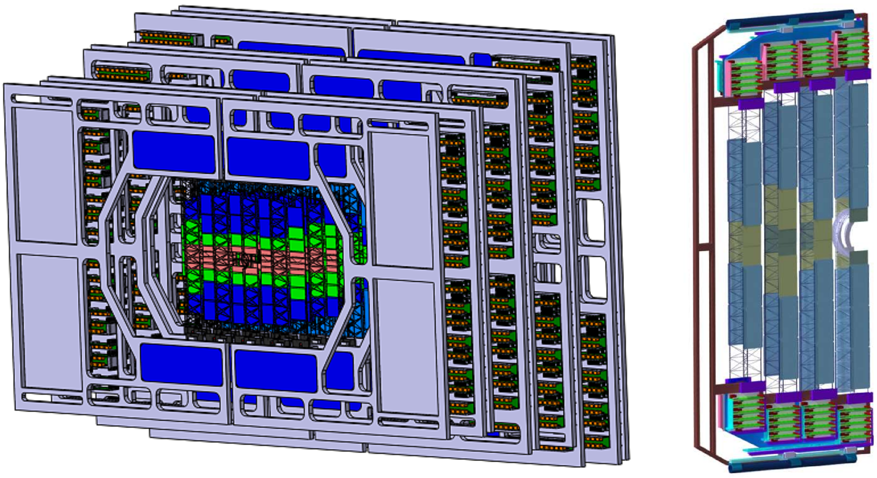

Figure 3.3: STS detector conception (left). Half-station (right). Figures courtesy of GSI.

entire reconstruction chain is performed online by high-speed algorithms which run on a high-performance computing farm.

3.2 Silicon Tracking System

The STS is the key detector for measuring the momentum and tracks of up to 700 charged particles produced in central Au–Au collisions. Due to the required momentum resolution for the STS of $\Delta p/p \approx 2\%$, the material budget of STS has to be minimized to reduce multiple Coulomb scattering and the production of delta electrons. In order to keep the read-out electronics, cooling and mechanical infrastructure out of the detector acceptance, the sensors are connected to the self-triggering frontend electronics using low-mass flexible microcables with a length of up to 50 cm. In combination with the large double-sided sensors with a maximum size of up to 124 mm × 62 mm, the detector module becomes a highly complex structure, which in turn leads to a challenging module assembly procedure. Figure 3.3 shows a sketch of the STS setup. The STS comprises eight tracking stations equidistantly spaced 30 cm to 100 cm downstream of the target [69]. Each station is composed of two half-stations mounted on mechanical ‘C’-shaped frames, as shown on the right of Figure 3.3. The half-station contains several low-mass carbon fiber support ladders with a length from 480 mm to 970 mm. They are the central mechanical components onto which the Si sensors, integrated into detector modules, are mounted inside the physics aperture of the STS detector. Their task is to keep the sensors in their assigned geometrical position with high mechanical precision and stability. Averaged over the whole ladder area, the carbon fiber carrier contributes a radiation length of

$$X/X_0^{avg} = \frac{14.8\,\mathrm{g}}{120\,\mathrm{cm}\cdot 6.15\,\mathrm{cm}\cdot 42.7\,\mathrm{g\,cm^{-2}}} = 0.047\,\%$$

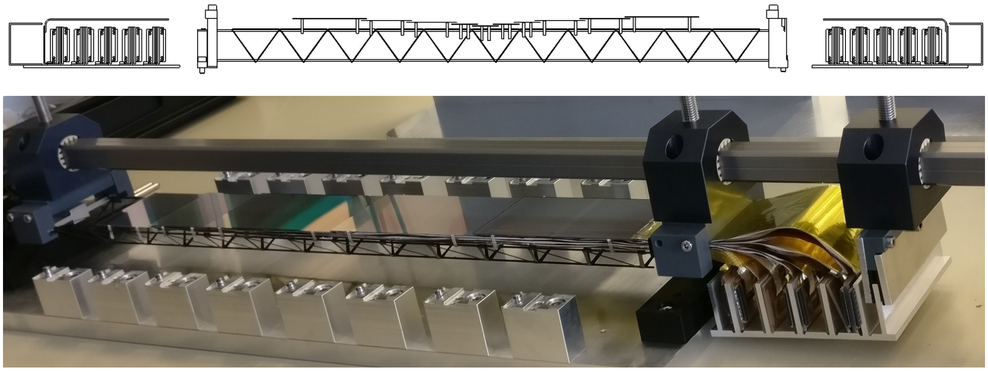

Figure 3.4: Top: Side view sketch of the STS detector ladder, with carbon fiber carrier and mounting structures at both ends. The sensors are attached in a staggered manner, starting from the middle of the ladder. From [76]. Bottom: Half-ladder fully assembled with dummy modules. From [77].

Table 3.1: Quantities of key STS components.

Stations	Ladders	Modules	FEBs	ASICs	Microcables
8	106	896	1792	14 336	14 336/28 672

Each ladder hosts eight to ten detector modules. The readout electronics are located at the periphery—outside of the detector acceptance.

The ladder design, including mounting structures and boxes for the frontend boards (FEBs) at both ends, is shown in Figure 3.4. Also shown is a half-ladder with five dummy modules assembled at GSI. For the full STS, a total of 876 modules are glued to 106 ladders coming in 19 variations. More information about the carbon fiber ladders can be found in [76]. Table 3.1 summarizes the number of components necessary to build up the STS.

3.3 STS detector module

The fundamental functional unit of the STS is the detector module. Each module comprises a double-sided Si microstrip sensor, which is connected to the readout electronics using low-mass flexible microcables with a length of up to 50 cm. The frontend electronics are implemented as Application Specific Integrated Circuits (ASICs). A total of 16 ASICs are connected to the sensor by 16 or 32 microcables. The ASICs are attached to two frontend boards type 8 (FEB-8), each carrying eight chips. Figure 3.6 shows a complete module assembled at GSI. Module assembly can be divided into four major steps, as depicted in the flow diagram in Figure 3.5.

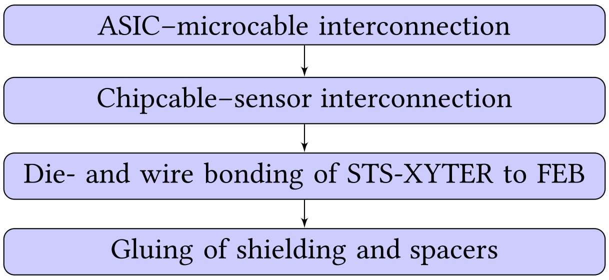

Figure 3.5: Flow diagram of STS module assembly.

Figure 3.6: STS detector module comprising 50 cm aluminium microcables and a 6.2 cm × 6.2 cm sensor. Image courtesy of GSI.

3.3.1 Silicon microstrip sensor

The STS employs double-sided silicon microstrip sensors. Each sensor is segmented into 2048 strips; 1024 strips on the opposing n– and p-side, respectively. The strip pitch is 58 µm and the bond pad size is 60 µm × 180 µm. Four main sensor sizes are deployed, all being 62 mm wide and 22, 42, 62, and 124 mm long. While the n-side strips are oriented parallel to the edge of the sensor, the p-strips are tilted by a 7.5° stereo angle with respect to the n-strips. Figure 3.7 shows a close-up of the p-side of the sensor. In case of a 62 mm × 62 mm sensor, the angled p-strip crosses $\tan\alpha \cdot L/p \approx 136$ strips, so the number of ghost hits is greatly reduced compared to a 90° stereo angle, where the p-strip would cross all 1024 n-strips.

During R&D, the CBM collaboration examined two sensor vendors, CiS Forschungsinstitut für Mikrosensorik GmbH, Erfurt, Germany and Hamamatsu Photonics, Japan. While the overall sensor design is the same for both vendors, small differences in processing and implementation of the STS requirements lead to slightly varying sensor characteristics. As CBM finally opted for the Hamamatsu sensors for series production, all values given in this section are valid for Hamamatsu sensors. However, it should be noted that during the course of this work, CiS sensors have been employed in prototyping.

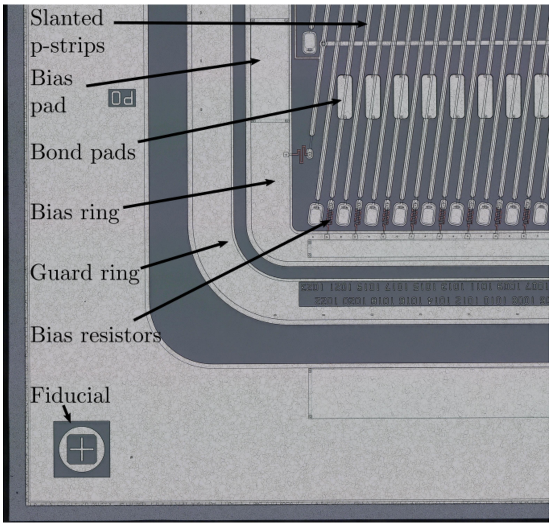

Figure 3.7: Microscopic image of the p-side of a Hamamatsu sensor illustrating the 7.5° stereo angle.

Hamamatsu uses n-type float zone Si with a <100> crystal surface orientation. Bulk resistivities range from 2.5 kΩ cm to 8 kΩ cm [78]. The sensor thickness is 320 ± 15 µm. The strip implants (p+, n+) are 10 µm wide and each strip is connected to the bias line with a poly-Si resistor. The strips are AC-coupled to the readout electrodes via a thin SiO_2 insulation layer. The inclination on the p-side creates shorter strips towards the corners of the sensor. These shorter strips, called z-strips, are interconnected via a second metal layer with their counterparts on the opposite sensor side to form full-length strips which then can all be read out from the same edge. The strips' metal-1 layer is 22 µm wide, metal-2 is 20 µm wide. The layer thickness is 1.5 µm (metal 1 and 2), yielding a resistance $R = 9\,\Omega\,\text{cm}^{-1}$.

Guard rings shape the field inside the sensitive area to minimize edge effects and to guarantee a defined homogeneous potential for all strips, including the edge ones. The guard rings are p− and n-type implants, DC-coupled to aluminium electrodes on floating potential [79]. The p-side guard rings are self-isolating and act as staged potential degraders. Multiple floating guard rings are applied on the n-side as well, as the sensors will be biased with positive and negative voltage symmetric to the virtual ground in the middle of the sensor thickness. No p-spray/p-stop is present on n-side guard rings. Above full depletion they act as one wide guard ring due to being shorted by the electron accumulation layer below the surface oxide.

Table 3.2 summarizes important parameters measured for the Hamamatsu sensors, namely coupling capacitance C_C, backplane capacitance C_b, interstrip capacitance C_{is}, full depletion voltage V_{fd}, breakdown voltage V_{bd}, and leakage current I_{leak} at room temperature before irradiation [80]. A contactless, optical 3D metrology system has been developed at GSI for the optical quality assurance of the sensors before modules assembly [81, 82]. The following failure modes can be found: pinholes, leaky strips, implant/metal breaks and shorts, or poly-Si breaks. The acceptance limit for STS is a maximum of 1.5 % bad strips per sensor.

Table 3.2: Hamamatsu float zone <100> sensor parameters [80].

$\mathbf{C_{C,p}}$ / $\mathbf{C_{C,n}}$	$\mathbf{C_b}$	$\mathbf{C_{is,p}}$ / $\mathbf{C_{is,n}}$	$\mathbf{V_{fd}}$	$\mathbf{V_{bd}}$	$\mathbf{I_{leak}}$
10 / 11 pF cm^{-1}	0.19 pF cm^{-1}	0.36 / 0.37 pF cm^{-1}	51 V	550 V	7 nA cm^{-2}

Following from eqs. (2.11) and (2.14) on page 20), the depletion voltage $V_{fd,diode}$ and backplane capacitance per unit length $C_{b,diode}$ of a planar diode with width p and thickness d are

$$V_{fd,diode} = \frac{eN_{eff}d^2}{2\epsilon} = \frac{d^2}{2\epsilon\mu_n\rho_n} \qquad\qquad C_{b,diode} = \epsilon\frac{p}{d}\,. \tag{3.1}$$

With hadron irradiation, the effective doping concentration for n-type Si can be parametrized as [83]

$$N_{eff} = N_0 \mathrm{e}^{-c\Phi} - \beta\Phi\,. \tag{3.2}$$

Here, the first term describes the creation of vacancy-P complexes which reduce the number of active donors. The latter term describes the creation of acceptor states by negatively charged divacancy complexes. The coefficient c can be interpreted as a donor removal cross-section while β is the probability of acceptor state creation by a hadron per unit path length in Si. The effective doping concentration N_{eff} is usually determined by measuring C-V curves.

For a segmented strip detector, the width w of the strip is smaller than the pitch p. This modifies both $V_{fd,diode}$ as well as $C_{b,diode}$. For a double-sided strip detector with strip widths w_p and w_n for p- and n-side, a semi-analytical solution of the Poisson equation yields [84].

$$V_{fd} = V_{fd,diode}\left(1 + 2\frac{p}{d}\left[f(w_p/p) + f(w_n/p)\right]\right)\,. \tag{3.3}$$

$$C_b = C_{b,diode}\frac{1}{1 + \frac{p}{d}\left[f(w_p/p) + f(w_n/p)\right]} = \epsilon\frac{p}{d + p\left[f(w_p/p) + f(w_n/p)\right]}\,. \tag{3.4}$$

Here, $f(w/p) = f(x) = -0.00111x^{-2} + 0.0586x^{-1} + 0.240 - 0.651x + 0.355x^2$. The implant width of the STS strips is 10 µm for the n- and p-strips. With the pitch of 58 µm, $f(w/p) \approx 0.44$.

Inserting the width and pitch values of the STS sensors results in a backplane capacitance of 0.162 pF cm^{-1} and depletion voltages of 59.92 V, 95.87 V, and 191.74 V for bulk resistivities of 8 kΩ cm, 5 kΩ cm, and 2.5 kΩ cm, respectively. In reality, the situation is more complicated, V_{fd} is slightly dependent on implant depth and metal-to-implant area. The equation is therefore a good starting point, but a calibration measurement should be done for each new sensor type and its diode on the same wafer [51].

The relevant parameter for the electronic noise is the total strip capacitance. As the overall system noise strongly depends on the total capacitance seen by the input of the CSA, it is worthwhile to estimate it. Electrostatic simulations predict a linear dependence of the total strip capacitance on strip width w for a given pitch p [85]. For a 50 µm pitch

$$C_{tot} = \left(0.9 + 1.4\frac{w}{p}\right)\left[\mathrm{pF\,cm^{-1}}\right] \quad , \tag{3.5}$$

which for STS results in a predicted total capacitance of 1.14 pF cm^{-1}. In general, n$^+$-strips have a larger capacitance than p$^+$-strips since the charge accumulated between n$^+$-strips makes the n$^+$-cathode effectively larger.

The breakdown voltage for a one-sided abrupt junction is

$$V_{bd} = E_m \cdot d/2\,. \tag{3.6}$$

Here, E_m is the maximum electric field at breakdown, which for a one-sided abrupt junction can be expressed as [48]

$$E_m = \frac{4\times 10^5}{1-(1/3)\log_{10}(N/1\times 10^{16}\,\mathrm{cm^{-3}})}\left[\mathrm{V\,cm^{-1}}\right]\,. \tag{3.7}$$

With $N = 10^{12}$ cm^{-3} and $d = 320$ µm, this results in the estimated breakdown voltage of 1570 V for the STS sensors. However, in junctions formed by a planar process, an important edge effect should be considered. At the junction perimeter with relatively sharp edges in the doping distribution, the depletion region is narrower and the electric field is higher. Hence, the avalanche breakdown voltage is determined by these regions and the actual breakdown voltage will be smaller than the above calculated value.

3.3.2 Frontend ASIC

The frontend ASIC is developed at AGH University of Science and Technology, Cracow, Poland. The STS-XYTER2 is a 128-channel readout ASIC designed for STS and MUCH, It is therefore also called STS/MUCH-XYTER2 or short SMX2. The naming convention in this thesis however will be STS-XYTER2. Its predecessor is the STS-XYTER [86]. The STS-XYTER2 provides self-triggered 14-bit time and 5-bit energy measurement, as well as serialized streaming of the digitized data. The chip is processed in UMC CMOS 180 nm technology and has the dimensions 10 mm × 6.75 mm. Figure 3.8 shows an image of the chip.

The block diagram of a single processing channel is shown in Figure 3.9. The current pulse $i(x)$ generated by charged particles in the active sensor volume is integrated by the CSA. The CSA output signal is fed to the Polarity Selection Circuit (PSC). The PSC is required to handle negative as well as positive signals emerging at opposite sides of the double-sided sensors. The PSC output signal is then split into two paths—the slow and the fast path—optimized for energy and timing measurements, respectively. Using two different, parallel signal paths in a single processing channel has been implemented before, e.g. in the n-XYTER ASIC [87]. Compared to the n-XYTER, the STS-XYTER2 contains an ADC in each channel, a timestamp validation functionality, CSA reset circuitry, and has much lower power consumption.

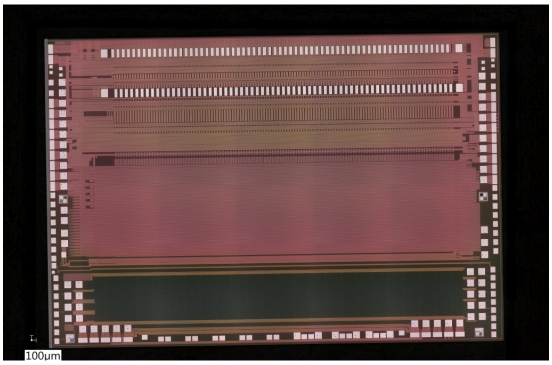

Figure 3.8: Microscopic image of the STS-XYTER 2.1 readout ASIC.

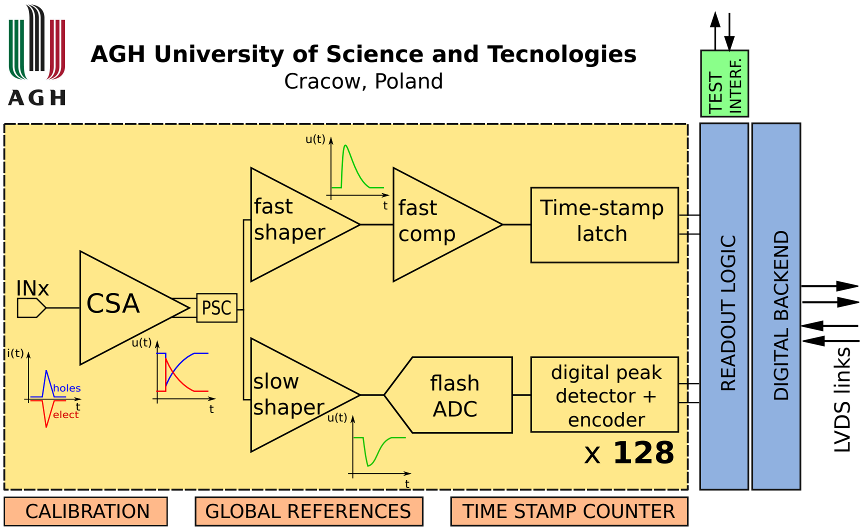

Figure 3.9: Block diagram of a single processing channel of the the STS-XYTER2 readout ASIC.

The fast path includes a fast CR-RC shaper with a peaking time of $\tau_p = 30\,\text{ns}$, a discriminator, and a timestamp latch. The fast path is optimized to determine the input charge arrival time with a timing resolution of approximately 4 ns. The slow path is optimized for accurate energy measurement. It contains an approximate CR-(RC)^2 shaper with variable peaking times of $\tau_p = 90$, 160, 220, and 280 ns, a 5-bit flash ADC, and a digital peak-detection logic. The ADC digitizes the amplitude at the slow shaper output to compensate the time-walk effect and increase timestamp accuracy.

The digital backend provides time pre-sorting, monitoring, and throttling features as well as multiple 320 Mbit/s serial links for a GBT[1]-based DAQ structure. More information about the chip can be found in references [88, 89, 90]. The current ASIC revision STS-XYTER was

---

[1] GigaBit Transceiver

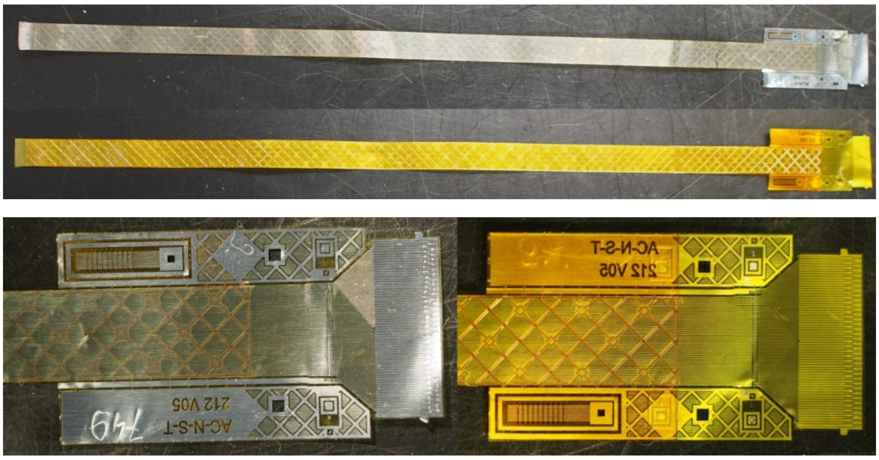

Figure 3.10: Top: Frontside and backside of the aluminium microcable. Bottom: Close-up of the bond area including the technological zone for testing of the chipcable.

thoroughly characterized as part of this work. The results will be presented in chapter 6 on page 75.

3.3.3 Low-mass microcables

Sensor and ASIC are connected by low-mass flexible microcables with a length of up to 50 cm. To avoid later confusion, it needs to be stressed that two types of microcables are mentioned in this work. On one side, there is the initially developed and primarily used *aluminium microcable* [91]. Fully functioning modules have been produced at GSI following the full quality assurance protocol [92]. As with most technologies, especially in such a cutting-edge project, there are certain downsides and risks associated with the aluminium microcable and the corresponding interconnection technology. These will be discussed in chapter 4. Thus, these considerations have led to the development of another type of microcable based on copper signal lines. The work done for this thesis was focused on the *copper microcable* which will be described in detail in chapter 4.

In order to appreciate the differences and similarities between the cables, the aluminium microcables are briefly described now. Figure 3.10 depicts an aluminium microcable. Each microcable is divided into 64 channels with a bond pad pitch of 116 µm. This results in $2048/64 = 32$ cables that have to be connected to each sensor. The 64 aluminium traces with a thickness of 14 µm sit on top of a 10 µm thick polyimide (PI) substrate, which sits on top of a 75 µm thick meshed-PI spacer. A summary of the aluminium cable dimensions is given in Table 3.3.

On each sensor side, two microcable layers have to be placed on top of each other. This setup has a radiation length of

$$X/X_{0,tot} = 2 \cdot 10\,\mu\text{m}/X_{0,PI} + 2 \cdot 14\,\mu\text{m}/X_{0,Al} \cdot A_{Al}/A_{tot} + 2 \cdot 75\,\mu\text{m}/X_{0,mesh} = 0.03\%\,, \quad (3.8)$$

Table 3.3: Aluminium microcable dimensions. The thickness of the meshed spacer, the PI layer, and the aluminium strip are denoted by d_{mesh}, d_{PI}, and d_{strip}. The strip width is denoted by w_{strip}. Units are in µm.

Length	Width x Height	d_{mesh}	d_{PI}	d_{strip}	w_{strip}	Bond pitch
1.5 to 5×10^5	7.5×10^4 x 99	75	10	14	30	116

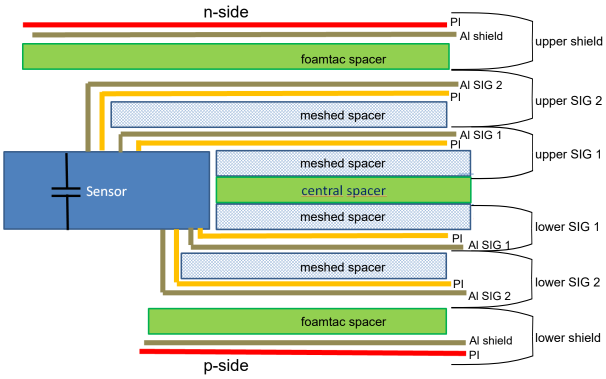

Figure 3.11: Complete aluminium microcable stack including spacers and shielding.

where A_{Al}/A_{tot} is the surface fraction covered by the aluminium signal lines and X_0 denotes the radiation length of the respective material. The full stack of microcables per module including shielding and spacers is shown in Figure 3.11. Considering a ladder of ten modules, five of those cable stacks add up on the periphery. This leads to a significant amount of material that has to be bent by 90° to accommodate the FEBs inside the FEB cooling boxes. The full stack-up of five stack layers should not exceed 5 mm including some safety margin.

As the total noise in a detector channel strongly depends on the total capacitance connected to the input of the CSA, the microcable capacitance is a critical contributor to the overall system noise. The optimal microcable stack is the one with the lowest capacitance still satisfying the geometrical constraints inside the FEB cooling boxes. The capacitance of the microcable stack has been studied extensively [93], resulting in the materials and parameters presented in Table 3.3. The simulation results for the inner and outer signal layer are $0.387\,\mathrm{pF\,cm^{-1}}$ and $0.367\,\mathrm{pF\,cm^{-1}}$, respectively. Measurements of a single microcable layer with an LCR meter at GSI revealed a stray capacitance of $0.38\,\mathrm{pF\,cm^{-1}}$ between signal traces, in great agreement with the simulations. During the measurement, the shielding and all lines were put on GND while one line was measured with respect to GND potential.

Microcable and die are interconnected by aluminium–aluminium Tape Automated Bonding (Al–Al TAB) [94, 95]. Al–Al refers to the fact that an aluminium signal line is bonded to an aluminium bond pad. TAB is a simple process that is sketched in Figure 3.12. A dedicated bonding needle pushes the free-floating signal carrier down onto the die and welds it using ultrasonic power and force. Figure 3.13 shows an aluminium microcable connected to a die in

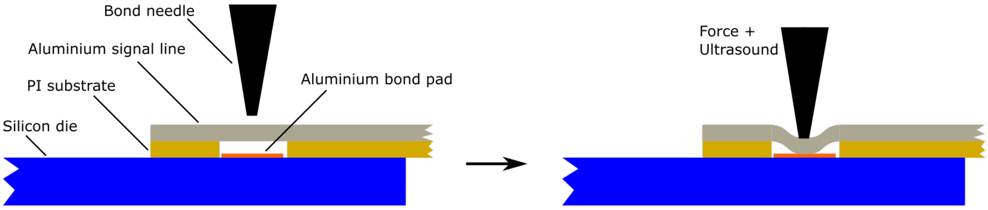

Figure 3.12: The TAB process used for the microcable-to-die interconnection. The bond needle ultrasonically welds the aluminium signal carrier directly onto the aluminium bond pad on the silicon die.

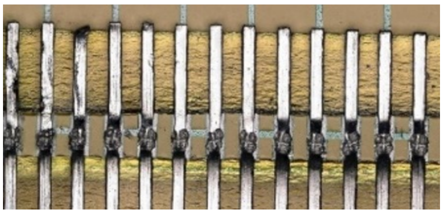

Figure 3.13: Aluminium microcable connected to a die with the TAB process.

the TAB process. After bonding all 64 channels one by one, the interconnection is protected with Epolite FH 5313, a solid, RT-curing, optically clear, electrical grade epoxy glue. Two microcable layers have to be bonded to each ASIC, one over the other.

During module assembly, 32 microcables are connected to 16 STS-XYTER2 first. Afterwards, the ASIC–microcable structures, from now on called chipcables, are connected to the sensor by the same TAB process—eight chipcables per sensor side. While the interconnection technology is the same, handling is considerably more difficult on the sensor side. Here, one deals with a large and complex structure with a total length of up to more than 60 cm with a sensor on one end and multiple ASICs on the other end. After eight chipcables have been connected to the p-side of the sensor, the whole structure has to be flipped to connect the remaining eight chipcables to the n-side. As the sensor is the most expensive component of the module, extreme care must be taken at all times.

3.3.4 Frontend board

Each module uses one p-side and one n-side FEB-8. Figure 3.14 shows the current versions of the FEB-8, the FEB-8_A2 (blue, n-side) and FEB-8_B2 (red, p-side). Each FEB-8 hosts eight STS-XYTER readout ASICs. Each ASIC provides up to 5 LVDS data signals (uplinks) with a data rate of 10 Mhits/s per link. The main function of the FEB-8 is to apply appropriate power supply voltages to the ASICs and to provide a capacitively coupled data interface, which establishes the connection of the LVDS lines (clock, downlink and uplinks) to the readout board (ROB) [96]. In the current FEB-8 version, the galvanical isolation of the LVDS signals between the ROB and the sensor bias potential is realized with 36 vertically arranged HV ceramic SMD capacitors (3.3 nF / 500 V), located underneath the ZIF connector (see Figure 3.14).

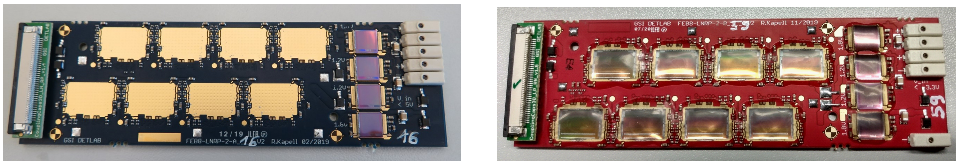

Figure 3.14: FEB-8_A2 (blue, n-side) and FEB-8_B2 (red, p-side) with 2 uplinks per ASIC and the coupling capacitors arranged vertically underneath the ZIF connector at the left.

With this arrangement, these parts are sensitive to lateral forces. Therefore, the capacitors are protected with glob top glue. Future versions will have those capacitors spaced throughout the board to mitigate this risk factor. The boards shown in Figure 3.14 provide two uplinks per ASIC. Most of the frontend boards used for sensor readout at the STS detector are of this kind. For the detector areas where higher data rates arise, the FEB-8_5, providing five uplinks per ASIC, is in development at AGH Cracow [96]. Due to the increase in uplinks, there are 84 signal lines instead of 36.

Additionally, four custom-designed radiation-hard low-dropout voltage regulators (LDOs), manufactured at the Semi-Conductor Laboratory (SCL) in Chandigarh, India, are installed on the FEB-8. They are used to generate stable 1.2 V and 1.8 V as the last element of the supply chain to achieve the required noise power density level for low-voltage powering of the ASIC [97]. The advantages of an LDO over DC-DC regulators include the absence of switching noise, smaller device size, and greater design simplicity.

Since the FEBs-8 are also needed in the copper technology, the process steps in module assembly that include the FEB-8 are described in the following. After arrival, the PCBs are cleaned in a multi-step procedure:

- clean 5 min to 10 min at 50 °C in ultrasonic bath with VIGON US,
- rinse in deionized water,
- clean 5 min in ultrasonic bath with deionized water,
- dry in the oven for 60 min at 60 °C.

Next, the LDOs are die bonded with Epotek E4110 silver glue, which is curable at RT. Bonding of these chips is difficult due to their very small bond pads. After wire bonding of the ASIC to the PCB, Dymax Multi-Cure 9001-E-V3.5 (Dymax 9001) is used as glob top material for wire bond and chip protection. Its benefits include fast curing in a matter of seconds at RT under UV-light exposure, good thermal cycling resistance, excellent adhesion to the FEBs, and good electrical insulation. At this stage, the FEBs are ready for module assembly.

ASIC-to-FEB bonding must be performed row-by-row due to accessibility. First, four STS-XYTER2 are die bonded to the row closer to the sensor on the FEB-8. Curing is accelerated by heating to 70 °C for 2 h. The chips are wire bonded and tested for basic communication and functionality. If the tests are successful, the chips are glob topped also with Dymax 9001. The ASIC shielding for the first row is soldered to the FEB. Next, the row of ASICs further from the sensor is handled in exactly the same way. As soon as both FEBs-8 are complete with successful tests on each ASIC, the module shielding is glued and soldered to the FEBs-8.

4 Development of High-Density Interconnects for Copper Microcables

4.1 Motivation

The primary assembly technology for STS is the Al–Al TAB process based on aluminium microcables. Several modules with varying cable lengths including the longest 50 cm ones and sensor sizes of up to 62 mm × 124 mm have been produced in the Al–Al TAB technology. Still, there are some downsides to the technology. The individual microcable alignment is a manual process that requires skilled personnel and time. Reworking is possible only for individual connections, not a full cable at once. Additionally, aluminium-on-polyimide flex technologies at those fine pitches are not common in industry. The CBM-STS collaboration found one single cable supplier in LTU Ltd, Kharkov, Ukraine. At a certain point in time a sufficient microcable yield and throughput for series production could not be guaranteed. Therefore, the collaboration was looking for alternative solutions.

As a result, a double-layered copper-polyimide flexible microcable has been designed and produced at KIT [98]. Its design and characterization are described in section 4.3. Based on the copper microcable, a novel high-density interconnection technology has been developed [99]. It comprises fine-grain solder paste printing on the microcable and gold stud bumping on the die. It combines a high automation capability with good mechanical and electrical properties making it an interesting technology also for future detector systems. The individual processing steps are described in detail in section 4.5.

4.2 Requirements

Any alternative assembly solution must bear comparison with the established Al–Al TAB technology. From the physics point of view, minimal material budget is a necessity. Apart from physics requirements, practical considerations surrounding the module assembly and integration as well as long-term reliability are important. Another factor is cost.

For module series production, a technology with high automation capability is desirable to reduce person hours and improve module quality as well as uniformity. The microcable must meet the thermal and mechanical requirements of the interconnection technology and of detector integration. Parameters to consider are the thermal expansion coefficient and the

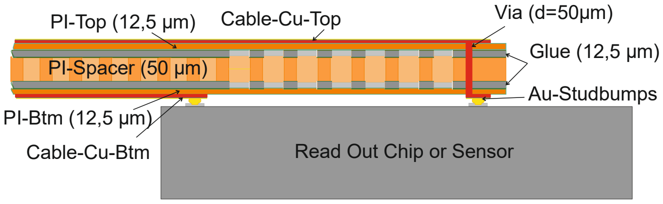

Figure 4.1: Schematic drawing of the developed two-layer Cu microcable connected to a die. The top Cu layer is routed to the bottom side with vias. A meshed-PI interposer reduces the stray capacitance. From [100].

cable stiffness. Sufficient spark protection between the HV sensor edge and the LV microcable needs to be ensured.

Regarding module integration, there are two main areas to consider. The overall cable stack thickness is limited due to spatial restrictions. On top of that, the cables must withstand a 90° bend with varying bending radii down to a few mm in order to accommodate the FEBs in the cooling shelves. The microcable-die interconnection must withstand the CBM lifetime fluence of $1 \times 10^{14}\ \mathrm{n_{eq}/cm^2}$ accumulated over approximately 10 years of operation at $-5\,^{\circ}\mathrm{C}$.

4.3 Copper microcable design and characterization

The aforementioned downsides to the Al–Al TAB technology motivated the design of a new microcable based on copper as the signal carrier. Copper-on-PI flex technologies are widely established in industry. Due to the characteristics of copper and highly sophisticated processing technologies, high yields can be expected which allow wider and multi-layered microcables. In the end, a two-layered copper microcable was developed, resulting in 128 channels per cable. Compared to the Al–Al TAB technology, the higher channel density leads to a reduction in required microcables for the STS by a factor two. Figure 4.1 ([100]) shows the developed copper microcable schematically. Vias route the top Cu line to the bonding site. A meshed-PI interposer with a fill factor of 30 % reduces the stray capacitance while adding only very little material budget. Two staggered rows of 64 pads each enable the connection of 128 channels.

Cross sections of the actual copper microcable can be seen in Figure 4.2. The total thickness of the cable calculates to ≈ 140 µm. The height of the copper traces is ≈ 8 µm. The resulting radiation length was calculated to

$$\begin{aligned} X/X_{0,tot} &= 2 \cdot 12.5\,\mu\mathrm{m}/X_{0,glue} + 2 \cdot 12.5\,\mu\mathrm{m}/X_{0,PI} + 75\,\mu\mathrm{m}/X_{0,mesh} \\ &\quad + 2 \cdot 8\,\mu\mathrm{m}/X_{0,Cu} \cdot A_{Cu}/A_{tot} = 0.05\,\%\,. \end{aligned} \tag{4.1}$$

Here, $A_{Cu}/A_{tot} = 1/5$ is the surface fraction covered by copper, determined by the copper trace width-to-pitch ratio. The radiation lengths of the relevant materials are listed in Table 4.1. While the radiation length is higher compared to the aluminium microcable, it still is

Table 4.1: Radiation length of various materials used in the STS detector module. Data from [101].

Material	Si	Al	Cu	PI	Epoxy	Air (dry, 1 atm)
X_0 (cm)	9.370	8.897	1.436	28.570	32–35	3.094×10^4

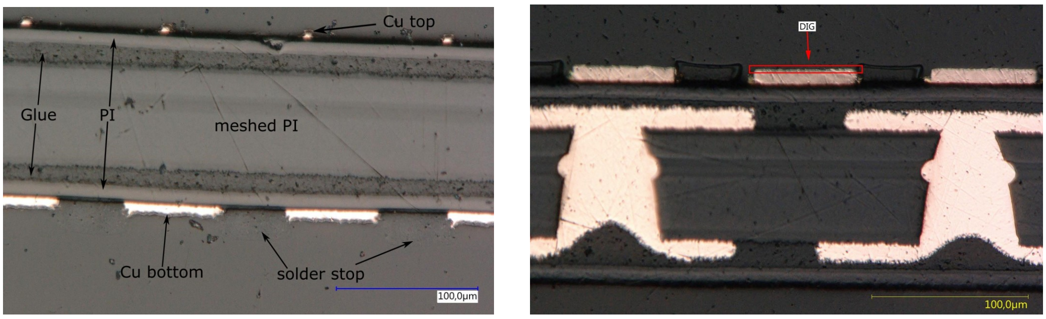

Figure 4.2: Cross sections of the copper microcable. The individual layers are shown on the left. The copper-filled vias and the 200 nm thick gold-plating of the bond pads are shown on the right.

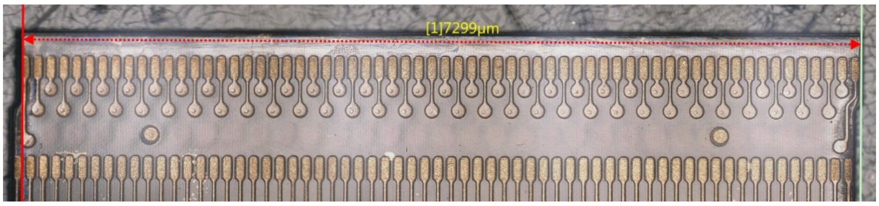

Figure 4.3: Bond area of the double-layered copper microcable showing the 128 bond pads arranged in two staggered rows.

considerably below the sensor itself, which contributes $320\,\mu m/X_{0,Si} = 0.32\,\%$. A top view of the bond area of the cable is presented in Figure 4.3.

4.3.1 Capacitance

Finite Element (FE) simulations have been performed with the goal to minimize the microcable interstrip capacitance. Geometric parameters such as the copper trace width as well as the thickness of the meshed interposer have been varied. The simulation setup and results are displayed in Figure 4.4 [100]. The cable capacitance is shown as a function of meshed-interposer thickness for Cu trace widths of 18, 24, 30, and 36 µm. Based on these results, the trace width was fixed to 24 µm and the thickness of the meshed interposer to 75 µm.

Capacitance measurements have been performed at IPE with a Rohde und Schwarz ZVA24 Network Analyzer with probes in the ground–signal–ground configuration. The network analyzer performs a frequency sweep, sending a sine wave with known power for each

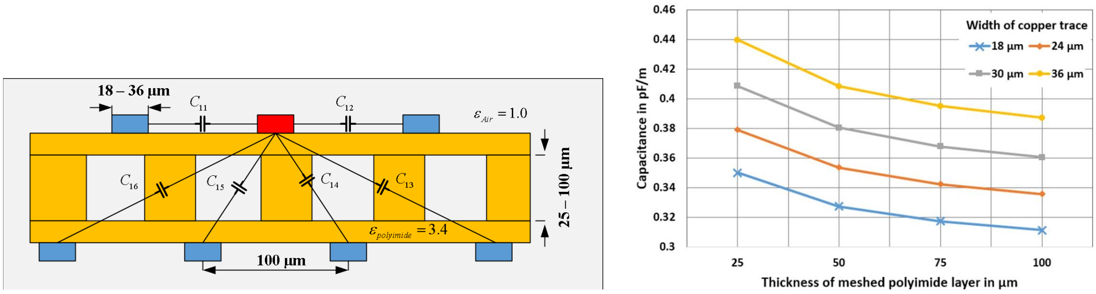

Figure 4.4: The setup for the microcable capacitance FE simulations (left). The line of interest (red) is put to high potential while both neighboring lines and the four lines directly opposite (blue) are put to GND. Image: T. Blank. Results of the FE simulation for varying interposer thickness and different Cu trace widths (right). From [100].

frequency while measuring the reflected signal. For the microcable capacitance measurements, the frequency was swept between 1 MHz to 100 MHz. The capacitance was determined by reading the value from the Smith chart at 10 MHz. During the measurements, the signal line of interest is put on potential, while the neighboring lines left and right and the two lines on the opposite side of the cable are put on ground. The same connection scheme is applied on the far end of the cable to close the current loop. Two signal lines have been measured in this manner with ten repeated measurements each. The capacitance for a 20 cm long microcable was found to be 7.68 ± 0.40 pF, equating to 0.38 pF cm^{-1}.

For comparison, the same measurements have been performed on a 20 cm long aluminium microcable. Here, the signal line of interest is put on potential while the neighboring lines left and right are put on ground. Four signal lines have been measured with ten repeated measurements each. The capacitance was found to be 6.89 ± 0.46 pF, equating to 0.35 pF cm^{-1}. These values will be used in the following sections for calculating the detector module noise based on the capacitive load at the CSA input.

4.3.2 Thermal and mechanical considerations

Besides the electrical performance of the cable, mechanical and thermal requirements must be satisfied, both for module assembly and final detector integration. During detector integration, the FEBs are placed inside the FEB cooling boxes at the periphery of the STS stations at a 90° angle with respect to the sensors and a bending radius down to a few mm. The cables must tolerate the arising forces without damage to the copper traces. Additionally, a higher cable stiffness complicates assembly and integration.

In the copper technology, the die-microcable interconnection involves a soldering process, hence the cables experience high temperatures. First, the mechanical integrity of the cable has to be assured, i.e. delaminations must be avoided. Second, the thermal dilatation of the cable bond region has to be considered so that the bond pads of the cable still coincide with

Table 4.2: Thermal expansion mismatch for various microcable widths from a singular microcable with 128 channels to one wide microcable with 1024 channels for two temperature differences corresponding to peak process temperatures during bonding with conventional solder paste and low–melting point solder paste.

Thermal expansion	Single (Width=7.5 mm)	x 2	x 4	x 8
ΔL_{PI-Si} @ ΔT = 150 K (µm)	19.6	39.2	78.3	156.6
ΔL_{PI-Si} @ ΔT = 220 K (µm)	28.7	57.4	114.8	229.7

the bond pads on the die. In sensor-side interconnection, the cables must physically fit next to each other at the bonding temperature.

For a given material, the change in length has a linear relationship with the change in temperature with a material-specific coefficient of thermal expansion (CTE) α

$$\Delta L = L \cdot \alpha \cdot \Delta T \,. \tag{4.2}$$

The CTE of Si is $\alpha_{Si} = 2.6 \times 10^{-6}\,\mathrm{K}^{-1}$, whereas the CTE of the PI used in the microcable is $\alpha_{PI} = 2 \times 10^{-5}\,\mathrm{K}^{-1}$. Table 4.2 shows the thermal expansion mismatch for various microcable widths from a singular microcable with 128 channels to a hypothetical wide microcable with 1024 channels for two temperature differences corresponding to peak process temperatures during bonding with conventional solder paste and low–melting point solder paste. The thermal mismatch clearly rules out the use of wide microcables, even if they could be produced with an acceptable yield. Besides alignment incompatibilities, the thermal mismatch induces mechanical stress on the interconnection during cool-down. Ideally, the CTE of the microcable should match the one of Si and the process temperature should be as close as possible to RT. The reduction of CTE of PI films is an active area of research. Recent publications claim the development of a novel PI film having an ultra-low CTE of 3 ppm/K [102] or 2.5 ppm/K [103]. The company NeXolve offers Novastrat® 800, a high temperature PI film with a CTE of 4 ppm/K, and Novastrat® 905 with essentially zero CTE. Such materials might be suitable candidates for future developments.

The copper microcable is considerably stiffer than the aluminium microcable. To test the bending resistance of the microcable, a series of test bends has been performed. Cu microcables have been bent by 90° with a 0.5 mm bending radius and by 180° with a 0.5 mm and 1 mm bending radius. The line resistance of multiple lines was measured with a needle prober before and after bending. No increase in line resistance was observed. Optical inspection of the traces revealed no visible damage.

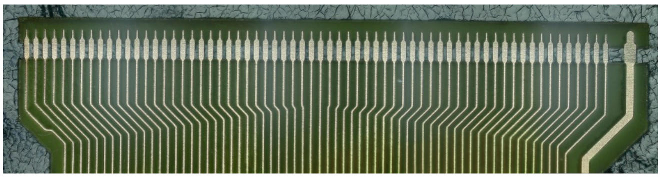

Figure 4.5: Single-layer, 64-channel copper microcable developed for the TAB process.

4.4 Investigations into TAB process for copper microcables

Next to the aforementioned double-layered copper microcable, a single-layered copper microcable with 64 channels has been developed to investigate the possibility to use the TAB process for the copper technology, see Figure 4.5. The Al–Al TAB process produces reliable connections even at RT, as the connection is monometallic. Due to material mismatch, a direct copper–aluminium TAB process will not work, as copper is much harder and has a larger Young's modulus than aluminium. Additionally, copper oxidizes quickly, which requires working under nitrogen atmosphere. Therefore, the copper TAB microcable was plated with a 200 nm gold layer in a Direct Immersion Gold (DIG) process. Gold is much more resistant to environmental contaminants than copper. Still, elevated temperatures and increased bonding force and ultrasonic power are required to achieve a reliable interconnection. The hardness of copper combined with higher bonding parameters bears the risk of damaging the die bond pads.

Several bond tests have been performed with bonding temperatures up to 162 °C, bond forces up to 20 g, ultrasonic current up to 50 mA, and bond times up to 70 ms. The top panel of Figure 4.6 shows a microcable connected to the die before and after a shear test. The shear test resulted in lift-offs and/or cratering, both unacceptable failure modes. The TAB process was subsequently improved by combining it with the gold stud bumping technology. Gold studs are placed on the die first and the microcable is then connected to the studs with the TAB process. In this manner, a monometallic interconnection is achieved.

The lower panel of Figure 4.6 shows a microcable connected to the die in the TAB–gold bump process before and after a shear test. The point of failure moved from the interconnection to the copper trace itself. Shear forces up to 660 g have been reached. While this expressed a significant improvement of the process, cratering was still a major concern. Therefore, and due to time limitations the focus was shifted back to the double-layered copper microcable.

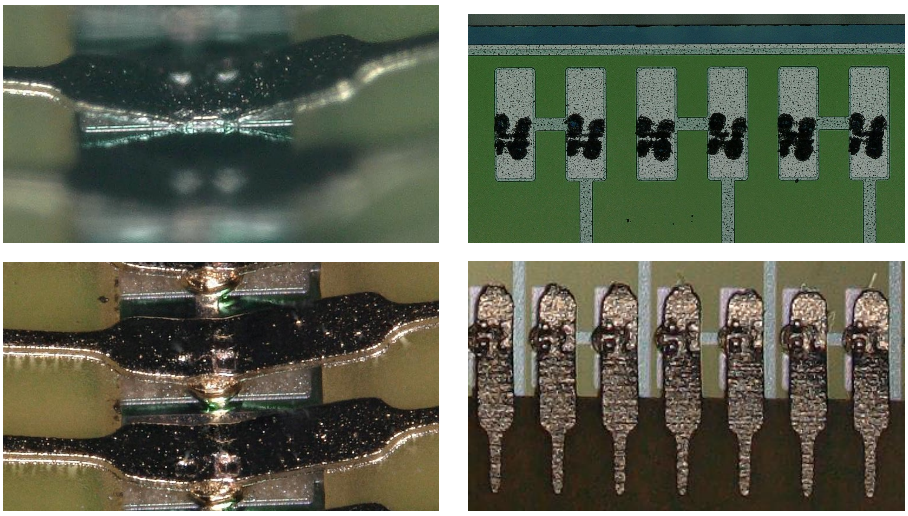

Figure 4.6: Top left: Direct TAB process of a gold-plated copper microcable on a test die. Top right: The shear test reveals a lift-off. Bottom left: TAB process of a gold-plated copper cable onto gold stud bump. Bottom right: The shear test reveals that the point of failure moved to the copper trace itself.

4.5 Novel gold stud–solder interconnection technology

All of the individual processing steps of the novel gold stud–solder interconnection technology are schematically shown in Figure 4.7, as a guideline for the following discussions. As first steps, fine-grain solder paste of type 7 (particle size: 2–11 µm) or type 8 (particle size: 2–8 µm)is printed on the microcable, and gold stud bumps are placed on the ASIC and sensor. Next, the solder paste reflow enables storage in nitrogen compartments and facilitates handling. After successful preparation of the components, the microcable and die are connected in a thermocompression flip chip process to establish the mechanical and electrical connection. Finally, the structure is protected by underfill glue to guarantee spark protection of the low-voltage cable from the high-voltage sensor and to increase mechanical strength and reliability. In the following sections, the individual process steps of the gold stud–solder interconnection technology are described in detail. This includes the general description of the processes, process optimization and automation, quality assurance, and encountered challenges.

4.5.1 Gold stud bumping

Gold stud bump bonding has been described and investigated previously at KIT [104, 105]. It is a low-cost, flexible, and reliable technology. IPE owns a Kulicke & Soffa IConn ball bonder with a placement speed of up to 20 bumps/s. With the help of a dedicated vacuum jig, 16 ASICs can be bumped in less than two minutes semi-automatically. Each sensor side can be bumped in under a minute. For the p-side, the inner staggered pad row is bumped, while

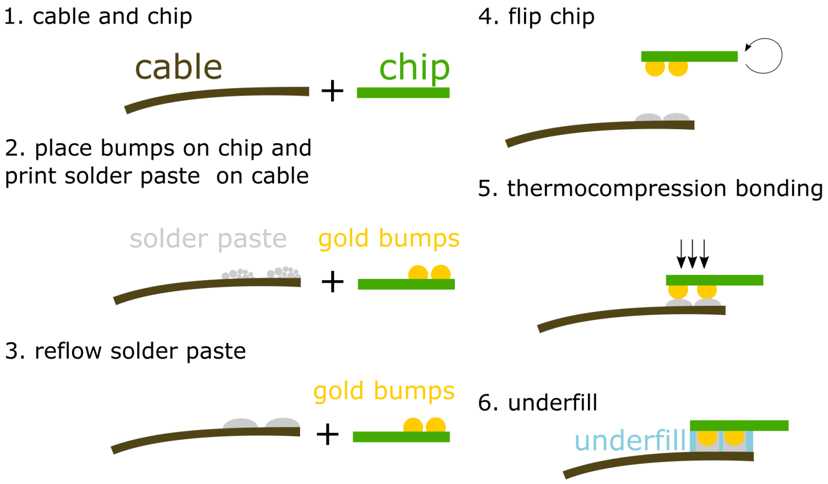

Figure 4.7: Schematic drawing of the individual process steps in the gold stud bump–solder paste interconnection technology.

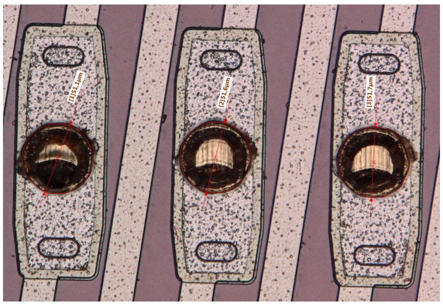

Figure 4.8: Gold studs placed on the p-side of the STS sensor. A gold wire diameter of 23 µm results in a gold stud diameter of 52 µm.

the n-side uses the outer staggered pad row. In this manner, all sensors and ASICs can be prepared quickly for subsequent bonding.

In a typical bump bonding interconnection, gold bumps are placed on both dies which are subsequently bonded in a thermocompression process. However, gold stud bumping on the microcable has been investigated across a wide range of bonding parameters and shown not to lead to a reliable interconnection. The compressibility of the cable is too high for a proper energy transfer to the interconnection site.

For the STS, a gold wire diameter of 23 µm results in a gold stud diameter of 52 µm, providing a maximized interconnection area without creating shorts between neighboring channels. Such gold bumps, placed on the p-side of a CiS sensor, are displayed in Figure 4.8. In order to investigate possible damage created on the sensor during the bumping process, a cross section analysis was performed. Figure 4.9 shows a cross section of a bumped CiS sensor. It was prepared by grinding, fine-polishing, and subsequent ion beam milling in a Hitachi ArBlade 5000 ion milling system. No indication of any kind of damage to the sensor is observable.

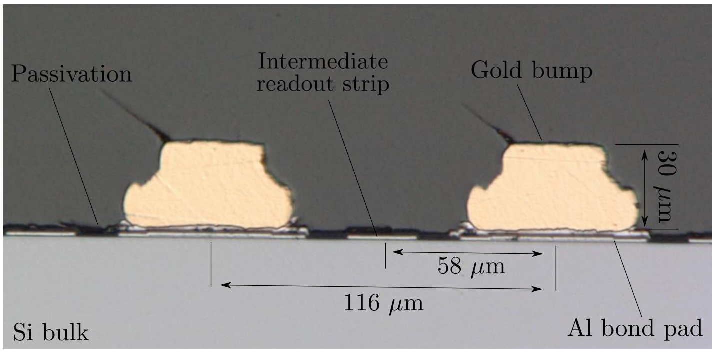

Figure 4.9: Cross section of a CiS sensor after gold stud bumping. There is no indication of any damage to the sensor.

In order to test the strength of the gold bump–die interconnection, shear test analysis was conducted on a CiS sensor (CBM 06, FA-Nr. 331827-7). Shear testing was executed with a Dage Precision Industries Ltd. Series–4000–PXY multi-purpose bondtester. During the test, the shear tool shears through the gold bump at a height of 6 μm with a velocity of 500 $\mu m\,s^{-1}$. The force-time curve and the force required to break the connection are recorded. In case of a strong connection, the gold bump itself is the weakest point. Failure modes to be avoided include ball lift-off, pad lift-off, and cratering.

The shear test results obtained for 48 bump bond parameter combinations (4× temperature, 4× USG (ultrasonic current), 3× bond force) and 20 test bumps each are shown in Figure 4.10. The data is presented in dependence of all three parameters separately to appreciate the influence of the bump parameters more clearly. In the lower panel, three USG–bond force parameter combinations are plotted over temperature. For all three of them, the slope reduces significantly above 175 °C. Based on these results, the temperature was fixed to 175 °C, reducing the parameter phase space for further parameter optimizations. The top panels show the shear strength as a function of USG (80–95 mA) and bond force (25–35 g), respectively. For both USG and bond force, the shear force increases linearly towards larger bond parameters.

Figure 4.11 on page 53 shows a 2D histogram and contour plot of shear strength versus USG and bond force for a bond temperature of 175 °C. One has to pay attention that the optimal parameters are not necessarily the ones that lead to the highest shear force readings. If the bond force and/or USG are chosen too high, the bumps will start to be squashed and express irregularities in shape. The bonding procedure itself becomes unstable and the risk of cratering increases. Hence, for the STS sensor and ASIC a bond force of 30 g and USG of 90 mA was selected. The most relevant bump bonding parameters used for the STS sensors and ASICs are listed in Table 4.3.

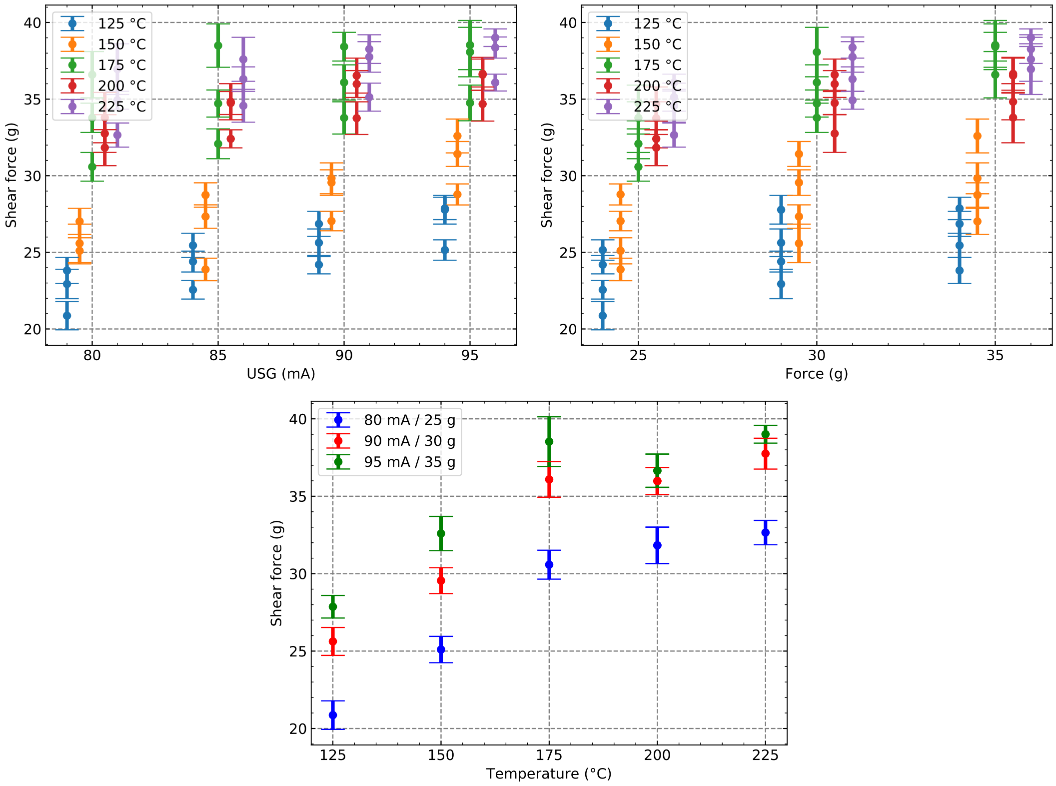

Figure 4.10: Results of shear tests on a CiS sensor. Top left: Shear forces versus USG for temperatures between 125 °C to 225 °C. The data points for each of the four USG values are spaced horizontally for better visibility. Each T–USG combination shows data for bond forces of 25, 30, and 35 g. Error bars show the standard deviation over 20 sheared bumps. Top right: Same data plotted versus bond force. The data points for all three bond forces are spaced horizontally for better visibility. Bottom: Shear force versus temperature for three bond parameter sets.

4.5.2 Solder paste printing and reflow

The solder paste is applied to the microcable in a screen-printing process. Screen-printing is performed on high-precision laser-cut stencils on an EKRA E5 STS screen printer. In the printing process, the substrate—in our case the microcable—is fixed by vacuum on a movable platform. A camera system aligns the substrate to the stencil before the platform brings them

Table 4.3: Gold bump parameters used for the STS sensors and ASICs. Sizes are given in mil (1 mil = 25.4 µm).

Wire ∅ (mil)	FAB[a] (mil)	USG[b] (mA)	Force (g)	Time (ms)	T (°C)	SD[b] (mil)	BH[c] (mil)	SH[d] (mil)
0.9	1.9	90	30	8	175	1.3	0.8	0.8

[a] Free Air Ball; [b] Ultrasonic Current; [c] Smooth Distance; [d] Bond Height; [e] Separation Height

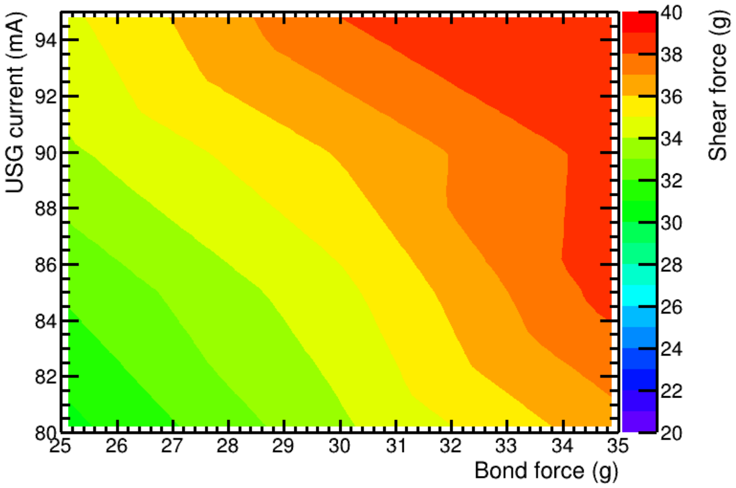

Figure 4.11: Same data as in Figure 4.10 on the previous page, shown as a 2D contour plot of the parameter phase space for a bond temperature of 175 °C.

into contact. Next, the solder paste is applied with a squeegee. Important process parameters are the squeegee speed and pressure as well as the stencil lift-off speed. The vacuum which fixates the microcable had to be turned off before applying the solder paste. Otherwise, the solder paste leaked in between the bond pads.

The majority of solder paste printing investigations have been performed with Heraeus $Sn_{96.5}Ag_{3.0}Cu_{0.5}$ (SAC305) type 7 and type 8 solder pastes. Lead-free solder pastes and their printing performance have been investigated thoroughly in the last decade [106, 107]. Solder paste typically consists of flux and solder in a volume ratio of 50/50 which results in a significant volume loss during reflow.

Fine-grain solder pastes, such as type 7 or higher, have a large surface-to-volume ratio and therefore oxidize quickly. In general, the time between air exposure and insertion into the reflow oven should be minimized. During reflow, the flux evaporation, processing gases, a high amount of oxidation, and humid substrates can lead to solder splashing as well as trapped gas inside the solder, so-called voids. There are various types of voids. Depending on their size and even more so on their location, these voids can substantially reduce the reliability of the solder joint [108]. Solder splashing in turn can lead to short circuits [109]. As all these defects are strongly dependent on the reflow atmosphere, it has been studied intensively. All experiments have been performed in an ATV Technologie GmbH SRO–700 table top IR vacuum reflow oven.

Figure 4.12 shows a typical reflow profile. In the beginning, the chamber is flooded twice with N_2 with intermittent vacuum to reduce the oxygen content in the reflow oven below 10 ppm. Next, the temperature ramps up to 245 °C, which is held for 4 minutes. Finally, the chamber is cooled as fast as possible because previous reflow investigations at KIT have shown strong

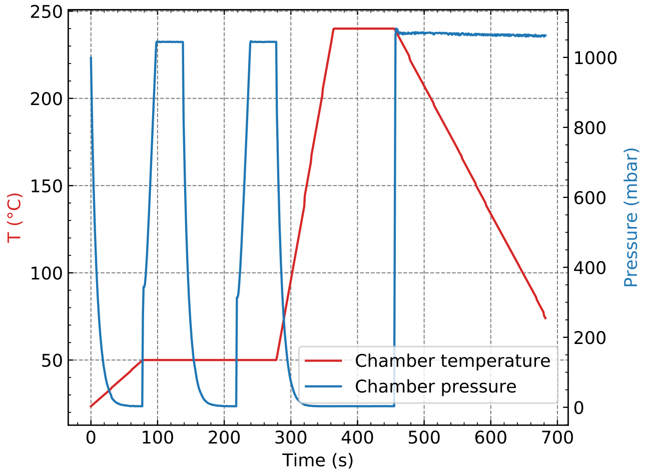

Figure 4.12: Typical reflow profile used for the solder paste reflow on the microcable.

voiding related to a slow cool-down process [104]. Fast cooling also decreases process time. Four distinctly different process atmospheres have been tested:

a) without flushing of the chamber, no processing gases,
b) actively sucking vacuum after flushing, depicted in Figure 4.12,
c) not actively sucking vacuum after the second flushing step,
d) 3 L min^{-1} flow of a N_2/HCOOH gas mixture (additional plateau at 160 °C held for 120 s), second plateau 120 s at 245 °C.

Cross sections of the microcables after reflow are shown in Figure 4.13. Figure 4.13a clearly shows the need for chamber flushing to remove residual oxygen. Simply staying under vacuum does not lead to a proper reflow (Figure 4.13b), either. Staying under N_2 (Figure 4.13c), as well as introducing formic acid (Figure 4.13d), lead to a complete reflow of the solder paste. While both results are acceptable, the formic acid process on average has lead to more voids and some small free solder balls, as shown in Figure 4.13d. Moreover, process c) does not require an additional processing gas such as formic acid, and thus it is the favored process for the solder paste reflow. Figure 4.14 underlines the high level of solder depot uniformity and quality that can be achieved with process c).

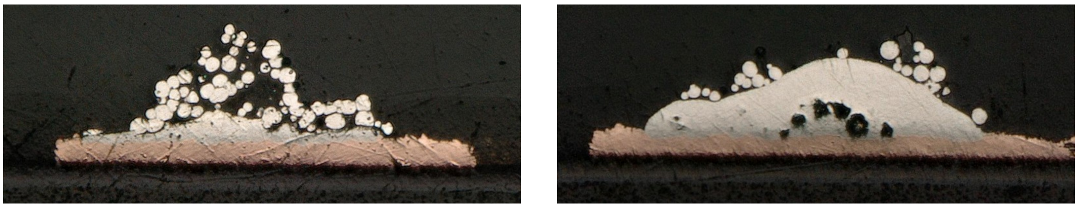

(a) Partial reflow in the bottom region.

(b) More advanced, yet still incomplete reflow. Some voids are present.

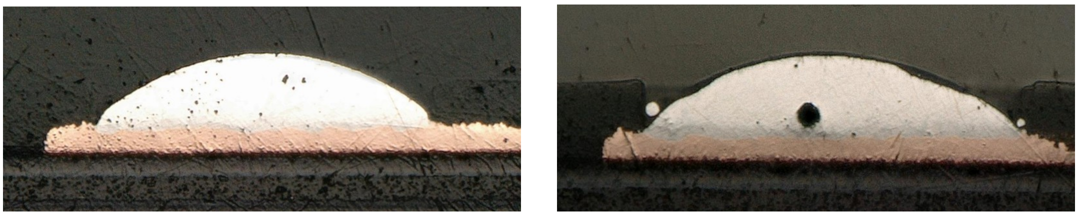

(c) Full reflow without any major voids.

(d) Full reflow with two free solder balls and a void present.

Figure 4.13: Cross sections of solder paste type 7 on the copper microcable after the reflow process. Four different process atmospheres have been tested. They are described in the text.

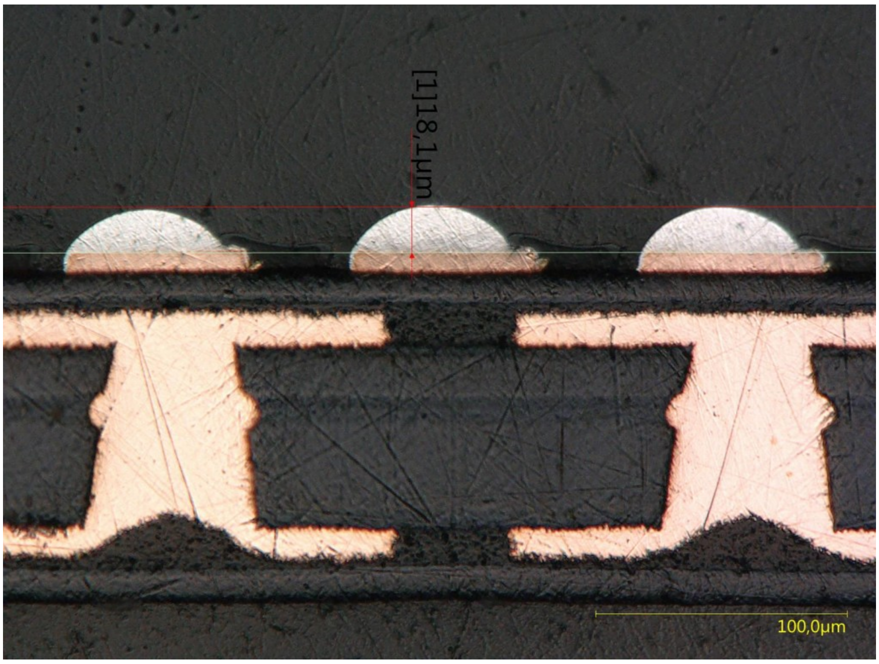

Figure 4.14: Homogeneous solder depots after reflow.

Low-temperature fine-grain solder paste In the assembly of eight chipcables onto one sensor side, the gaps between the microcables are as small as 20 µm. The thermal expansion of the microcable for a peak temperature of 230 °C is close to 20 µm. Combined with the manufacturing tolerances and even more so tolerances in laser cutting for microcable separation, it proved impossible to align the microcables without overlap. One possible remedy is to minimize the bonding temperature.

Therefore, we investigated several fine-grain solder pastes with lower liquidus temperatures T_l. These include $Sn_{63}Pb_{37}$ (T_l = 183 °C), $Sn_{42}Bi_{58}$ (T_l = 138 °C), and $Sn_{42}Bi_{57.6}Ag_{0.4}$ (T_l =131 °C). Changing the solder paste type and alloy typically requires the adaptation of most of the screen-printing and reflow parameters. Even with optimal parameters, the results for different pastes will differ and the paste's suitability must be determined individually. As an additional remedy to reduce the effects of the microcable expansion, the microcable bond pitch was reduced by 0.5 µm, reducing the overall microcable width by 31.5 µm. Eventually, it was found that, with these microcables, even the Heraeus SAC305 solder paste could be successfully used in the chipcable–sensor interconnection.

4.5.3 ASIC-to-microcable interconnection

Die and microcable, prepared for bonding, are shown in Figure 4.15. After preparation with gold bumps and solder paste, both components are connected in a flip chip thermocompression bonding process with the help of a Finetech Fineplacer femto flip chip machine (femto). Initially, it was foreseen to have a tacking step at around 140 °C under the femto followed by a dedicated reflow process in the reflow oven. This process was thoroughly investigated with varying tacking and reflow parameters. However, none of them led to a satisfying result. The dies disconnected easily. The low weight of the chip might cause it to float on top of the liquid solder during reflow resulting in a weak interconnection after solidification. Attempts to weigh down the chip during reflow proved unsuccessful.

It was then attempted to have a full reflow under the femto machine. A typical femto bonding and reflow profile with a peak temperature of 260 °C and a low bond force of 5 N during ramp-up and 1 N during the liquid phase is shown in Figure 4.16. This process requires an inert gas atmosphere to prevent oxidation of the solder surface. The femto can provide N_2 as well as HCOOH gas to the bond area. Unfortunately, the dedicated motorized gas chamber was not available during the time of this work. Still, N_2 gas could be used with a custom-built gas chamber. The full reflow process under the femto resulted in shear forces below 400 g, which corresponds to less than 3 g/bump, as shown in Figure 4.17 on page 58. Possible reasons for the low interconnection strength might be the lack of HCOOH gas, improper removal of residual oxygen, and non-optimal bond parameters.

In a third and novel approach, a full reflow is avoided. Under clean room atmosphere, the solder is heated to around the liquidus temperature to become soft and promote intermetallic formation. The Au stud is then pressed into the solder with a higher force to penetrate it

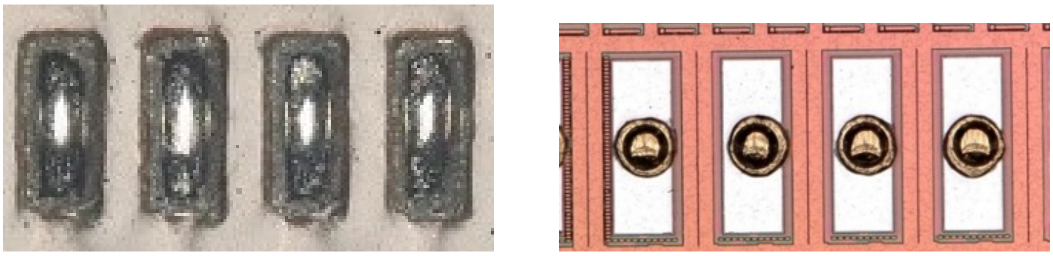

Figure 4.15: Four bond pads of both the copper microcable (left) and the readout ASIC (right) after preparation for the thermocompression flip chip bonding.

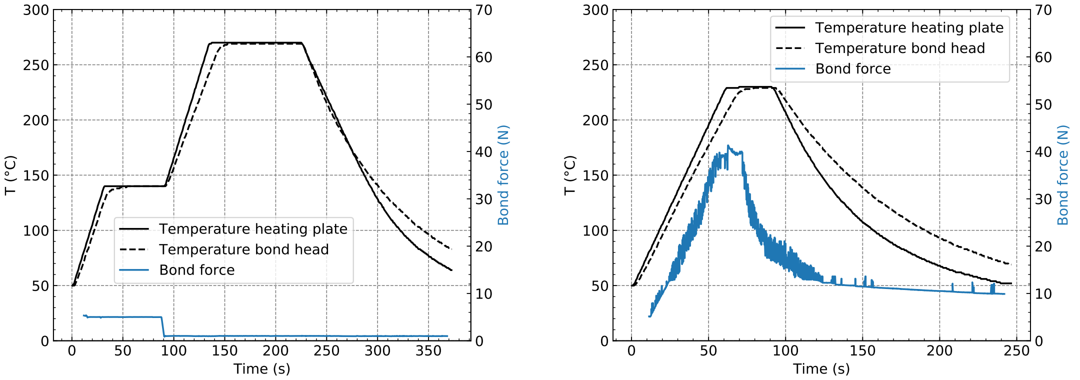

Figure 4.16: Bonding profile for the traditional reflow performed under formic acid atmosphere (left) and for the non-reflow tacking performed under ambient atmosphere (right).

deeply and guarantee a large interconnection area. Optimization of the bonding parameters led to a bond force of 40 N and a bonding temperature of 230 °C. The corresponding thermocompression bonding profile is shown in Figure 4.16. Figure 4.17 shows the achieved shear strength for the improved non-reflow bonding process. It amounts to 1800 g which corresponds to 14 g/bump, a significant improvement compared to the initial reflow process. High mechanical shear forces have been obtained for varying bonding parameters between 10 N to 60 N and 200 °C to 250 °C. A cross section of the chipcable structure bonded with a bond force of 40 N and a bonding temperature of 230 °C under ambient atmosphere is shown in Figure 4.18. It clearly shows the excellent wetting of the gold stud with solder which explains the high mechanical strength of the interconnection. The shape of the solder hints to the incomplete reflow during bonding. X-ray imaging enables non-destructive testing of the alignment after bonding. Figure 4.19 on page 59 shows an X-ray image of the interconnection area between die and microcable with the gold studs located in the center of the bond pads.

4.5.4 Underfill application

The application of underfill between the die and the microcable is a non-trivial task. Depending on the bond force and solder volume, the gap between microcable and die can be as low as

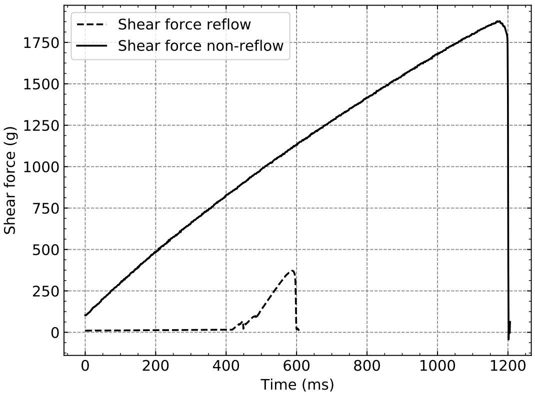

Figure 4.17: Shear test results for the traditional reflow and the improved non-reflow process.

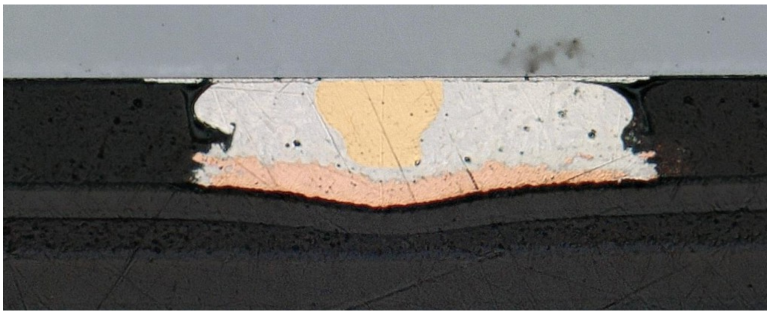

Figure 4.18: Cross section of the STS-XYTER ASIC (top) bonded onto the copper microcable (bottom). The gold ball is covered in solder entirely. The microcable is slightly compressed due to the applied bond force .

20 µm. The individual interconnections act as obstructions for the underfill material. Air inclusions on the sensor-side interconnection should be avoided as they could provide a path for sparking between the microcable and the sensor due to the potential difference of more than 250 V by the end of detector lifetime.

Systematic parametric studies of capillary flow in underfill have shown that capillary flow on solder stop—which is present on the microcable in the bond area—is much lower than on a silicon die [110], while obstructions have a much lower influence on capillary flow than temperature, type of material, and surface morphology.

We performed underfill application studies with Polytec EP601-LV underfill glue. Polytec EP601-LV is a transparent, two-component, optically clear epoxy, ideal for fine-cavity filling due to its low viscosity of 240 mPa s. Figure 4.20 shows a readout chip and a microcable after disconnection where Polytec EP601-LV had been applied and cured beforehand. The underfill covered the whole interconnection area without any visible air inclusions. Electrical breakdown behavior of the underfill was tested with an HV generator and considered appropriate for the STS requirements.

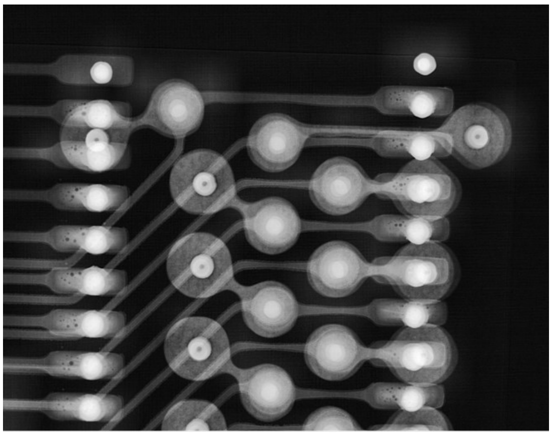

Figure 4.19: X-ray image of the interconnection area between die and microcable. The gold studs (bright spots) are centered in the bond pads.

Figure 4.20: Readout chip (left) and copper microcable (right) after disconnection after the underfill had cured completely. The direction of flow is top to bottom in both images. The material reached the opposite side of the interconnection area without air inclusions.

Radiation hardness tests have been conducted for Polytec EP601-LV on plexiglass substrates with a roughened surface. Aluminium bond wire with a 22 µm diameter was placed as a spacer to achieve a uniform underfill thickness comparable to the gap in the die-microcable interconnection. The interconnection area was 12 mm × 12 mm. The samples have been weighed down during curing at RT for more than 24 h. The setup is shown in Figure 4.21. Six samples each have been prepared for pull tests before and after irradiation at the TRIGA reactor at the Institute for Nuclear Chemistry in Mainz, Germany. The samples have been exposed for 400 s to a mixed field of fast and thermal neutrons with an equivalent 1 MeV neutron flux of $5.15 \times 10^{11}\,\mathrm{cm^{-2}\,s^{-1}}$ resulting in a total fluence of $2 \times 10^{14}\,\mathrm{cm^{-2}}$ which corresponds to the double maximum lifetime fluence of the STS. The results of the pull tests after irradiation are summarized in Table 4.4. Unfortunately, due to technical difficulties, the non-irradiated samples could not be tested. While the relative measurement is missing, the high absolute value of 362.1 ± 22.7 N for the irradiated samples shows that the glue is still mechanically functional after irradiation.

4.5.5 Chipcable-to-sensor interconnection

The chipcable-to-sensor interconnection is the most challenging part of the module assembly. The sensor is fixed in position and eight chipcables are placed one by one on the outer bond

Figure 4.21: Sample preparation for underfill radiation hardness tests.

Table 4.4: Pull test results for plexiglass substrates glued with Polytec EP601-LV given as the average and standard deviation over six samples. Units are in N.

Before irradiation	After irradiation
–	362.1 ± 22.7

row on the n-side. After strengthening the connection with underfill, the whole structure is flipped and eight further microcables are bonded to the inner bond row on the n-side. In order to be able to handle the long and flexible chipcables while simultaneously achieving a great alignment accuracy, a fully customized bonder machine has been developed during this work. It is described in the chapter 5.

4.6 Summary

A low-mass copper-PI flexible microcable with 128 transmission lines and a bond pitch of 116 µm has been designed, developed, produced, and characterized. A sophisticated double-layer design was possible due to the high levels of industry expertise in Cu-PI flex technology. Still, the cable is at the edge of modern fabrication technology, leading to inconsistencies in quality, reduced yield, and rather high cost. Offsets of the solder stop of up to 12 µm appeared in multiple batches due to difficulties in mask alignment. Laser cutting the individual cables from a sheet of eight requires finely tuned parameters to avoid damaging the pads in closest proximity to the cable edge. Therefore, laser cutting had to be outsourced to a dedicated company. A slight long-axis asymmetry in the initial microcable design resulted in a significant microcable twist. We found that the increased stiffness of the copper microcable compared to the aluminium microcables complicates module assembly.

With a stray capacitance of 0.38 $\mathrm{pF\,cm^{-1}}$, the microcable compares well to the primary aluminium cable (0.35 $\mathrm{pF\,cm^{-1}}$). Due to the short radiation length of copper, the relative radiation length of $X/X_0 = 0.05\,\%$ is higher than that of the aluminium cable ($X/X_0 = 0.03\,\%$) but still about an order of magnitude below the sensor contribution ($X/X_0 = 0.32\,\%$).

Based on the copper microcable, a novel high-density interconnection technology has been developed. The individual process steps have been established and optimized. These include the gold stud bumping, solder paste printing, solder paste reflow, die-to-microcable flip chip bonding, underfill application, and the overall handling of the module and its components. The effects of the thermal mismatch between the microcable and die have been minimized by downscaling the microcable pitch and reducing the bonding temperature with low-temperature solder pastes. All in all, the gold stud–solder bump bonding interconnection technology offers good automation capabilities while placing high demands on the precision solder printing and the planarity between microcable and die. Due to the increased material budget of the copper microcable and low yields for long cables, the copper technology is an attractive backup solution for the outermost modules on the STS ladders, which require shorter microcables.

5 Design and Construction of a Custom Bonding Machine

During bonding of the chipcables to the sensors, the sensor must remain stable on the bond table while the chipcables are picked up by the bond head one by one. At first, the goal was to utilize the commercial pick-and-placer machines available at IPE. However, extensive experimentation including the development of custom bond head adapters and vacuum trays did not lead to a satisfying performance. The overarching issue is the fact that these commercial machines are designed to handle small and rigid dies. Loading the bond heads with the long, flexible microcables results in insufficient vacuum adhesion, unstable alignment, and spatial restrictions in the interior of the machines.

Hence, a fully customized bonding machine was developed during this work [111]. Its main purpose is the realization of the interconnection between the chipcable and the sensor. Additionally, the machine can be programmed to perform the ASIC-to-microcable bonding as well as the underfill application. In order to get a better understanding of the following sections, Figure 5.1 shows a single-sided assembly of eight copper chipcables on a 6.2 cm × 6.2 cm sensor next to a schematic drawing indicating the important geometrical parameters for assembly in a side and top view.

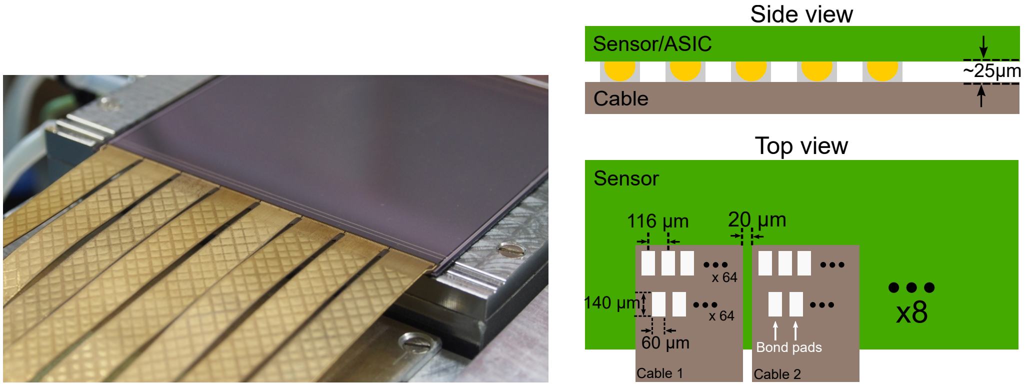

Figure 5.1: Full single-sided assembly of a 6.2 cm × 6.2 cm sensor and eight copper microcables (left). Side and top view drawings showing the dimensions that are important for module assembly (right).

5.1 Requirements

A wide variety of requirements have to be satisfied by the bonder machine. The most important ones are listed below.

Alignment accuracy There is only a small gap of 20 µm in x-direction between the individual microcables on the sensor which places an upper bound on alignment accuracy of 10 µm. Furthermore, the microcables are produced in sheets of eight cables which have to be separated with a laser. The tolerance of this laser cutting process currently is ~5 µm. Therefore, an alignment accuracy of $\Delta_x = 5\,\mu\text{m}$ in the x-direction is required. The accuracy demands in y-direction are less strict. The microcable bond pad size is 60 µm x 140 µm and the gold stud diameter is 55 µm. Demanding that the gold stud should be completely inside the bond pad, the maximum allowed error in y-direction is $\Delta_{y,max} = \frac{140-55}{2}\mu\text{m} = 42.5\,\mu\text{m}$. Any rotational deviation mainly adds to Δ_y, not Δ_x. With 64 pads per row and a pad pitch of 116 µm, the error in y-direction on the outermost pads introduced by a rotational error is Δ_α is $\Delta_{y,rot} = 64/2 \cdot 116\,\mu\text{m} \cdot \tan \Delta_\alpha$. Assuming a translational offset $\Delta_y = 5\,\mu\text{m}$, the maximum allowed error introduced by rotation is $\Delta_\alpha = 10\,\text{mrad}$ or 0.58°.

Thermal resistance and thermal stability During the bonding process, temperatures of up to 230 °C are applied to the bond head and sensor plate. The maximum working temperature of the z-stage is 50 °C, as given by the manufacturer. Therefore, a good thermal insulation between the sensor plate and the motorized stages is required. Thermal fluctuations will lead to differences in thermal expansion between the microcable and sensor and therefore to inaccuracies in alignment. The thermal stability of the system should be better than 2 °C.

Bond force The bonder machine must be able to provide a bond force of at least 40 N [99], equating to roughly 30 g per gold stud. Additionally, the bond force variability between individual assemblies should be small.

Planarity There are 64 bond pads with a pitch of 116 µm along the width of the microcable. If we allow a maximum height difference of 10 µm across all 64 channels, the error in planarity between cable and sensor must be smaller than 0.08°. In any case, non-planarity will always lead to a heterogeneous bond force distribution.

5.2 Bonding machine setup and critical components

With the aforementioned requirements in mind, the bonder machine has been planned, designed, and constructed. The machine is shown in Figure 5.2 on page 66 with its key components labeled. All functional components and the aluminium profile are mounted onto a

1 m^2 steel base in a height of 100 cm to provide a convenient working height. The steel base is mounted onto the lower frame via four shock absorbers to reduce vibrations. The essential components of the bonder machine are:

1 & 2 **X-axis/Y-axis**: Two OWIS® LIMES 150 linear stages provide precise positioning in the xy-plane. Their unidirectional repeatability is better than 1 µm while the microstep resolution is $\mathcal{O}(1\,\mathrm{nm})$. The y-stage is mounted onto the base plate; the x-axis is mounted onto the y-axis with a 90° angle. All motors are controlled with OWIS PS–10 control units.

3 **Z-axis**: Movement in the vertical z-direction is realized with the OWIS HTM 100 z-stage with a repeatability of better than 10 µm. It is mounted directly onto the x-stage. Currently, the step motor version is installed which can be upgraded to a servo motor with automated bond force control, if necessary.

4 **Φ-axis**: Parallel alignment between the microcable and sensor is achieved with the OWIS DMT 100 rotary stage with a repeatability of better than 0.01°. It is mounted directly onto the z-stage.

5 & 6 **Top and bottom camera**: A dual-camera system consisting of a top (facing downwards) and bottom (facing upwards) camera enables sensor detection from the top and microcable detection from the bottom to ensure precise alignment. Both camera setups comprise a Basler acA1300-200µm 1/2" camera and a Lensation TCST-40-40C lens. The lenses have an object side resolution of 4.8 µm and a depth-of-field of 143 µm.

7 **Bond head** The heatable bond head picks up the microcables from the vacuum tray. Heating is done with a heating cartridge. Temperature regulation is provided by a temperature sensor and a JUMO Quantrol LC100 controller. A precision bond tool from SPT sucks the microcable in the bond area. Microcables of varying lengths can be secured to the bond head by exchangeable vacuum tools with varying lengths. The bond head is thermally isolated from the rest of the machine. Planarity between the bond head and sensor plate is achieved with niveling screws.

8 **Sensor plate**: The silicon sensors are secured by vacuum on the heatable sensor plates. The base of the sensor plate has three heating zones which can be switched on and off for the different sensor sizes. The top plate is replaceable to accommodate the different sensor sizes. Alternatively, precision limit stops can be installed. Heating is done with heating cartridges regulated by a temperature sensor and a JUMO Quantrol LC100 controller. The sensor is thermally isolated from the motors. The sensor plate is extended to the backside to host the bonded microcables.

9 **Chipcable tray**: Before bonding, up to eight chipcables are placed on the designated vacuum tray next to the sensor. Each chipcable has an independent vacuum supply.

5.3 Thermal insulation optimization

In a first iteration, a planar plate of Torlon (polyamide-imide material) with a thickness of 6 mm and a thermal conductivity $\lambda = 0.28\,\mathrm{W\,m^{-1}\,K^{-1}}$ was installed as a thermal insulation between both the sensor plate and the motors and the bond head and the aluminium frame.

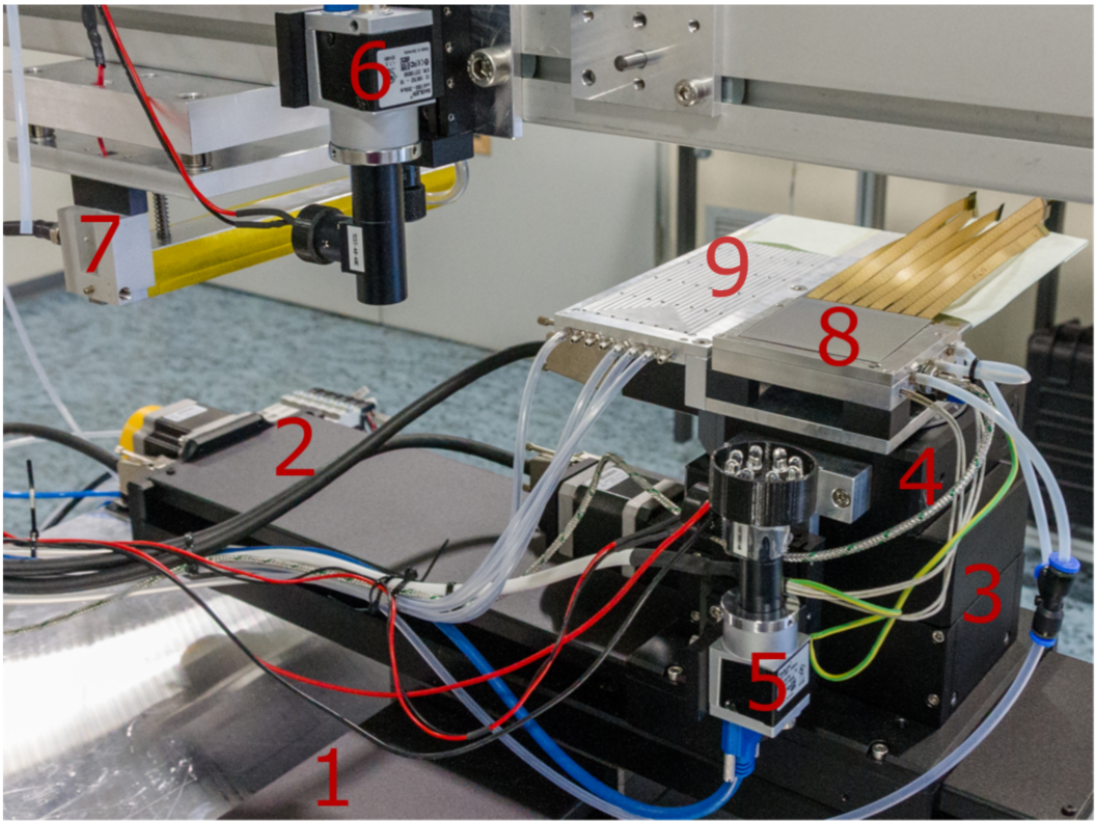

Figure 5.2: The custom bonding machine developed at IPE for CBM–STS module production. The labeled components are described in the text.

However, heat camera measurements revealed excessive heating of the motorized stages. Upon removal, the Torlon plate showed burn marks and severe bending. To improve the mechanical property retention at high temperatures, Duratron CU60 PBI was chosen as the new thermal insulation material. It has a thermal conductivity of $\lambda = 0.4\,\mathrm{W\,m^{-1}\,K^{-1}}$ and is delivered in sheets of 12.5 mm thickness.

Thermal FE simulations have been performed for several geometries. The final geometry and the respective simulation results for different heating powers are shown in Figure 5.3. A considerable minimization of contact area was necessary to achieve the required thermal insulation in order to keep the z-stage below 50 °C. Based on the simulation results, the insulation has been manufactured in house and is now in operation for more than two years. Thermal insulation is sufficient up to at least 230 °C and no signs of deformation are visible after hundreds of temperature cycles and bonding operations.

5.4 Bonding procedure and working principle

After preparation of the components, the gold-bumped sensor is placed on the sensor plate while eight chipcables are put on the vacuum tray. The bond head and sensor plate are heated to the respective bonding temperatures of 180 °C and 150 °C. The bond head temperature is higher to make sure the solder is adequately soft while the lower sensor temperature increases the stability of the already bonded cables. The individual process steps for the sensor-side assembly are described in a flow chart together with accompanying diagrams for better visualization in Figure 5.4.

Before the actual assembly procedure can begin, a camera calibration needs to be performed. Its motivation and realization are described in detail in section 5.5. After successful calibration, the following steps are repeated for all eight chipcables per side: First, the chipcable is picked up by the bond head. A custom-designed vacuum structure keeps the long cable in place. Next, the cable is detected with the bottom camera which moves together with the motor

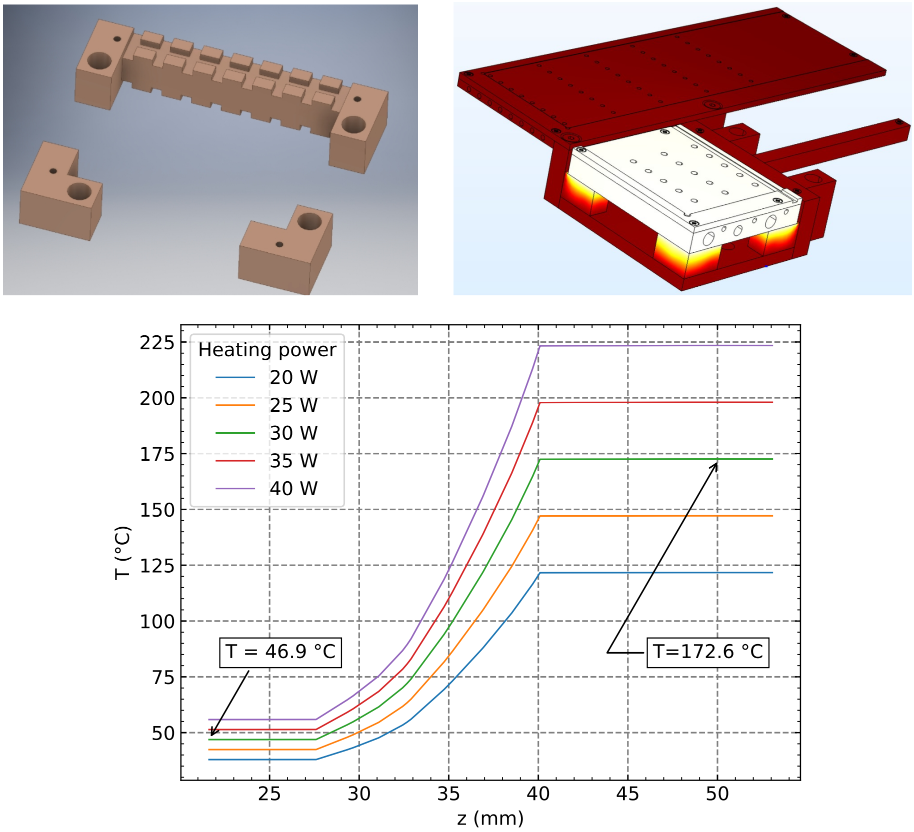

Figure 5.3: Final geometry of the thermal insulation between the sensor plate and motors (top left). The thermal simulation setup (top right). Thermal simulation results showing the temperature drop across the insulation material for various heating powers (bottom). The curve where the temperature on the motor falls below 50 °C is indicated.

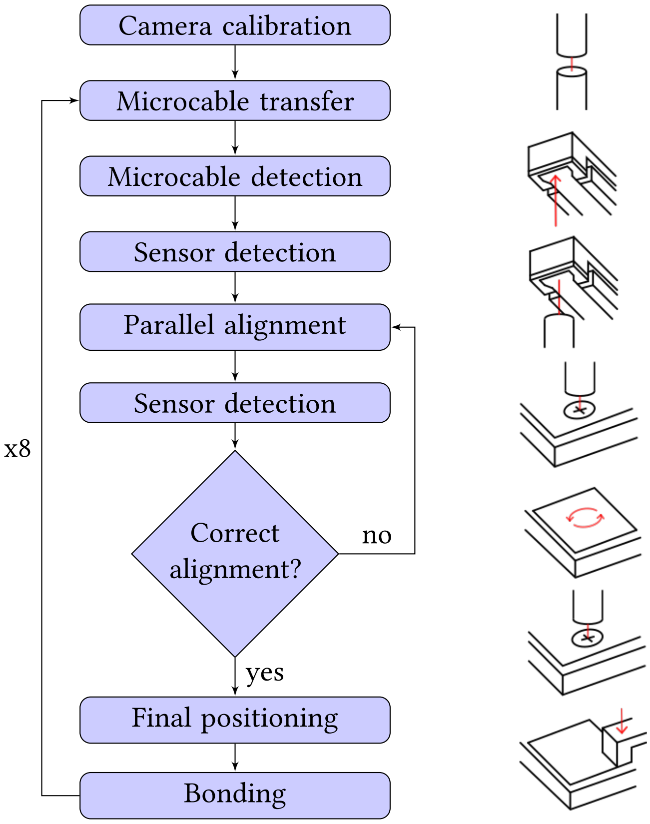

Figure 5.4: Flow chart of the chipcable–sensor bonding accompanied by sketches of the corresponding process steps.

stages. The motor positions and the positions of the cable fiducials inside the image are stored. Then, the stages move such that the top camera is able to detect the sensor via two fiducials in the upper left and upper right sensor corner. The rotational stage rotates the sensor parallel to the cable and the fiducials are detected again. Thanks to the second detection after rotation, precise knowledge of the distances between the eight assembly positions on the sensor and the rotation axis is not required.

Now, the stages align the respective bonding position on the sensor with the chipcable. The z-stage moves the sensor up into contact with the chipcable where it resides for a typical bonding time of 60 s. After successful bonding, the assembly of the next cable begins. After one side of the sensor has been fully bonded, underfill glue can be dispensed automatically. After the glue has cured, the full structure is carefully flipped to assemble the opposite side with eight additional chipcables.

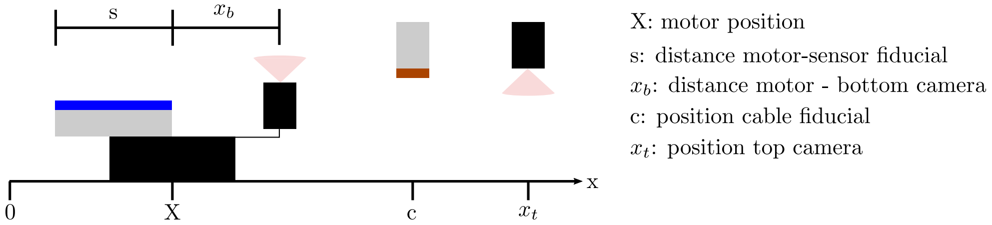

Figure 5.5: 1D sketch showing the essential coordinates required to determine the bond position.

5.5 Camera calibration

In order to achieve accurate alignment between the microcable and sensor, the top and bottom camera have to be calibrated. Figure 5.5 displays a one-dimensional sketch illustrating the relevant coordinates needed to calculate the assembly position. The motor position x can be manipulated and read back by the software. The positions of the sensor s and the microcable c can vary in between bonding cycles and must be determined. Ideally, the positions x_t and x_b of the top and bottom camera remain constant in between assemblies. However, vibrations in the setup or mechanical stress introduced by touching the camera or the camera mounts could lead to minor camera movement. The sensor plate and the bottom camera are rigidly connected to the motor, hence their positions x_s are x_b are given relative to the motor position x.

Let x_0 be the motor position where the fiducials of the microcable and sensor coincide. To find correct bonding alignment one must calculate the distance from the fiducials to the assembly positions, where the bond pads coincide. The sought motor position is

$$x_0 = s + c\,. \tag{5.1}$$

To find s and c, the fiducials of the sensor and microcable are detected. The respective motor positions are x_s and x_c. Now, s, c and x_0 are

$$\begin{aligned} s &= x_s - x_t\,, && (5.2)\\ c &= x_c + x_b\,, && (5.3)\\ \hookrightarrow x_0 &= x_s + x_c + x_b - x_t\,. && (5.4) \end{aligned}$$

Theoretically, the correct bond position can be identified for each bonding cycle by determining x_b and x_t. However, measuring them is complicated. Fortunately, it can be avoided by performing a camera calibration procedure—finding the motor position x_{cc} where both cameras are coincident.

$$\begin{aligned} x_{cc} &= x_t - x_b\,, && (5.5)\\ \hookrightarrow x_0 &= x_s + x_c - x_{cc}\,. && (5.6) \end{aligned}$$

It is not sufficient to perform the calibration once. Not only because the cameras can move but also because the zero position of the setup changes slightly each time the motors are

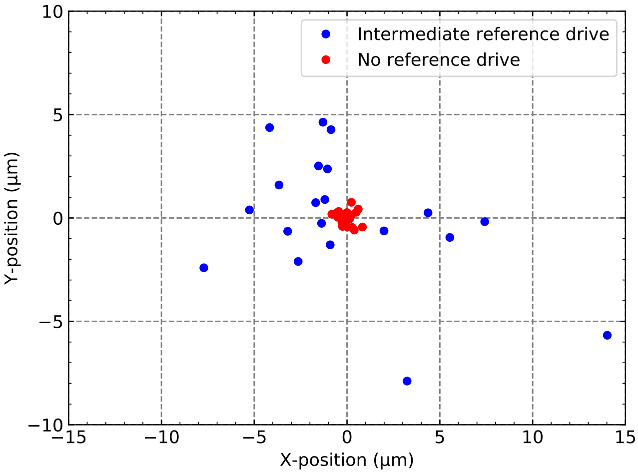

Figure 5.6: Detected motor positions for repeatedly moving into the same position with and without intermediate reference drives.

referenced. This is shown in the graph in Figure 5.6. It shows the detected motor positions for driving 20 times into the same position with and without an intermediate reference drive of the motor axes. In practice, the calibration is conducted by detecting a precise laser-cut pattern with both coinciding cameras, as depicted in the sketch on the left side of Figure 5.7. A custom pattern holder was developed which is installed on the aluminium profile, shown on the right side of Figure 5.7. It allows position manipulation in three dimensions for optimum positioning of the calibration pattern. The pattern itself is realized by precision laser cutting in thin sheet metal.

To perform the calibration, first the lower camera is moved roughly underneath the upper camera. Next, the upper and lower camera detect the calibration pattern and store its center coordinates. The pixel positions are converted into mm. The motor now moves to counterbalance the offset between the cameras. These steps are repeated iteratively until the desired accuracy is achieved. The tolerance must be chosen small but not too small to avoid an endless loop. Finally, the motor position after calibration is stored together with the image coordinates of the calibration pattern.

5.6 Bond position calculation

After the sensor has been rotated parallel to the microcable and has been detected again, the final bond position needs to be calculated. A complication arises from the fact that the sensor coordinate system typically is rotated with respect to the motor axes coordinate system. Hence, the known distances from the sensor fiducials to the bond positions must be converted into the motor coordinate system. There are several possibilities to do so, using either of

Figure 5.7: Sketch of the camera calibration setup (left). Both the top and bottom camera detect the calibration pattern simultaneously. The mounting device developed for inserting the calibration pattern in between the cameras is shown on the right.

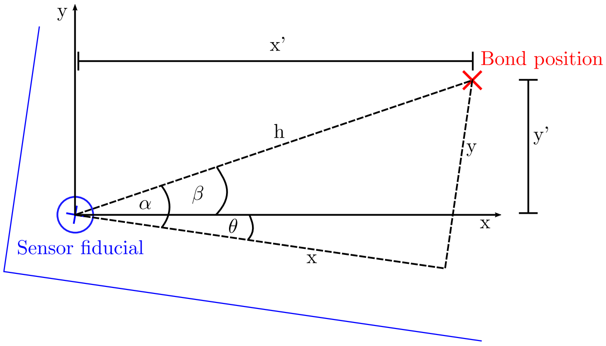

Figure 5.8: 2D sketch illustrating the relevant geometrical parameters in determining the bond positions.

the two fiducials or the midpoint between them. We opted to use the fiducials closest to the respective bond position.

Figure 5.8 illustrates the relevant geometrical parameters. The parameters x and y are known from the sensor design whereas x' and y' are the sought-after coordinates in the motor axes system. Let's assume that the sensor is rotated by the angle θ with respect to the motor axes system. The following relations hold

$$h = \sqrt{x^2 + y^2}\,, \tag{5.7}$$

$$\alpha = \arctan\frac{y}{x}\,, \tag{5.8}$$

$$\beta = \alpha - \theta\,, \tag{5.9}$$

$$x' = \cos\beta \cdot h\,, \qquad y' = \sin\beta \cdot h\,, \tag{5.10}$$

$$\hookrightarrow x' = \cos(\arctan\frac{y}{x} - \theta) \cdot \sqrt{x^2 + y^2}\,, \qquad y' = \sin(\arctan\frac{y}{x} - \theta) \cdot \sqrt{x^2 + y^2}\,. \tag{5.11}$$

The angle θ can be measured with the camera system. Knowing x' and y', the final positioning can be performed. Here, it is important to consider the bond head and sensor plate temperatures during bonding. The temperature differences of the bond head and sensor plate with respect to RT are ΔT_{bh} and ΔT_s, respectively. The CTE of the microcable is α_c, the CTE of the sensor is α_s. Finally, eq. (5.6) on page 69 is modified into

$$x_0 - x_s = x_c - x_{cc} + d_y \sin\theta \cdot \alpha_c \Delta T_{bh} + x'\alpha_s \Delta T_s\,, \tag{5.12}$$

$$y_0 - y_s = y_c - y_{cc} + d_y \cos\theta \cdot \alpha_c \Delta T_{bh} + y'\alpha_s \Delta T_s\,. \tag{5.13}$$

5.7 Interplay between cameras and motors

To determine the conversion factor C between the pixels in the camera image and the actual length scale in µm, an object with a well-known geometry such as the sensor or the ASIC is measured with the cameras. The determined conversion factor for our setup is 1.2049 µm/pixel with a first deviation in the sixth decimal. As the image size is $\mathcal{O}(1000\,\text{pixels})$, the maximum conversion error over the full image size is of the order $\mathcal{O}(10\,\text{nm})$ and therefore negligible.

As mentioned in section 5.5 on page 69, the camera calibration is necessary to find the motor position where both cameras are coincident. In order to determine the interplay between the cameras and the motor axes, a series of measurements has been performed. First, the camera calibration is performed with the calibration pattern in the image center. Let us refer to the image coordinates of the pattern in this position as the calibration position. Next, the calibration is repeated with the calibration pattern in the corners of the image, namely the upper right and lower left corner. In a perfect setup with neither rotation nor tilt between the cameras, the pattern should be detected at exactly the same position with both cameras. The distances between the pattern and the initial calibration position are called $d_{x,cp}$, $d_{y,cp}$. The difference in the image coordinates of the detected pattern between the top and bottom camera are called $d_{x,tb}$, $d_{y,tb}$. The ratio d_{tb}/d_{cp} yields the deviation in dependence of the distance to the center calibration position.

The results of these measurements are presented in Table 5.1 for two different setups. In the initial setup, the cameras were mounted to the frame with ordinary angled aluminium brackets. In the second setup, the ordinary brackets were replaced by OWIS VT 30–Z precision brackets. With increasing distance from the image center, the deviation between the cameras increases in both setups. However, the installation of the precision brackets significantly improved the accuracy of the system. Still, deviations of a few µm are possible. Therefore, during fiducial detection, the motors are moved such that the image coordinates of the fiducial correspond to the image coordinates of the calibration pattern during camera calibration.

Table 5.1: Measurements for testing the stability of the camera system in two different camera mounting setups. Units are in µm. The meaning of the individual columns is explained in the text.

	Position	$d_{x,cp}$	$d_{y,cp}$	$d_{x,tb}$	$d_{y,tb}$
Initial brackets	Calibration position	0.0	0.0	0.6	0.9
	upper right	50.1	381.4	7.5	13.2
	lower left	100.2	200.8	15.7	20.0
OWIS VT 30−Z brackets	Calibration position	0.0	0.0	0.3	0.8
	upper right	166.6	170.6	2.0	0.1
	lower left	192.7	117.0	3.5	2.0

5.8 Performance evaluation

The final alignment accuracy of the bonding process is determined by various uncertainties. Systematic errors such as the yaw angle and pitch angle of the motors, rotation between bond head and motor axes, rotation between individual motors, or a tilt between the two cameras can be corrected for by the camera calibration procedure and by introducing offsets in the final alignment. The maximum accuracy of the alignment process is determined by statistical uncertainties which are mechanical, thermal and optical in nature. They include the repeatability of the linear stages, the camera resolution together with the pattern recognition capabilities, and the thermal stability of the full system. Five major statistical uncertainties contribute to the bonding process. After performing dedicated tests for all of them, the errors are conservatively estimated to be:

- Repeatability of the linear stages $\sigma_{motor} = 2\,\mu\text{m}$.
- Accuracy of camera calibration $\sigma_{calib} = 1.5\,\mu\text{m}$.
- Accuracy of cable detection $\sigma_{cable} = 2\,\mu\text{m}$.
- Accuracy of sensor detection $\sigma_{sens} = 2\,\mu\text{m}$.
- Thermal fluctuations $\sigma_T = 0.5\,\mu\text{m}$.

The individual uncertainties are not correlated and add in quadrature to $\sigma_{total} = 3.8\,\mu\text{m}$. This value lies well within the specifications of 5 µm.

5.9 Summary

Since the available commercial flip chip bonder machines at IPE are not suitable to establish the chipcable-sensor interconnection, a fully customized bonding machine was developed in hardware and software during this work. While its main purpose is the realization of the chipcable-sensor interconnection, it can be additionally used to perform the ASIC-microcable bonding as well as the underfill application.

Key features include four step motors with sub-micron step resolution, a dual-camera pattern recognition system, a heatable, temperature-controlled bond head and sensor plate, as well as tailor-made mechanical supports for the STS detector modules. The machine can acommodate each of the four sensor sizes employed in the STS.

With the help of thermal FE simulations, an appropriate geometry for the thermal insulation between the sensor plate and the motors, combining adequate thermal insulation and excellent mechanical property retention, was found. In order to achieve precise alignment between the chipcable and sensor, a camera calibration procedure—referencing both cameras to each other—was successfully developed and implemented. The essential figure of merit of the bonder machine is its alignment accuracy. After extensive testing, it is conservatively estimated to be below 4 μm, an excellent result fulfilling the imposed requirements.

The in-house developed bonder machine builds the foundation for the assembly of full-fledged detector modules in the copper technology, which can then be thoroughly tested and characterized in the laboratory as well as in test beam campaigns.

6 Characterization of the STS-XYTER2.1 Readout ASIC

A thorough characterization of the STS-XYTER2.1. readout ASIC is essential to confirm the proper functioning of the chip, both standalone as well as in conjunction with the silicon sensors and interconnects. Amplitude and time calibration is required to assure consistent behavior among ASICs as well as individual readout channels before installation in the STS detector. The calibration protocol for the STS-XYTER2 was developed in [112]. The following sections start by recapping a few issues—like the different behavior of odd and even channels—uncovered in the STS-XYTER2 and subsequent changes implemented in the STS-XYTER2.1. The focus of the chapter lies on the characterization of the STS-XYTER2.1 ASIC with a particular emphasis on the quantitative noise performance of the chip. Other important ASIC characteristics, such as its rate capability, crosstalk, and radiation hardness have not been evaluated during this thesis. The radiation hardness of the STS-XYTER2 was evaluated before in [112]. Rate capability measurements require a different test environment to what is described in this chapter. Data rates are being evaluated in the mini CBM (mCBM) beam campaigns at GSI, where a subsample of the individual detectors of CBM is exposed to the products of a heavy-ion collision. mCBM mimics CBM operation conditions with beam intensities of up to 10^8 heavy ions/s and collision rates of up to 10 MHz. In the 2019-2020 mCBM campaign, the achieved STS data rates were up to 800 MB/s, which corresponds to an average of 6.25 Mhits/ASIC/s (close to the limit of 10 Mhits/ASIC/s in the available FEB8-1 readout). This rate was dominated by delta electrons, whose contribution is very strong in the proximity of the target region and not suppressed by any magnetic field [113]. There, also the channel-to-channel and ASIC-to-ASIC crosstalk can be evaluated on the module level.

6.1 Overview of the changes implemented in the STS-XYTER2.1

The readout ASIC has already been described in section 3.3. Here, the focus lies on the issues detected in the STS-XYTER2, which triggered the development of the revised STS-XYTER2.1 chip. Two major observations have been made in analyzing the noise performance over all channels of the STS-XYTER2. First, a significant difference in noise between odd and even channels. Second, a considerable increase in noise towards the higher channel numbers. The former effect is associated to differences in the CSA biasing scheme between odd and even channels [90]. The latter effect is related to the biasing DACs of the ASIC being physically located on the side of higher channels. A detailed analysis of the STS-XYTER2 ESD protection circuit and its leakage current revealed two effects: The total leakage current contributing

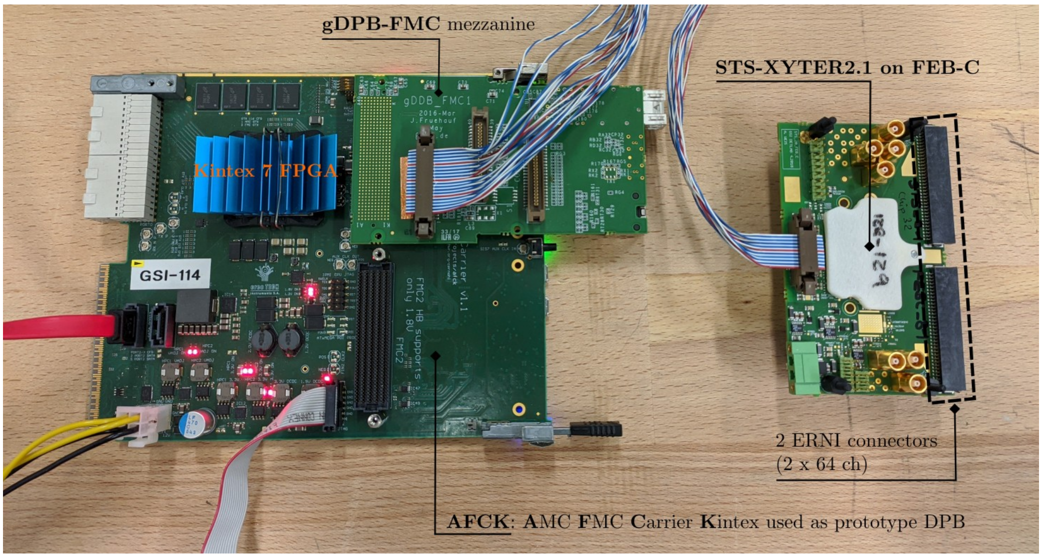

Figure 6.1: Photograph of the prototype readout system used for testing the STS-XYTER2.1 ASIC.

to the noise and the leakage current flowing into the CSA were larger than expected. The leakage current flowing into the CSA affects the use of the fast reset circuit of the CSA and needs to be minimized or compensated [114].

Overall, the main objective of the new design was to lower the output noise level and improve functionality. Several modifications have been implemented in the analog front end, including:

- Improved input transistor biasing scheme to reduce odd-even noise differences.
- Addition of pads for external decoupling on both sides of the chip for both DACs driving the odd/even channel input biasing current source reference node for further reduction of odd-even discrepancies.
- Removal of the ESD protection circuit for lower leakage current–induced noise and proper operation of the fast reset.
- Timing comparator with differential threshold to enable noise evaluation without signal. Implementation of an identical 8-bit DAC as in the previous chip also to the second branch of the comparator input stage.
- Improved resolution of global threshold of the slow path for better control of noise discrimination in the ADC.
- Addition of a 3 pF MOS capacitor in each channel to filter the noisy reference of the PSC.
- Improved radiation resistance regarding SEU and TID effects.

Further details of the chip modifications are described in [114, 115].

6.2 Test environment

Operating and testing the STS-XYTER2.1 ASIC requires a dedicated test system including a prototype readout chain. During this work the STS-XYTER2.1 ASIC was tested with the setup shown in Figure 6.1 on the previous page. Its main components are:

- a FEB-C hosting a single STS-XYTER2.1 ASIC,
- an FPGA-based data processing board (DPB) implementing the communication protocol backend,
- a gDPB-FMC mezzanine card, used for interfacing the FEB-C with the DPB.

The hardware platform for implementing the readout backend is bases on the AFCK board [116], which is the development and prototyping platform for the CBM DPB. The firmware reuses the functionality of the STS protocol-tester [117], designed for standalone protocol tests with the ASIC. The communication with the controller backend is done via the IPBus protocol using a 1 Gbps Ethernet link [118]. The FEB-C is a dedicated front end board for advanced characterization of the STS-XYTER2.1 ASIC. It enables signal extraction before and after the CSA, after the PSC, after the slow and fast shapers, as well as of the internal pulser for the two test channels implemented in the ASIC. The ASIC channels are wire bonded to a fan-out leading into two ERNI connectors with 64 channels each. External sensor boards or capacitor boards can be connected via the ERNI connectors. The FEB-C is also used for building prototype detector modules with a single ASIC per sensor side. This is highly valuable in the development stage, as it allows testing for connectivity between the microcable and ASIC or sensor and the evaluation of the overall noise and signal levels without the need to build complete detector modules.

6.3 Characterization of the STS-XYTER2.1

In a first characterization step, the ASIC analog waveforms are acquired from the output of the CSA, the fast shaper, and the slow shaper. The waveforms are observed and recorded with an oscilloscope (Tektronix 4054) for various ASIC register settings. A non-exhaustive lists of tests includes measuring the CSA bias current, the shaper bias current, shaping times, the feedback resistance, the ADC threshold, and the fast reset of the CSA. For more advanced testing, S-curve scans enable the quantitative analysis of noise performance for variable input capacitances and shaping times. The procedure is explained in detail in section 6.4.1.

6.3.1 Linearity of the internal pulse generator

Like its predecessor chip, the STS-XYTER2.1 ASIC has an internal calibration circuit which makes it possible to inject charge pulses into the analog front end. Automated calibration of all channels enables you to test the pulse processing chain of the chip. The ASICs 128 channels are subdivided into four groups of 32 channels each of which can only be excited

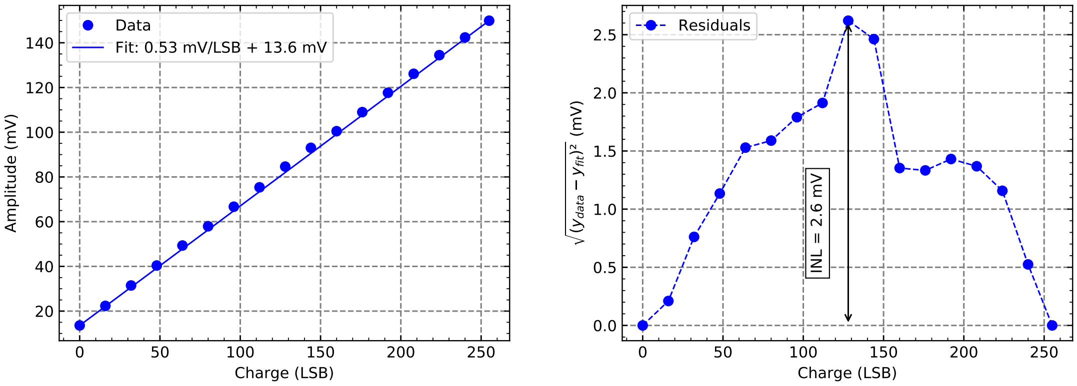

Figure 6.2: Linearity of the internal pulse generator. Left: Recorded amplitudes on the *amp_cal* pad over the full dynamic range of internally injected pulses including a linear fit. Right: Determination of the integral non-linearity of the internal pulser based on the distance of the data points to the linear fit shown in the left panel.

one after the other to reduce saturation effects. An on-chip bistable generator injects charge pulses through a set of capacitors ($C = 100$ fF). Pulse amplitudes of up to 140 mV are feasible, corresponding to a charge of approximately 14 fC. A dedicated pad on the FEB-C (*amp_cal*) allows monitoring of the injected pulses. Alternatively, an external pulse generator can be connected to the *amp_cal* pad [89].

Linearity is a crucial parameter of the internal pulse generator. It is tested by recording the *amp_cal*–pad waveforms for different settings of the corresponding 8-bit pulse injection–DAC with an oscilloscope. Figure 6.2 shows the recorded amplitudes over the full dynamic range of the internal pulser. A first-order polynomial is fitted to the data whereby the end points of the fit are determined by the first and last data point. It results in a slope of 0.53 mV/LSB. The graph on the right of Figure 6.2 displays the deviations of the individual data points to the fit. The integral non-linearity (INL), defined as the maximum deviation, is 2.6 mV. This result is considered acceptable for the usage of the internal pulse generation circuit in the ASIC calibration and further testing of the chip.

6.3.2 CSA discharge time constant

A 6-bit register (IFED) allows one to adjust the CSA feedback resistance. Higher register values correspond to a higher feedback resistance. Figure 6.3 shows the waveforms at the outputs of the slow shaper, the fast shaper, and the PSC for several register settings. Both signal polarities are shown, holes in the top row and electrons in the bottom row. As expected, the discharge time constant increases with higher feedback resistance.

For the slow and fast shapers to work as designed, the CSA output should be approximately constant over the course of the shaping time. Hence, moving towards shorter CSA decay times, the shapers start to develop more and more undershoot. As the decay times for electrons are

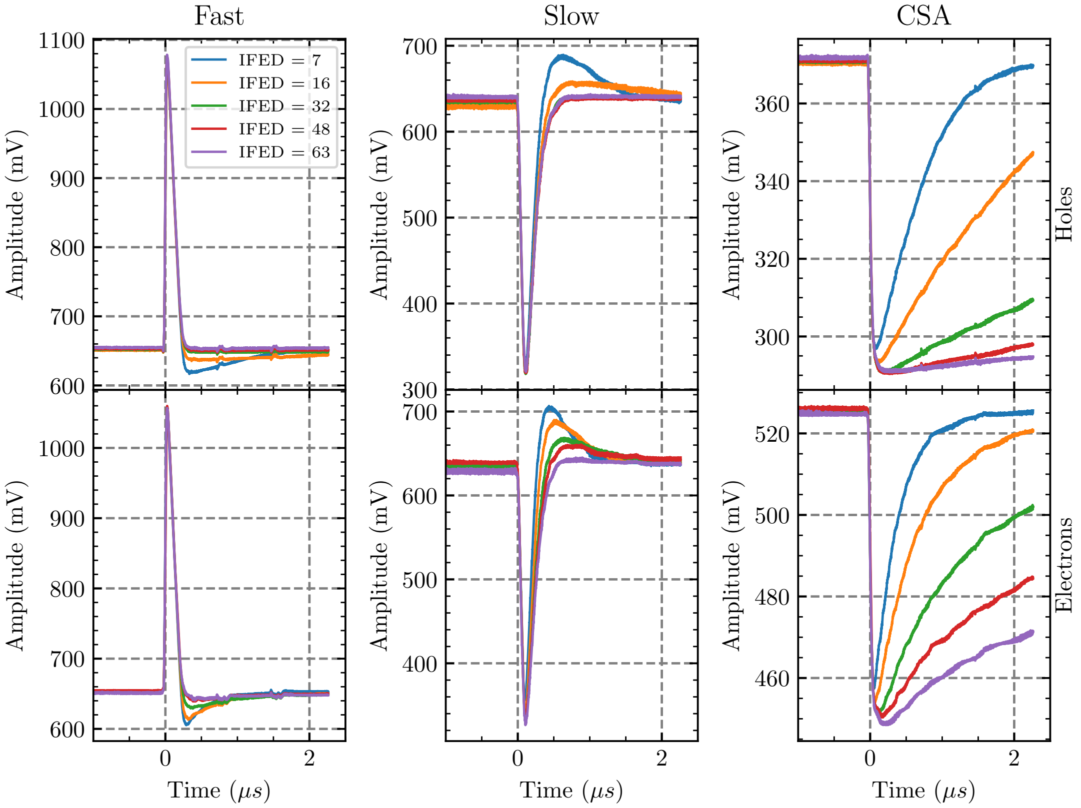

Figure 6.3: Waveforms at the outputs of the fast shaper, the slow shaper, and the CSA for several settings of the feedback resistance. Holes are shown in the top row, electrons in the bottom row.

shorter, this effect is more pronounced for electrons. Figure 6.4 shows the CSA waveforms for both signal polarities for a longer time interval of 100 µs, including an exponential fit to the data. A significant discrepancy between polarities is observed. The decay times are considerably longer for holes, especially for higher feedback resistance values. Table 6.1 lists the CSA decay times extracted from the exponential fits to the waveforms for different values of the IFED register, including the smallest and largest possible value. Additionally, the corresponding feedback resistance $R_f = \tau / C_f$ has been determined, where C_f =100 fF.

6.3.3 CSA fast reset

The STS-XYTER2.1 ASIC has an optional pulsed reset feature which can be used to quickly bring the CSA output voltage back to the baseline after time and amplitude measurement. Figure 6.5 on page 81 shows the waveforms of the slow shaper, fast shaper, and CSA with the fast reset turned on. The indicated rise times represent the time during which the signal rises from 10 % of the amplitude to the full amplitude. For this measurement, the input charge was

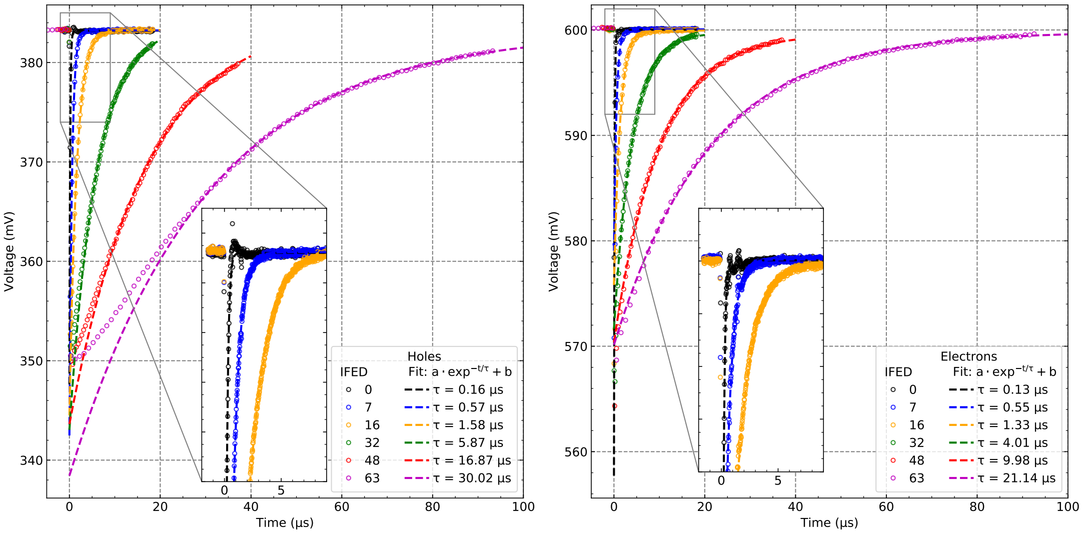

Figure 6.4: CSA discharge time constants for both signal polarities for different values of the feedback resistance. The insets show the indicated area with a 2.5x magnification.

Table 6.1: Measured CSA discharge time constants and calculated feedback resistance ($R_f = \tau / C_f$) for different values of the IFED register.

	Holes		**Electrons**	
IFED (LSB)	τ (μs)	R_f (MΩ)	τ (μs)	R_f (MΩ)
0	0.16	1.6	0.13	1.3
7	0.57	5.7	0.55	5.5
16	1.58	15.8	1.33	13.3
32	5.87	58.7	4.01	40.1
48	16.87	168.7	9.98	99.8
63	30.02	300.2	21.14	211.4

9.6 fC, the register controlling the shaper current was set to its typical value at 31, and the IFED register was set to 48, corresponding to a feedback resistance of 100 MΩ/169 MΩ (e/h).

The fast reset is triggered by the delayed falling edge of the fast comparator. The reset time delay is the time difference between the first appearance of the signal at the CSA until the reset is triggered, indicated by the two vertical dashed lines in Figure 6.5. It is approximately 325 ns/340 ns (e/h). Equivalently to the non-reset mode of operation, the CSA discharge time constant is determined by fitting an exponential during the decay. For the aforementioned chip settings the time constants are 18 ns/31 ns, corresponding to a feedback resistance of 180 kΩ/310 kΩ (e/h). The transients of the fast and slow shaper (shortest peaking time) end well within 1 μs, even for the 9.6 fC input pulse charge. This yields a maximum average input rate of ∼1 MHz.

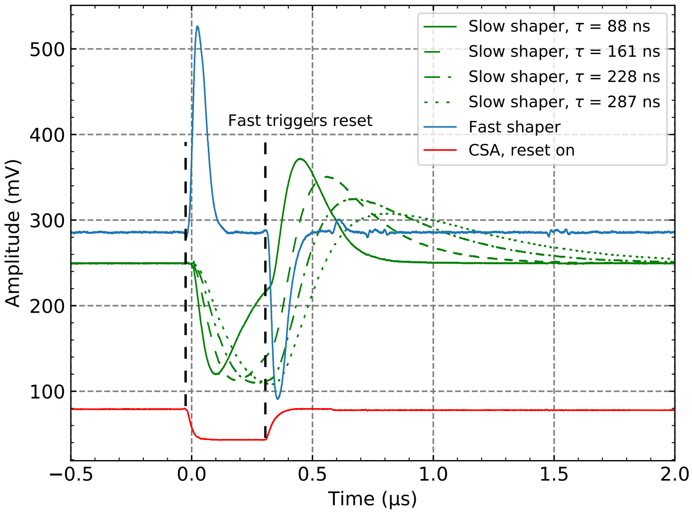

Figure 6.5: Operation of the pulsed reset used for CSA baseline restoration after time and amplitude measurement. Hole polarity. (R_f = 169 MΩ, Q_{in} = 9.6 fC).

It can be observed that the fast reset is activated close in time to when the slow shaper reaches its peak for the two longest shaping times. In the next ASIC revision—the STS-XYTER2.2—the fast reset will act earlier and for a shorter period of time to enable an even faster recovery to the baseline. This will prevent the usage of the longest peaking times in conjunction with the CSA reset.

6.3.4 Linearity and gain of the slow and fast shaper

The shaper linearity and gain are extracted by injecting charge pulses of varying amplitude into the CSA input and measuring the corresponding signal amplitude at the output of the shaping circuit. Figure 6.6 shows the slow and fast shaper waveforms for holes polarity for input amplitudes covering the full dynamic range of the ASIC from 0 fC to 14.32 fC. The slow and fast shaper gain is extracted from the waveform amplitudes. They are both shown for both signal polarities in Figure 6.7. The slow shaper expresses linear behavior over the full dynamic range of the ASIC. Considering the MPV of approximately 4 fC for charge creation in the STS sensors by a MIP, the linearity performance is more than sufficient. The fast shaper keeps linearity up to approximately 6 fC which is sufficient to allow for the adjustment of threshold settings for time-stamping of the hits. A first-order polynomial fit to the data results in a gain of 46 mV fC^{-1}/49 mV fC^{-1} and 29 mV fC^{-1}/30 mV fC^{-1} (e/h) for the fast and slow shaper, respectively.

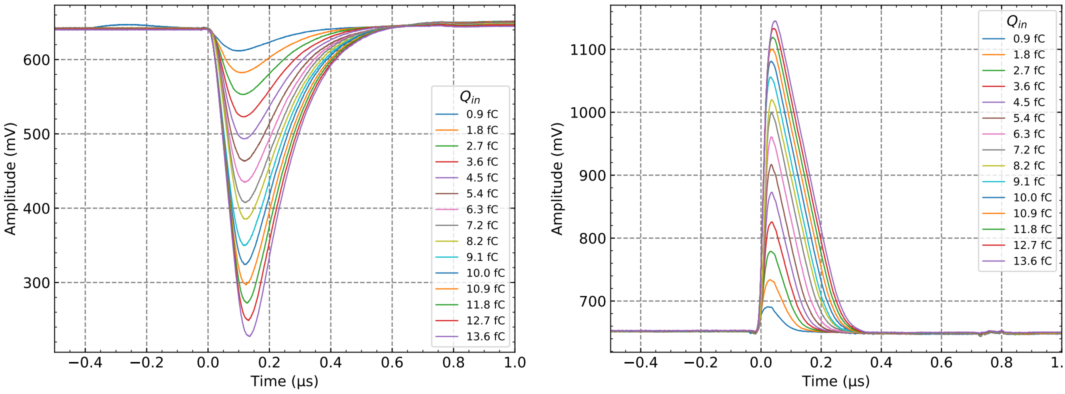

Figure 6.6: Slow shaper (left) and fast shaper (right) waveforms for injected charges over the full dynamic range of the ASIC. Hole polarity.

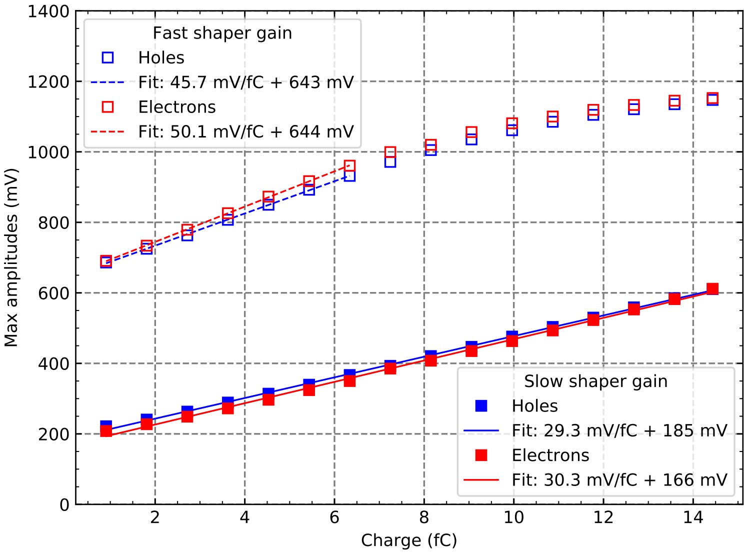

Figure 6.7: Slow and fast shaper gain for both signal polarities determined with a charge scan of the internal pulse generator.

6.3.5 ASIC calibration

The calibration procedure established for the predecessor chip STS-XYTER2 [112] can be adopted for the STS-XYTER2.1. To obtain accurate results, the ASIC must be calibrated for the desired dynamic signal range. Individual trimming DACs for each threshold discriminator in each channel enable fine-tuning of the thresholds to achieve the correct global ADC threshold and good ADC linearity. Figure 6.8 shows the response for all 31 threshold discriminators of one ASIC channel before and after calibration. The effective threshold in units of the calibration pulse amplitude is the value at which the discriminator counter has reached half

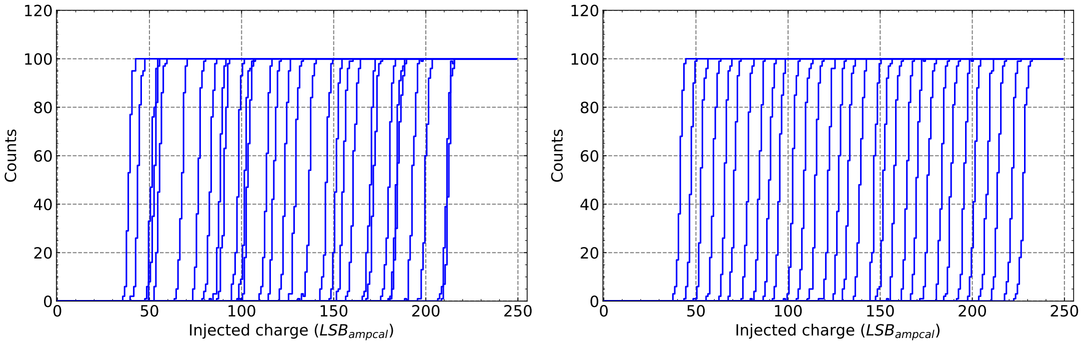

Figure 6.8: Comparison of the response of all 31 threshold discriminators in a single channel before and after calibration.

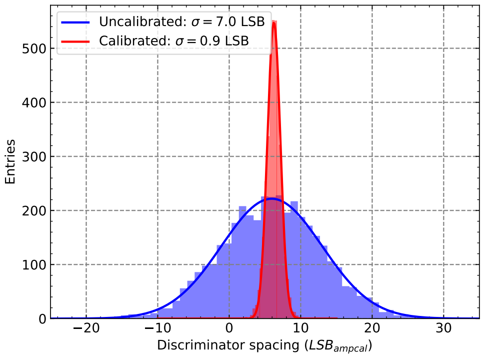

Figure 6.9: Distribution of discriminator threshold spacing before and after calibration for all channels of the same chip used in Figure 6.8.

the number of injected pulses. In order to get a quantitative understanding of the effect of calibration, one can plot the distribution of the discriminator threshold spacing before and after calibration and extract its standard deviation, as illustrated in Figure 6.9. For this particular ASIC, the calibration improved the threshold spacing uniformity by more than a factor of seven.

From the s-curves, the ADC transfer function and thus the ADC linearity can be extracted by plotting the effective threshold over the ADC discriminator number and fitting a first-order polynomial to it. Figure 6.10 shows the ADC transfer function for a single channel before and after calibration. The value of the fit for the lowest-threshold discriminator (#31) gives the ADC threshold, while the slope yields the ADC gain. For a more detailed description of the calibration procedure, please see reference [112].

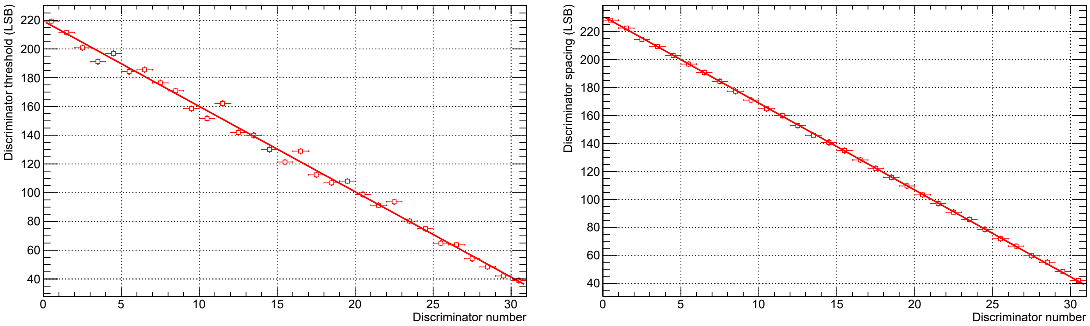

Figure 6.10: ADC transfer function of a single channel before (left) and after (right) calibration.

6.3.6 ADC global threshold scan

One of the novel features implemented in the STS-XYTER2.1 is the ability to choose between four different dynamic ranges of the global ADC threshold, determined by the $v_{\mathrm{ref,t}}$ potential. In contrast, the STS-XYTER2.0 offered only one rather large dynamic range of the ADC threshold with a resolution of ∼2000 e^-. The four dynamic ranges available in the STS-XYTER2.1 are selected by a combination of three bits, two of them being the LSBs of a 6-bit DAC, the third bit belonging to another register. They are referenced with 3’b000, 3’b001, 3’b010, and 3’b100. Each dynamic range has a 6-bit resolution (0 to 63). For each range, a threshold scan was performed between values of 44 and 58 of this register. Figure 6.11 shows results of the threshold scans for both signal polarities for all of the four dynamic ranges of the $v_{\mathrm{ref,t}}$ potential. Each set of data was fitted with a first-order polynomial. The IFED register controlling the feedback resistance was set to 31.

The slope of the fit is systematically higher for electrons compared to holes. Currently, this behavior is not fully understood and a topic of further investigations. For electron polarity, the signal passes through the PSC which is comprised of an inverting amplifier with a designed gain of 1. In practice, the gain of this amplifier is not exactly 1, leading to slight deviations in the intrinsic gain of the ASIC between polarities.

The measurements were repeated for the largest dynamic range (3’b001) with additional external low-leakage capacitors shunting the input. With increasing capacitance the threshold level rose for holes, but dropped for electrons. Naively, one expects the former behavior, as the growing capacitance leads to increased charge sharing and hence a reduced gain. Thus, a higher input charge is required to exceed the threshold. The discrepancy between polarities might be explained due to the pulse shapes of the injected pulses, which can be different for holes and electrons. Different pulse shapes will lead to different shifts in the DC baseline at the shaper output, which might explain the deviations in the behavior of the ADC threshold. This can be verified by observing the analog waveforms at the shaper output for both polarities and variable input capacitance with a focus on the baseline shift introduced by pulse injection. Additionally, the frequency of pulse injection (≈500 Hz) can be reduced by adding software delays.

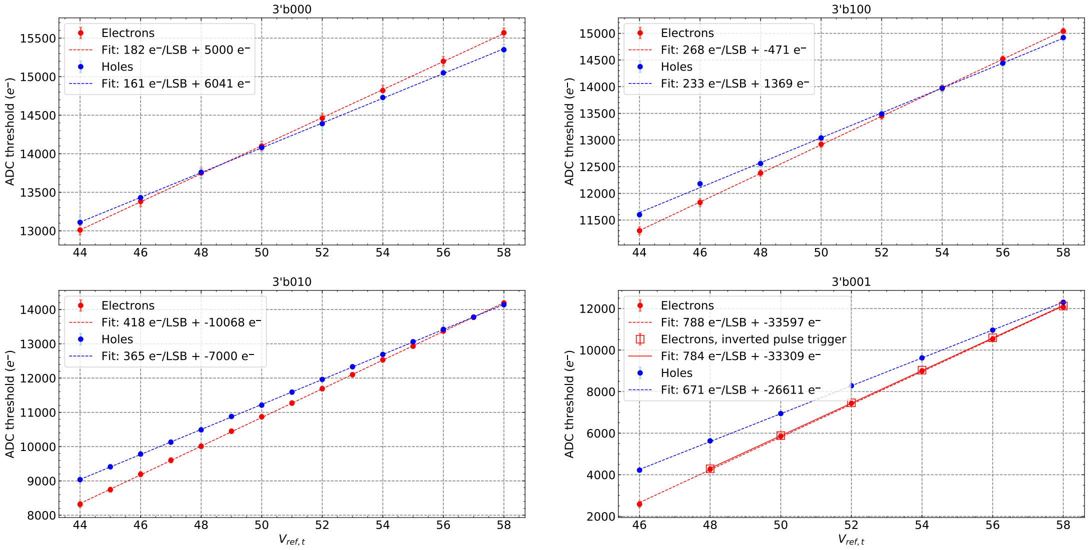

Figure 6.11: ADC threshold scan for both signal polarities for all of the four selectable dynamic ranges of the $\mathrm{v_{ref,t}}$ potential. The electron slope is consistently higher.

Table 6.2 summarizes the slopes—which represent the ADC threshold resolution—extracted from the fits and compares them to the nominal values, taken from [89]. Apparently, the ranges 3'b001 and 3'b100 have been accidentally swapped. The slope of the largest and smallest dynamic range differ by a factor of approximately four, allowing great flexibility in fine-tuning of the noise discrimination. However, the measurements show that one cannot exploit the full theoretically possible range of the larger dynamic ranges, as the threshold will move below the noise baseline of ~2000 $\mathrm{e^-}$ at a certain value of the $\mathrm{v_{ref,t}}$ potential. By extrapolating the ADC threshold to the maximum value of the $\mathrm{v_{ref,t}}$ potential and subtracting the offset, the dynamic ranges can be calculated. They are presented in the middle row of Table 6.2. Additionally, the maximum value of the $\mathrm{v_{ref,t}}$ potential is presented. It is designed to be the same for each dynamic range.

6.4 Systematic noise study

There are three major contributors to the overall noise of the STS detector readout system: the intrinsic noise of the CSA which is dominated by its input transistor, the shot noise generated by the detector leakage current, and white thermal noise of the resistive elements of the circuit (bias resistors, readout electrodes, microcable traces).

Regarding the readout front end implemented in CMOS technology, there are two major noise sources. In the saturation regime, the input transistor of the CSA exhibits a thermal noise spectrum $v_{na}^2 = 4kT\alpha\gamma/g_m$, with the transconductance g_m and two technology dependent numerical values α and γ [119]. The second noise component has a spectral density inversely

Table 6.2: ADC threshold resolution , dynamic range, and maximum possible threshold for the four different dynamic ranges of the global ADC threshold selectable in the STS-XYTER2.1. If available, nominal values are shown for comparison.

	Polarity	**3'b000**	**3'b100**	**3'b010**	**3'b001**
ADC thr. resolution, measured (e^-/LSB)	e	182	268	418	788
	h	161	233	365	671
ADC thr. resolution, nominal (e^-/LSB)	e/h	135	562	307	199
Dynamic range, measured (e^-)	e	11466	16884	26334	49644
	h	10143	14679	22995	42273
Dynamic range, nominal (e^-)	e/h	8650	35900	19600	12700
Largest value, measured (e^-)	e	16466	16413	16266	16047
	h	16184	16048	15995	15662

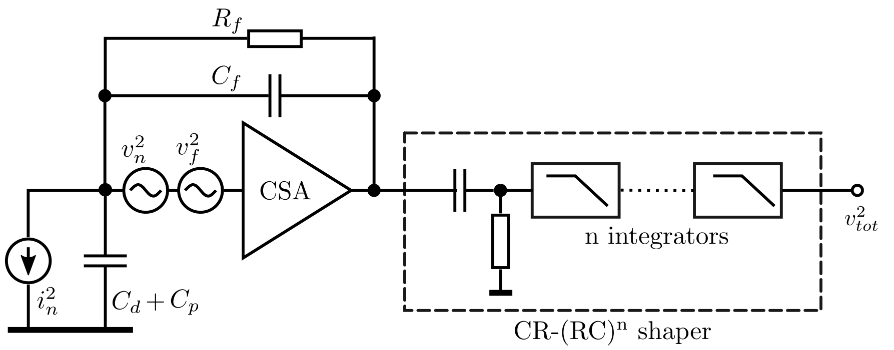

Figure 6.12: Noise model of a detector readout system including a CSA and a CR-(RC)^n shaper.

proportional to the frequency, therefore called 1/f noise or flicker noise. The equivalent input 1/f noise is $v_f^2 = \frac{K_f}{C_{ox}^2 WLf}$ [62]. Here, W and L are the width and length of the gate of the input transistor, C_{ox} is the oxide capacitance, and K_f the 1/f noise coefficient of the specific CMOS technology.

The equivalent input voltage and current noise generators of the readout front end are [62]

$$v_{ia}^2 = v_{na}^2 + v_f^2 = 4kT\alpha\gamma/g_m + \frac{K_f}{C_{ox}^2 WLf}, \tag{6.1}$$

$$i_{ia}^2 = |s(C_{GD} + C_{GS})|^2 \, v_{ia}^2 \quad , \tag{6.2}$$

where C_{GD} and C_{GS} are the gate-drain and gate-source capacitances of the input MOS transistor and $s = j\omega$. Regarding the full STS detector module, the noise can be grouped in three equivalent noise sources [119]:

- parallel current noise i_n^2 caused by the detector shot noise, bias resistors and feedback resistors
$$i_n^2 = 2eI_{leak} + \frac{4kT}{R_b} + \frac{4kT}{R_f} + i_{ia}^2\,, \tag{6.3}$$
- series voltage noise v_n^2 caused by thermal noise of series resistors and thermal noise of the CSA
$$v_n^2 = 4kTR_{Al} + 4kTR_{cable} + 4kTR_{inter} + v_{na}^2\,, \tag{6.4}$$
- 1/f noise v_f^2 caused by the CSA
$$v_f^2 = \frac{K_f}{C_{ox}^2 WLf}\,. \tag{6.5}$$

The total noise power spectrum at the output of the CSA is

$$v_{oa}^2(s) = \left|\frac{C_d + C_p + C_f + C_{GD} + C_{GS}}{C_f}\right|^2 (v_n^2 + v_f^2) + \left|\frac{1}{sC_f}\right|^2 (i_n^2 - i_{ia}^2) \quad , \tag{6.6}$$

where C_d, C_f, and $C_p = C_{cable} + C_{PCB}$ are the detector capacitance, feedback capacitance, and the parasitic capacitance of the interconnection between the detector and the amplifier input. Weighting the noise power spectrum by the transfer function of the shaper (see eq. (2.21) on page 26) yields the total integrated rms noise

$$v_{tot}^2 = \int_0^\infty |v_{oa}(s)|^2\, |H(s)|^2\, df\,. \tag{6.7}$$

To calculate the equivalent noise charge (ENC), v_{tot}^2 has to be divided by the peak amplitude at the shaper output due to one electron charge q

$$V_{out,max} = \frac{qA^n n^n}{C_f n! \mathrm{e}^n}\,. \tag{6.8}$$

Here, n represents the shaper order. As the noise power spectrum has three independent components, the integral in eq. (6.7) can be split into three independent integrals to calculate the ENCs separately. The total ENC is then simply given by adding the individual ENCs in quadrature

$$ENC_{tot} = \sqrt{ENC_i^2 + ENC_v^2 + ENC_{1/f}^2}\,. \tag{6.9}$$

Performing the integration one obtains

$$ENC_{tot}^2 = v_n^2 \frac{C_{tot}^2}{\tau_s} F_v + i_n^2 \tau_s F_i + C_{tot}^2 A_f F_f\,, \tag{6.10}$$

where τ_s is the time constant of the shaper, $C_{tot} = C_d + C_p + C_f + C_{GD} + C_{GS}$, and F_i, F_v, F_f are numerical values depending mainly on the shaper order. For the approximate CR-(RC)^2 shaper implemented in the slow path of the STS-XYTER2.1, they have been estimated to be

Table 6.3: Contributors to the current and voltage noise in the STS module [119].

Parameter	**Typical value**
R_{bias}	$1.5\,\mathrm{M\Omega}$
R_f	$20\,\mathrm{M\Omega}$
I_{leak}	$4\,\mathrm{nA}$
R_{Al}	$10.5\,\Omega\,\mathrm{cm}^{-1}$
R_{cable}	$0.6\,\Omega\,\mathrm{cm}^{-1}$
I_{inter}	$15\,\Omega$
CSA	$\alpha = 0.5$, $\gamma = 1$ $g_m = 0.044\,\mathrm{A\,V^{-1}}$

0.64, 0.85, and 3.41, respectively. Significant contributors to the current and voltage noise in the STS detector module are given in Table 6.3.

6.4.1 Methodology of noise measurements

In order to conduct the noise measurements for the STS-XYTER2.1, a single ASIC is bonded onto a FEB-C. The noise performance evaluation in this relatively simple system enables the optimization of the ASIC configuration and operation. Critical issues at the ASIC level can be identified early on. The reduced system complexity facilitates establishing clear dependencies of the noise with regards to variable chip settings, environmental changes, or other parameters.

For the noise measurements, input signals with increasing amplitudes are injected into the CSA input of each channel followed by the readout of the counters of all channel discriminators in a so-called s-curve scan. Ideally, the discriminator response is a step function. In reality, this step function is smeared by electronic noise, resembling more of an ‘S’-shape, as illustrated in Figure 6.13. The discriminator response is fitted with the complementary error function

$$f(x) = \frac{N}{2}\left(1 + erfc\left(\frac{x-\mu}{\sqrt{2}\sigma}\right)\right) + y_0 \quad . \tag{6.11}$$

Here, N is the number of injected pulses and y_0 some arbitrary offset. The mean μ, taken at the 50 % mark, indicates the effective discriminator threshold, while the width σ yields the noise. The channel noise is determined by averaging over all 31 ADC discriminators, whereas for the fast path it equates to its one and only discriminator. If there is a clear separation between the noise background and the lowest discriminator, it is in principle sufficient to only consider this discriminator in the estimation of the effective system noise [112]. Large noise in the fast path does not influence the overall system noise, but it does affect timing precision.

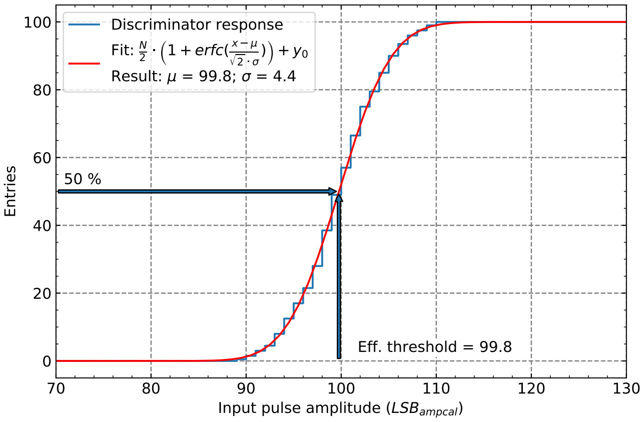

Figure 6.13: Typical response of a single ADC discriminator. Fitting the complementary error function to the discriminator response yields the discriminator threshold and noise.

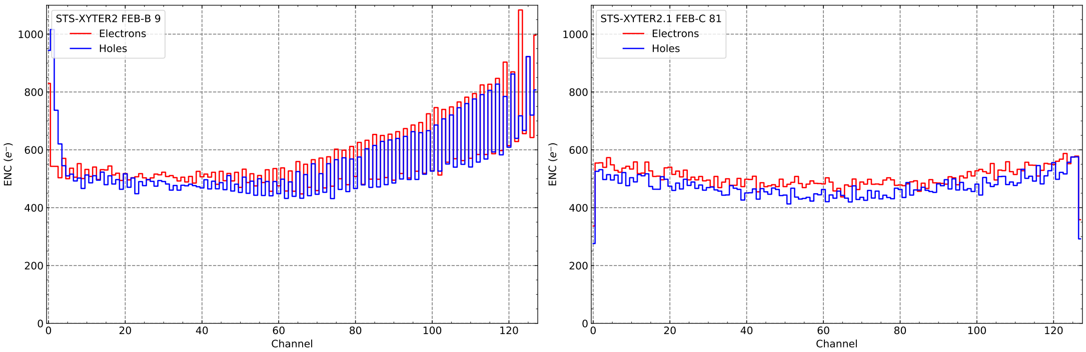

Figure 6.14: Comparison of ENC levels between the STS-XYTER2 (left) and the successor chip STS-XYTER2.1 (right) for all 128 channels of one ASIC.

6.4.2 Comparison of noise performance of the STS-XYTER2.1 and STS-XYTER2.0

Before diving deeper into the noise performance of the STS-XYTER2.1 under various settings and conditions, it is now a good place to compare the noise behavior of the STS-XYTER2.1 and the STS-XYTER2.0. Figure 6.14 shows the ENC for all channels of one STS-XYTER2.0 bonded onto a FEB-B next to one STS-XYTER2.1 bonded onto a FEB-C. Clearly, the chip modifications described in section 6.1 on page 75 have been successful. Both the noise discrepancy between odd and even channels as well as the higher noise towards higher channels are reduced dramatically. In the STS-XYTER2.1, the noise increases only marginally towards the chip edges. Apart from that, the overall noise level stayed the same, as can be seen by looking at the lower channels of both chips.

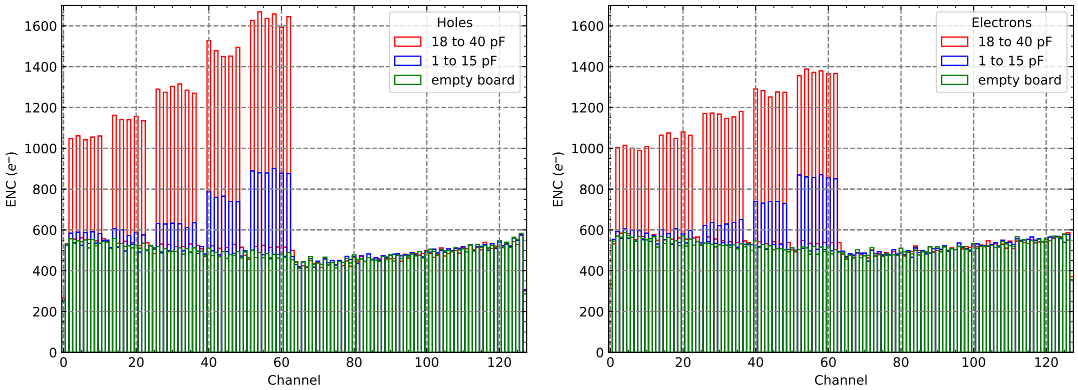

Figure 6.15: ENC levels in the STS-XYTER2.1 for three different capacitor boards attached to the even channels in the range 0 to 63. Left: holes. Right: electrons.

6.4.3 Noise dependence on input load capacitance

The noise of the readout front end strongly depends on the total capacitive load seen by the CSA input transistor [120]. Due to varying sensor sizes and microcable lengths among the individual modules in the final STS detector the capacitive loads are in the range of 12 pF to 40 pF [121, 122]. Therefore, the noise dependence on the capacitive load is tested with two dedicated capacitor boards simulating the sensor and microcable capacitance. Each board comprises a 64-channel ERNI connector with low-leakage C0G SMD capacitors with capacitances ranging from 1 pF to 40 pF soldered to the even channels.

The capacitance values are cross-checked with a Peak Tech 2155 LCR meter. During the measurements, the capacitor boards are connected to the low-channel ERNI connector of the FEB-C, i.e. channels 0 to 63. Charge pulses are injected into the CSA input Using the internal pulse generator of the ASIC. Figure 6.15 shows the ENC for all ASIC channels for both polarities with three different capacitor boards attached to the FEB-C, while Figure 6.16 displays the evolution of the ENC with increasing input capacitance for both signal polarities. As expected from eq. (6.10) on page 87, the ENC rises linearly with the input capacitance, caused by the series voltage and 1/f noise contributions. Correspondingly, experimental data are fitted with a straight line, yielding a slope of 21.7 e^-/pF and 28.7 e^-/pF for electrons and holes, respectively. The intersection of the fit lines with the ordinate axis corresponds to the noise levels of the STS-XYTER2.1 bonded onto a FEB-C. This rather large discrepancy between holes and electrons currently is not well understood and a topic of further investigations.

The described parametrization of the noise based on the input capacitance alone neglects the sensor leakage current. Nevertheless, it allows for an estimation of the system noise for various sensor and microcable combinations (i.e. varying input capacitance) later on. In case of low leakage current—like in the non-irradiated sensors used throughout this work—this parametrization is expected to be a valid approximation of the system noise.

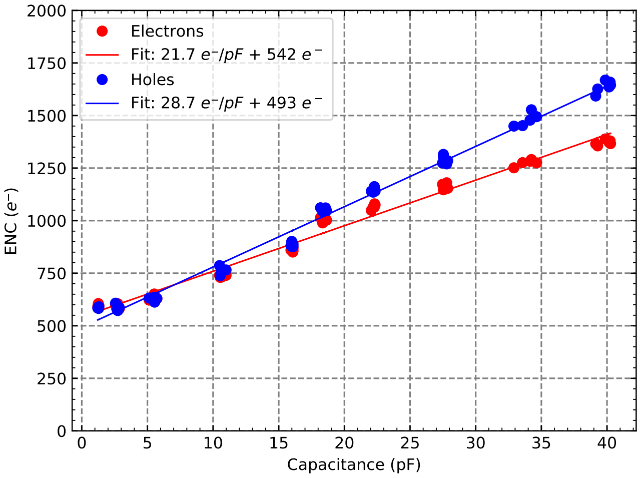

Figure 6.16: ENC as a function of input load capacitance, extracted from Figure 6.15.

6.4.4 Noise dependence on slow shaper peaking time

In order to find the optimum trade-off between speed and noise, the approximate CR-(RC)^2 slow shaper allows the selection of four different peaking times, 90 ns, 160 ns, 220 ns, and 280 ns. One key function of the pulse shaper is to improve the SNR of the readout system. In practice, other factors such as pile-up suppression and counting rate behavior have to be considered as well to find the optimum pulse shaper.

The slow shaper peaking times in the STS-XYTER2.1 are selected by a 2-bit DAC which modifies appropriate resistance values in the signal processing chain. Figure 6.17 on page 92 shows the ENC for all four possible slow shaper peaking times for three different test setups. The base setup comprises a single ASIC bonded onto a FEB-C. In the two remaining setups, the same FEB-C is connected via ERNI connectors to a 62 mm × 42 mm and 62 mm × 62 mm sensor, respectively. Each data point represents the ENC averaged over all channels, while the error bars indicate the standard deviation. Clearly, an increased input capacitance leads to an increased ENC, independent of shaping time. Independent of the setup, the ENC stays constant within the error bars amongst the different shaping times. For the FEB-C setup, electrons show a slightly higher noise which can be contributed to the PSC present in the electron signal processing chain. For the larger setups, the influence of the PSC is not as clear. Here, other factors such as the ERNI connectors themselves, the fan-out leading into them, and the sensor board contribute to the overall noise behavior, resulting in a larger variance between channels.

6.4.5 Long-term stability investigations

CBM will be a multi-year experiment with extended periods of continuous run-time. Therefore, reliable long-time performance of the electronics is essential. Long-term stability tests of the

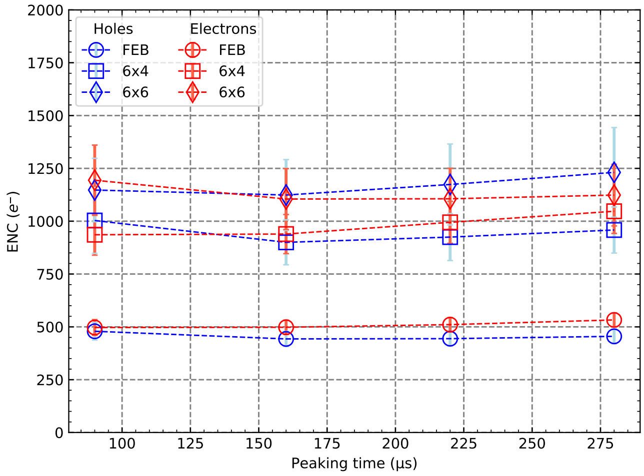

Figure 6.17: ENC for both polarities for all four possible slow shaper peaking times for the STS-XYTER2.1 on a FEB-C, on a FEB-C with a 62 mm × 42 mm sensor attached, and on a FEB-C with a 62 mm × 62 mm sensor attached. Sensors are attached with ERNI connectors and asymmetrically biased to 150 V.

STS-XYTER2.1 help identify sources of malfunction which might be overlooked in short-time tests. These include faulty ground connections, unstable power supplies, the connection of high-current devices in the same power line, electromagnetic interference, or changes in the ASIC working temperature.

Stability tests are performed for two test setups. The base setup comprises a single ASIC bonded onto a FEB-C. In the second setup, the same FEB-C is connected via ERNI connectors to a 62 mm × 62 mm sensor. The ADC threshold, ADC gain, and ENC are recorded every 15 min for several hours of continuous operation for both signal polarities. The results are summarized in Figure 6.18 on page 93. Each data point represents the average over all channels, while the error bars indicate the standard deviation. All three observed parameters are stable over the measurement periods of 15 h to 25 h. Especially the most important figure—the ENC—shows no significant fluctuations. The results of these measurements, even if they were not extended over a long period of time, could be considered satisfactory for identifying noise sources or fluctuations in the laboratory environment. Additionally, they represent a reference for future long-term studies with fully assembled modules.

6.5 Radiation studies with a 50 MeV proton beam

The STS detector module must withstand the CBM expected lifetime total ionizing dose (TID) of 10 kGy. Regarding the microcables and interconnects, the components most susceptible to radiation damage are the adhesives. Adhesives used in the STS frontend electronics are silver glue as die attach, and glob top as wire bond and ASIC protection. In case of the copper

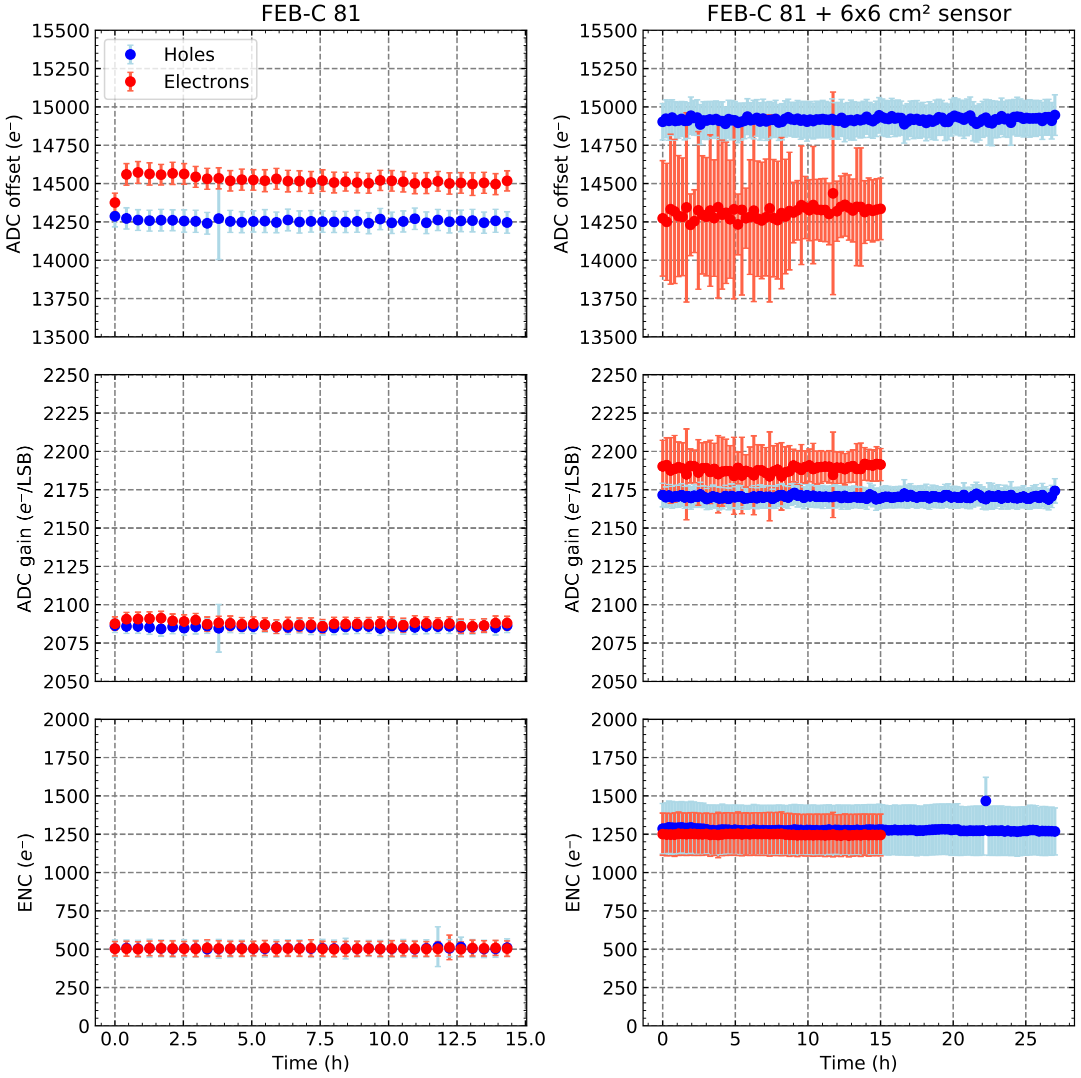

Figure 6.18: Long-term stability test of ADC offset, ADC gain, and ENC for the STS-XYTER2.1 on a FEB-C without (left) and with (right) a 62 mm × 62 mm sensor attached via ERNI connectors.

technology, further adhesives are found in the microcables laminating the individual layers, as well as the underfill glue protecting the gold bump–solder interconnection.

In order to verify the radiation tolerance of the STS-XYTER2.1 ASIC in combination with the glob top materials Dymax 9001 and Dymax 9008, STS scheduled an irradiation campaign with 50 MeV protons at the Proteus C–235 facility at the Institute of Nuclear Physics in Cracow, Poland, in December 2019. Additionally, the campaign was used to test the radiation hardness of the gold stud-solder interconnection technology, albeit being unlikely to fail for a TID of 10 kGy. During the irradiation at RT, the ASIC was not powered. The TID of 10.4 kGy was reached in 25 min, yielding a dose rate of 25 kGy h^{-1}. The dose has been calibrated with

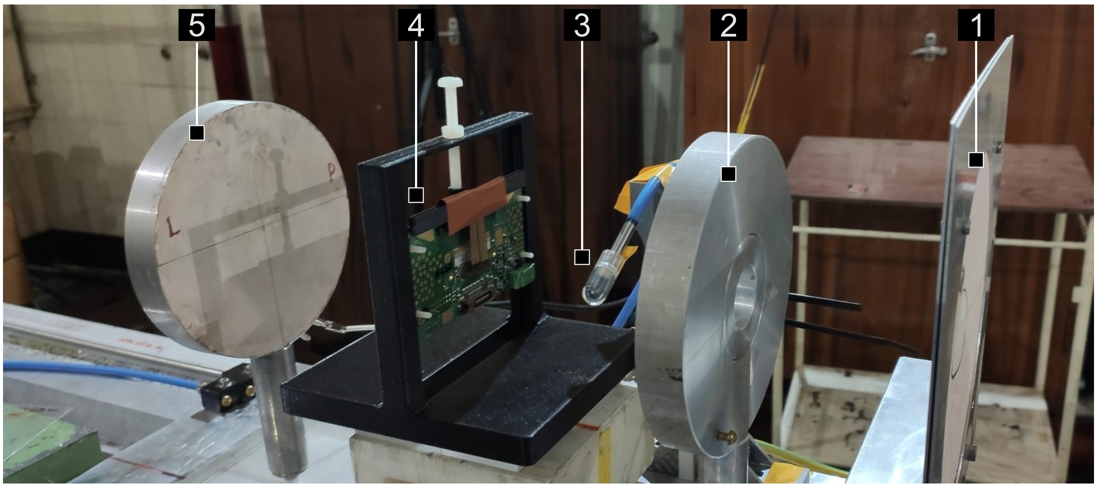

Figure 6.19: Experimental setup during the irradiation campaign at the Proteus C-235 facility in Cracow. The proton beam enters from the right. It passes a luminescent foil (1) for beam detection, a collimator (2), and an ionization chamber (3) used for calibration before reaching the device unter test (4) and finally the beam dump (5).

the help of an ionization chamber and a UNIDOS electrometer. The ASIC including the interconnection have been uniformly irradiated with a beam spot diameter of around 4 cm and a beam fluence of 50 nA to 60 nA. The beamtime setup is shown in Figure 6.19 on page 94.

The prevalent covalent bonds in polymers are rather sensitive to ionizing radiation [123]. As a consequence, the physical, chemical, and mechanical properties of polymeric materials are affected by radiation. From a macroscopic point of view, the effects of radiation on epoxies depend on the type of radiation, dose rate, and TID. The two dominant effects of radiation on polymers are the formation of cross-links, i.e. C—C covalent links between the long-chain molecules, and bond breakage, leading to scission of the macromolecules. While a moderate number of cross-links can often improve the physical properties of polymers, the materials can become stiff and brittle at higher cross-link densities. Scission usually results in materials that are soft and weak. In many cases, cross-linking and scission proceed simultaneously. However, when irradiating in the presence of air or water, the radicals formed directly and indirectly by the radiation are immediately attacked by the oxygen atoms and prevented from further processes such as cross-linking.

For adhesive systems, the adhesive-adherend interface typically is quite insensitive to radiation. That said, this statement holds only for well-prepared surfaces without a significant amount of pollutants and oxidants present. As the interface is responsible for the strength of the bonding, no degradation will be observed until the polymer itself starts to degrade. In general, the mechanical degradation occurs before the degradation of the electrical properties [123]. Mechanical properties to be tested are the deformation at break or the modulus of elasticity.

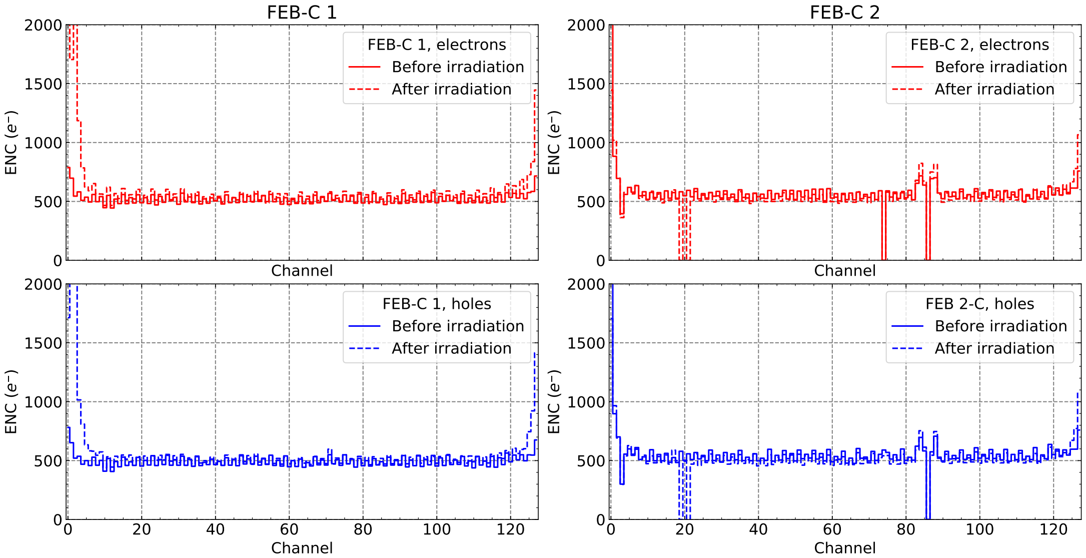

Figure 6.20: ENC over channel number for two FEBs-C hosting one ASIC each. Each graph shows a measurement taken before irradiation compared to a measurement taken several weeks after the irradiation. Top row: electrons. Bottom row: holes.

Two test samples consisting of a FEB-C, STS-XYTER2.1, and 20 cm Cu microcable have been prepared. Polytec EP601-LV underfill glue was applied between the microcable and ASIC. Polytec EP601-LV is a transparent, two-component, optically clear epoxy, ideal for fine cavity filling. The wire bonds connecting the ASIC to the FEB-C have been protected with Dymax 9001 glob top material.

Figure 6.20 on page 95 shows the ENC over channel number for both samples before and after irradiation for both signal polarities. The measurements after irradiation were taken at RT several weeks after the irradiation campaign. It can be observed that the ENC levels are not affected by the irradiation with the ASIC in the non-powered state. The higher noise on the edge channels is contributed to electromagnetic pick-up due to the cables being unshielded. The only channels, except for the edge channels, that express a difference in noise level after the irradiation, are channels 19 and 21 on the FEC-C 2. Looking into the s-curves in channel 19, only one discriminator shows a response, which is noisy. In channel 21, there is no response at all. Probably these channels suffer from radiation damage.

In summary, the quantitative noise analysis gives a first indication of the radiation tolerance of the full test setup, including the chip itself. For conclusive answers to the extent of mechanical or electrical degradation of the polymers, one must perform further measurements.

6.6 Summary

The STS-XYTER2.1 readout ASIC has been subjected to extensive tests, including analog waveforms for various ASIC register settings as well as the quantitative noise performance of the chip under different settings and conditions.

The STS-XYTER2 expressed a significant difference in noise between odd and even channels together with a considerable increase in noise towards the higher channel numbers. With an improved transistor biasing scheme and modifications of the biasing DACs, both of these issues could be resolved successfully in the STS-XYTER2.1.

Due to the removal of the ESD protection circuit, the CSA fast reset now works as expected. Fast reset decay times below 20 ns have been measured for electron polarity. The ASIC-internal pulse generator expresses excellent linearity ($INL = 2.6\,\mathrm{mV}$). Excellent linearity has also been observed for the slow and fast shaper. The slow and fast shaper gain are $29\,\mathrm{mV\,fC^{-1}}/30\,\mathrm{mV\,fC^{-1}}$ and $46\,\mathrm{mV\,fC^{-1}}/49\,\mathrm{mV\,fC^{-1}}$ (e/h), respectively.

Another modification of the STS-XYTER2.1 is the ability to choose between four different dynamic ranges of the global ADC threshold for better control of noise discrimination in the ADC. Hence, the global threshold resolution of the slow path improved from $\sim$2000 $\mathrm{e^-}$ to 182 $\mathrm{e^-}$/161 $\mathrm{e^-}$ (e/h). The noise dependence on input load capacitance was found to be 21.7 $\mathrm{e^-}$/pF and 28.7 $\mathrm{e^-}$/pF for electrons and holes, respectively. The overall noise level is practically independent of shaper peaking time, a consistent finding for various setups of different input capacitance. Long-term tests of the ADC gain, ADC threshold, and ENC for continuous operation over the course of half a day to a day indicate stable chip behavior.

Radiation tests with 50 MeV protons and a TID of 10 kGy have been performed in a non-powered state. No indications of damage to the chip and interconnects could be observed.

All in all, the STS-XYTER2.1 works as expected and fulfills the requirements imposed by the CBM environment. Only minor chip modifications are necessary for the upcoming ASIC revision 2.2 before going into production. In the meantime, the STS-XYTER2.2 has been delivered and tested at GSI. For more information, please see reference [124]. Finally, all these tests, conducted on the ASIC level and on prototype modules, form the foundation for successful assembly and operation of a full detector module and to evaluate its performance within a dedicated beam campaign.

7 Performance Evaluation of STS Copper Detector Modules

The fully customized in-house bonder machine was presented in chapter 5. Together with the knowledge gained from the extensive characterization of the STS-XYTER2.1 readout ASIC, described in chapter 6, the foundations are laid to assemble and characterize small-scale and full-scale STS detector modules in the copper technology.

The assembly and testing of prototype modules with a single ASIC per sensor side described in section 7.1 is followed up by the characterization of full-scale modules in section 7.2. Signal measurements with a radioactive ^{241}Am-source have been performed on a full copper module in section 7.2.4. A comparison of module performance of the aluminium and copper technologies is presented in section 7.3.

7.1 Small-scale prototype modules

While accumulating first experience in the full assembly chain, including the ASIC–microcable, chipcable–sensor, and ASIC–FEB bondings, with all the associated gluing and handling steps, the choice was to build small-scale prototype modules first. The reasoning for this is twofold: reducing the usage of resources (material and time) and receiving a quick feedback on possible difficulties.

Therefore, prototype modules with one chipcable per sensor side have been built. Such a module is shown in Figure 7.2. It consists of a 62 mm × 62 mm CiS sensor and one 20 cm long copper microcable per sensor side, each connected to a STS-XYTER2.1 readout ASIC, which in turn is wire bonded to a FEB-C. The microcables are shielded with copper tape. These prototype modules allow us to gain important knowledge about the electrical and mechanical performance of the copper modules. The connectivity and ENC of individual channels, radiation tolerance of the interconnection, or mechanical reliability can be investigated, albeit it with reduced statistics.

The modules had to be built at KIT in one go without intermediate testing. After having completed all assembly steps, the modules have been tested at the STS detector laboratory at GSI. The test setup is almost identical to the one described in section 6.2, used for testing the ASIC. The p– and n-side are tested separately. For p-side testing, the sensor is biased asymmetrically to 0 V and 150 V on p– and n-side, respectively. For n-side testing, the sensor is biased to −150 V and 0 V on p- and n-side, respectively. The HV bias is transmitted to the

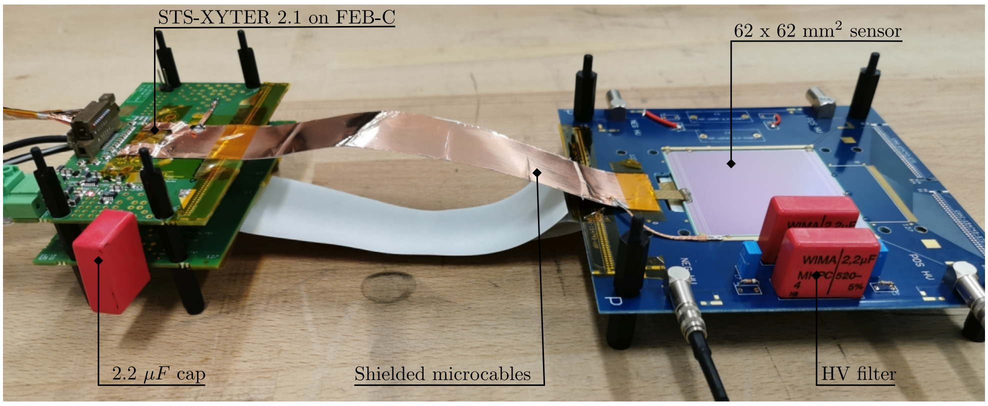

Figure 7.1: Small-scale double-sided copper prototpye module.

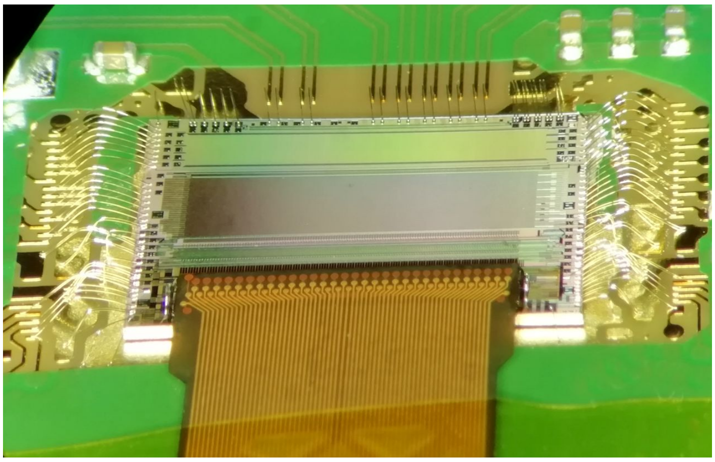

Figure 7.2: Microscopic image of an STS-XYTER2.1 readout ASIC wire bonded to a FEB-C.

FEB grounds via the microcable shielding. The two FEB grounds are connected by a 2.2 µF capacitor while the FEB ground sitting at 0 V is connected to the aluminium shielding box which in turn is connected to earth.

The noise parametrization based on the input capacitance, which neglects the leakage current, gives a good approximation for the expected ENC for the non-irradiated test modules:

$$ENC_{s,n} = 350\,\mathrm{e}^- + \left(0.38\,\frac{\mathrm{pF}}{\mathrm{cm}}\cdot 20\,\mathrm{cm} + 1.52\,\frac{\mathrm{pF}}{\mathrm{cm}}\cdot 6.2\,\mathrm{cm}\right)\cdot 28.7\,\mathrm{e}^-/\mathrm{pF} = 839\,\mathrm{e}^-\,,$$

$$ENC_{s,p} = 350\,\mathrm{e}^- + \left(0.38\,\frac{\mathrm{pF}}{\mathrm{cm}}\cdot 20\,\mathrm{cm} + 1.24\,\frac{\mathrm{pF}}{\mathrm{cm}}\cdot 6.2\,\mathrm{cm}\right)\cdot 28.7\,\mathrm{e}^-/\mathrm{pF} = 789\,\mathrm{e}^-\,.$$

Like in the ASIC testing, the ENC of the individual channels is determined with S-curve scans. Because the capacitive load seen by the CSA will be lower for unconnected channels, the ENC evaluation allows us to identify them—on the ASIC level as well as on the sensor

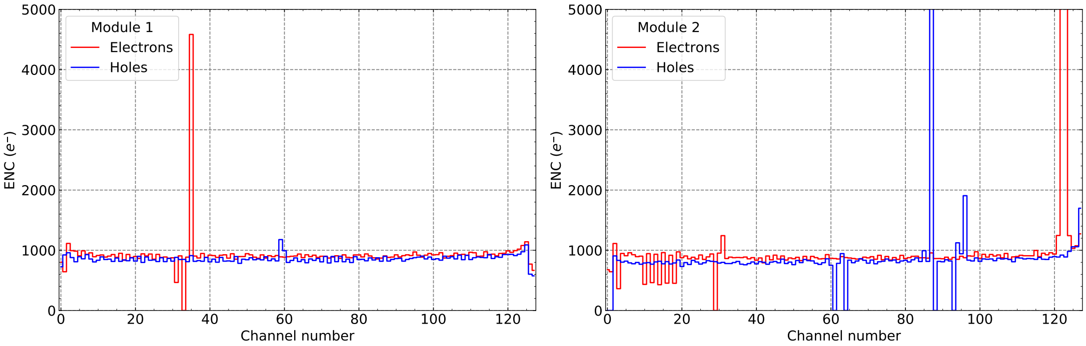

Figure 7.3: ENC over channel number for two small-scale copper prototype modules.

Table 7.1: Summary of performance of small-scale copper prototype modules.

		Dead	**Noisy**	**Disconnected**	**Sum**	**Channel yield** (%)
Module 1	p	0	0	2	2	98.5
	n	0	2	4	6	95.3
Module 2	p	6	3	0	9	93.0
	n	1	2	8	11	91.4
Total		7	7	14	28	94.5

level. However, as the noise contribution of the microcable is ~200 e^-, it can be difficult to differentiate between the two cases. The pattern of unconnected channels can additionally give a hint to the root of the problem. If the channels to one side of the chip are disconnected, there likely is a left-right tilt between the cable and die. If every other channel is disconnected, there might be a tilt in the other direction. However, because of the small distance between the two ASIC rows this failure mode is unlikely. Isolated unconnected channels might be caused by insufficient solder deposition on this particular bond pad. Of course, there can also be processing errors on the cable or sensor, such as metal strip opens, which cause a lower capacitance seen by the CSA.

The results of the ENC analysis for two small-scale copper modules are shown in Figure 7.3. Channels without a proper analog response are set to zero. Channels with excessive noise stand out as spikes. A total of 14 out of the 512 channels appear to be not properly connected, corresponding to 2.7 %. Table 7.1 summarizes the individual failure modes and presents yields for the individual chips as well as the total yield of usable channels, which amounts to 94.5 %. The ENC levels of the properly connected channels are 910 ± 40 e^- and 860 ± 50 e^- for the n- and p-side of Module1 and 890 ± 40 e^- and 830 ± 50 e^- for the n- and p-side of Module2, in good agreement with the expectation.

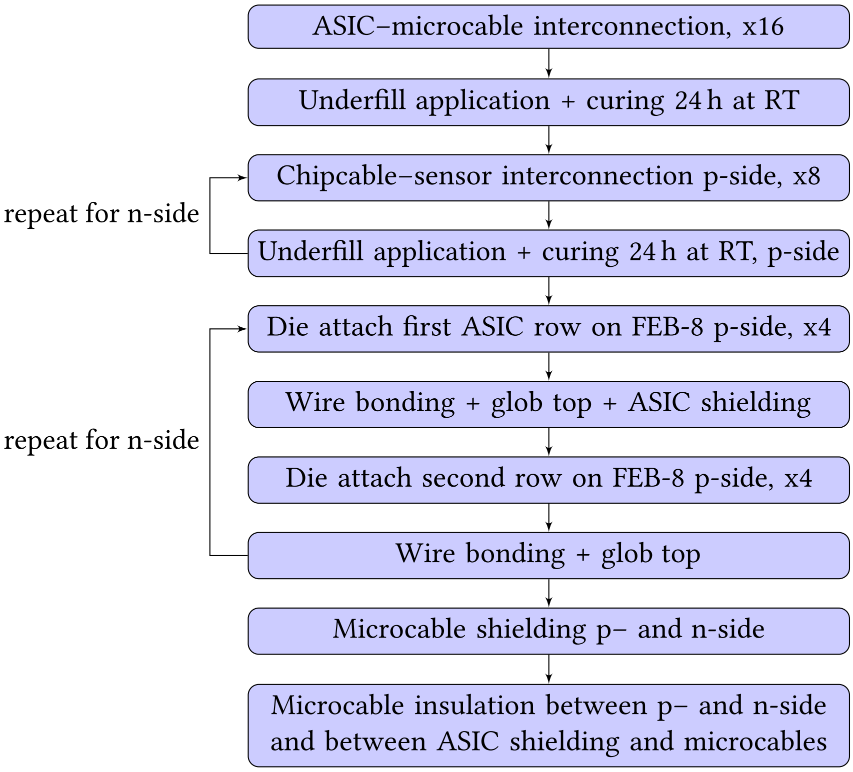

Figure 7.4: Workflow of copper module assembly.

7.2 Full module

Having gained valuable experience through building and testing the small-scale prototype modules, the assembly of a complete detector module in the copper technology could begin.

7.2.1 Assembly considerations

The individual process steps involved in the assembly of a full copper module are listed in Figure 7.4. During die attach, an important observation was made: The increased stiffness of the copper microcable severely complicates assembly. During the die attach of the first row of four ASICs, the microcable has to bend only slightly, because of some low-profile SMD components on the FEB-8 between the ASIC and the FEB edge. Here, the suction forces of the liquid silver glue are sufficient to keep the ASIC flat while the glue cures. However, in bonding the second row of ASICs, the microcable has to overcome a significant height difference between a glob-topped ASIC and the FEB surface over a short distance. Due to the copper microcable stiffness, it is impossible to keep the ASIC flat without pre-bending the microcables or applying an additional external downward force. A dedicated jig was developed for the die attach, shown in Figure 7.5. First, four ASICs are placed on the base in

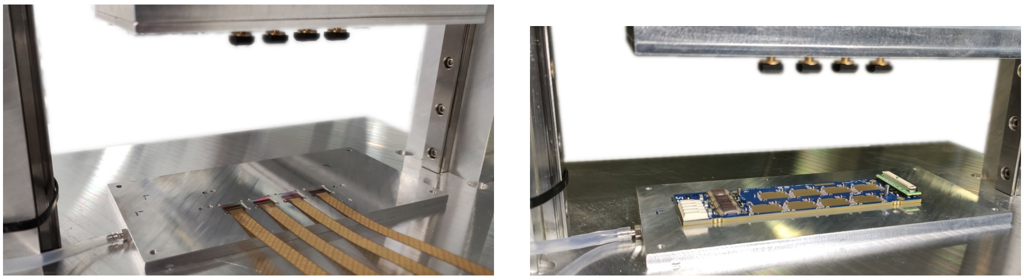

Figure 7.5: Jig developed for precise alignment during the die attach.

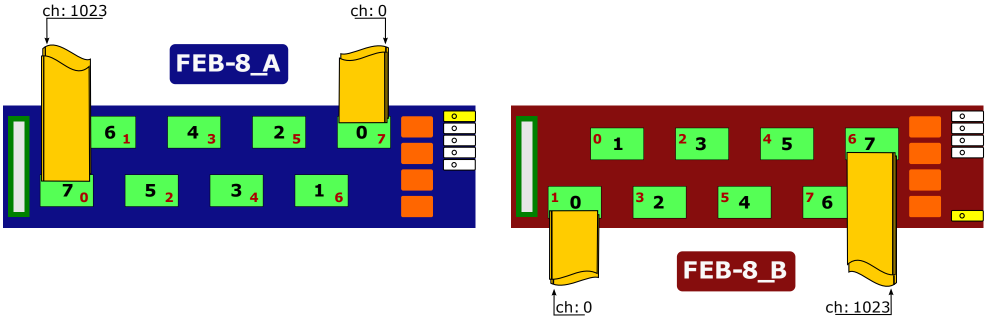

Figure 7.6: Connection scheme for the FEB-8_A2 (n-side) and FEB-8_B2 (p-side) used in the copper module. The black numbers correspond to the ASIC number, while the red numbers indicate the ASIC hardware adress.

precisely machined pockets (covered by the FEB-8 in the image). Second, they are picked up by vacuum bond heads. Third, the FEB-8 is placed on the base. Alignment pins and vacuum suction guarantee precision and stability. After applying silver glue on the FEB-8, the ASICs are bonded with a defined force thanks to the spring loaded bond heads. The fully assembled module Cu_KIT_202 is shown in Figure 7.7. It comprises a 62 mm × 22 mm CiS sensor, 16 microcables with a length of 20 cm, 16 STS-XYTER2.1 readout ASICs, and two FEBs-8. The first row of ASICs is covered by the ASIC shielding. Four LDOs from SCL India, which generate the FEB-8 supply voltages VDD1.8, AVDD1.8 and 2 × AVDD1.2 , are visible on the left. The die attach, wire bonding, and glob topping of the LDOs is performed before the ASIC bonding. Since the copper microcables are not insulated on either side, insulation has to be installed in between the p- and n-side cables, as well as in between the conductive ASIC shielding and the cables.

Figure 7.6 shows the connection scheme for the FEB-8_A2 and FEB-8_B2 used in module Cu_KIT_202, showing the physical location of the numbered ASICs on the FEBs. In the following, if ASICs are referred to by number, the ASIC number is indicated, *not* the hardware address.

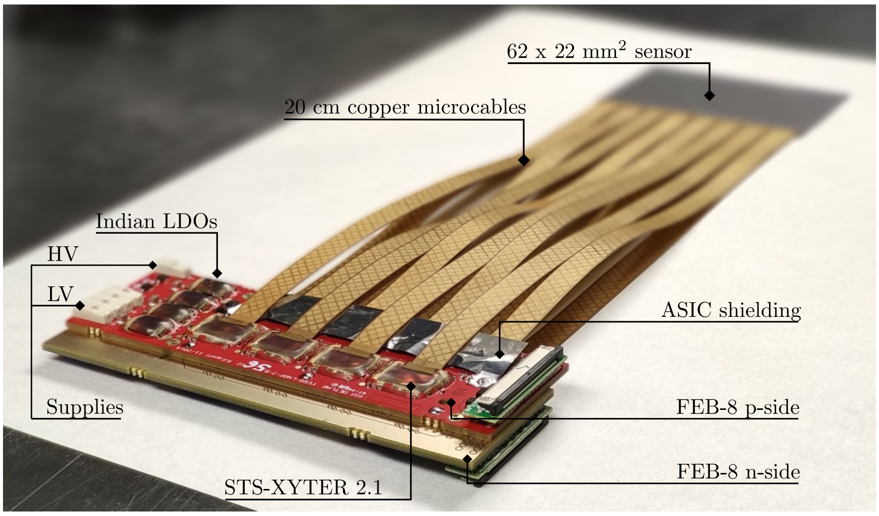

Figure 7.7: Complete STS detector module in copper technology before application of microcable shielding and insulation.

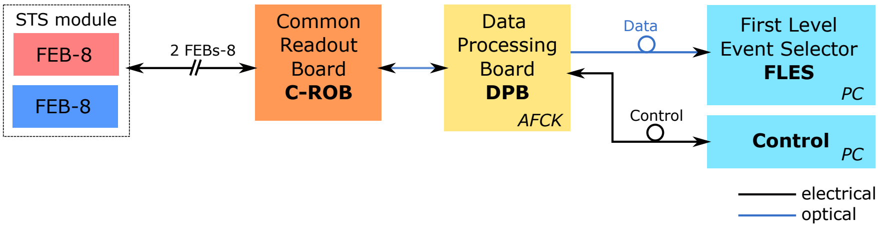

Figure 7.8: Readout chain of the full module test.

7.2.2 Test environment

After assembly at KIT, the module was brought to the STS detector laboratory at GSI for module characterization. The readout chain used in the full module test consists of three main components: the FEBs on the module, the C-ROB providing data aggregation and the electrical-to-optical interface, and the DPB (see fig. 7.8). The C-ROB is connected to the FEBs via two flat data cables, interfaced with a ZIF to FMC connector on the C-ROB. It is powered with 7 V via a pair of twisted cables. Optical fibers connect the C-ROB to the DPB, which is based on the AFCK board, hosted inside a µTCA crate. The module is installed inside a light-tight aluminium box which provides shielding against electromagnetic interference, as shown in fig. 7.9. The FEBs-8 are mounted with the help of thermally conducting pads onto the cooling fins, oriented perpendicular to the sensor plane, simulating the actual STS environment. The FEBs are water-cooled to 15 °C. Additionally, the box integrates a holder that allows accurate positioning of a radioactive source above the sensor in order to perform position sensitive signal studies.

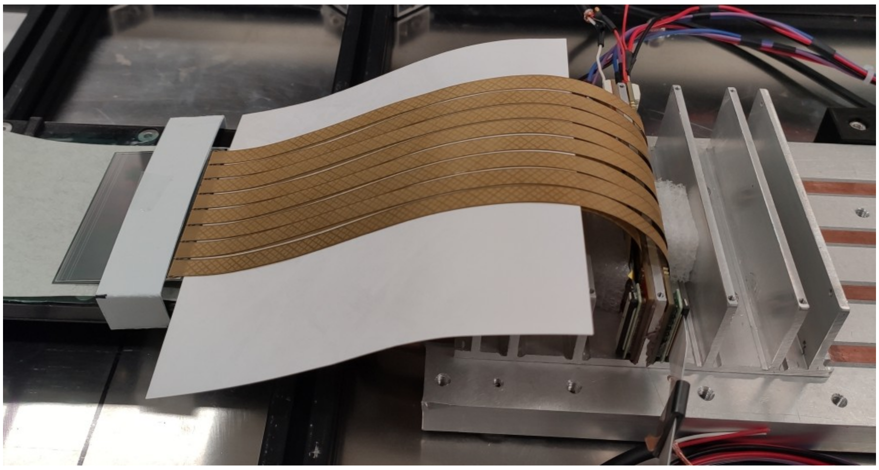

Figure 7.9: Copper module without microcable shielding installed inside the module test box.

7.2.3 Module Performance evaluation

Based on the ENC parametrization used before we expect the following ENC levels for the module Cu_KIT_202, comprising a 62 mm × 22 mm CiS sensor and 20 cm copper microcables

$$ENC_{tot,e} = 350\,\mathrm{e}^- + \left(0.38\,\frac{\mathrm{pF}}{\mathrm{cm}} \cdot 20\,\mathrm{cm} + 1.52\,\frac{\mathrm{pF}}{\mathrm{cm}} \cdot 2.2\,\mathrm{cm}\right) \cdot 28.7\,\mathrm{e}^-/\mathrm{pF} = 664\,\mathrm{e}^- , \tag{7.1}$$

$$ENC_{tot,h} = 350\,\mathrm{e}^- + \left(0.38\,\frac{\mathrm{pF}}{\mathrm{cm}} \cdot 20\,\mathrm{cm} + 1.24\,\frac{\mathrm{pF}}{\mathrm{cm}} \cdot 2.2\,\mathrm{cm}\right) \cdot 28.7\,\mathrm{e}^-/\mathrm{pF} = 646\,\mathrm{e}^- . \tag{7.2}$$

Figure 7.10 shows the measured ENC levels of all channels on the p– and n-side, measured at a symmetric bias voltage of 150 V. ASICs 1 and 7 of the p-side are non-functional due to problems in wire bonding. Channels without a proper analog response are set to zero. This can be due to no response at all or such high noise levels that a fit is not feasible. Neglecting the z-strips on the-pside, as well as dead and overly noisy channels, the average ENC levels on the n– and p-side are is measured noise levels are 670 e^- and 590 e^-, respectively. The 62 mm × 22 mm sensor has a total of 42 z-strips on the p-side, which are connected via the second metalization layer to form full-length strips. The additional capacitance introduced by the second metalization layer almost doubles the noise level of channels 0–41. Also shown in Figure 7.10 are the expected ENC levels based on the parametrization in eq. (7.1). This helps in the identification of unconnected channels, be it on the sensor side or the ASIC side. It can be observed that the majority of unconnected channels (48 out of 70) is located on ASICs 4 and 6 on the p-side. They are found to be clustered on the lower end of channels, respectively, indicating a slight tilt between microcable and ASIC, or insufficient solder deposition on this end of the cable. Table 7.2 summarizes channels that do not behave as expected, including dead, overly noisy, and unconnected channels. The calculated channel yields are 92.1 % and 97.4 % for the p– and n-side, respectively, resulting in an overall channel yield of 95.1 % for the module Cu_KIT_202. Figure 7.11a shows the ADC threshold distribution at calibration

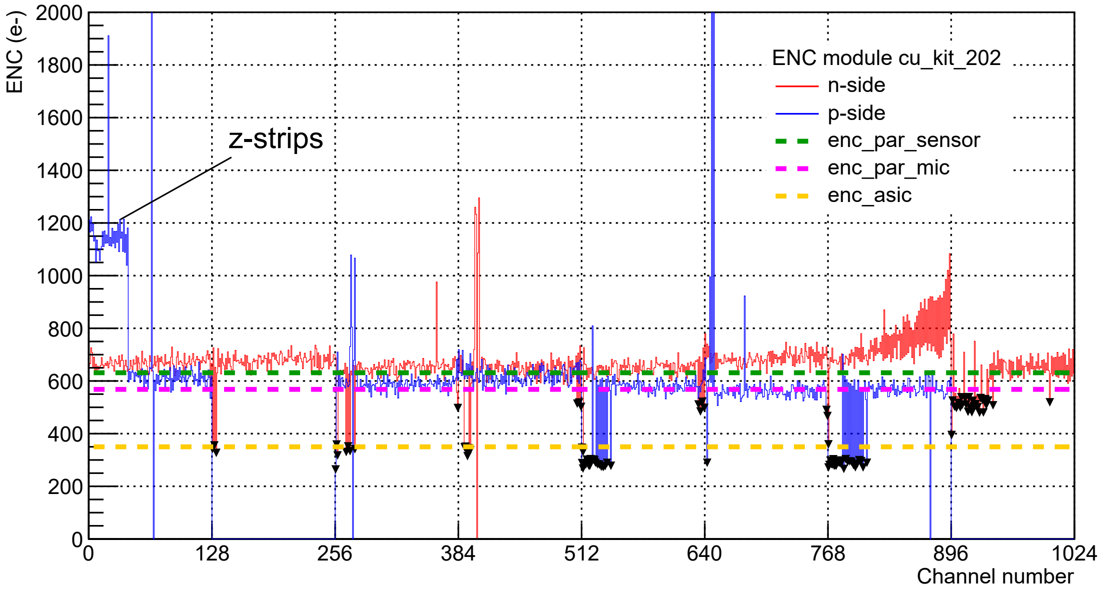

Figure 7.10: ENC as a function of channel number of the copper module Cu_KIT_202. ASICs 1 and 7 on the p-side are non-functional. The z-strips, which are interconnected via the second metalization layer, are indicated.

Table 7.2: Summary of conspicious channels of the full-scale copper prototype module Cu_KIT_202. The yield is a conservative estimation, including the presumably functional noisy channels.

	Dead	Noisy	Disconnected	Sum	Channel yield (%)
p-side	3	8	50	61	92.1
n-side	1	6	20	27	97.4
Total	4	14	70	88	95.1

value ($v_{ref,t}$ = 58) for both signal polarities. The difference in threshold between the n− and p-side is less than 1 %. Gaussian fits to the distributions yield a relative spread of 2.0 % and 1.9 % for n− and p-side, respectively. The ADC gain distributions (see Figure 7.11b) reveal great uniformity with a gain of 0.112 ± 0.002 fC/LSB and 0.112 ± 0.001 fC/LSB for the n− and p-side, respectively. After having assured good module performance with the help of the ENC measurements, a symmetric bias voltage scan was performed between 40 V to 350 V for ASICs 2 and 3 of the p-side and ASICs 4 and 5 of the n-side. In the installed module, those ASICs are located directly opposite of each other (see Figure 7.6). The ENC-bias voltage curve for all four ASICs is presented in Figure 7.12. The data points represent the ENC averaged over all channels of the ASIC while the error bars indicate the channel spread. The sensor depletion is beautifully reconstructed on the n-side channels. When increasing the reverse bias voltage, starting from 0 V, the depletion zone expands from the p-side towards the n-side. At the lowest data point at 40 V, the region surrounding the p-side implants is already depleted,

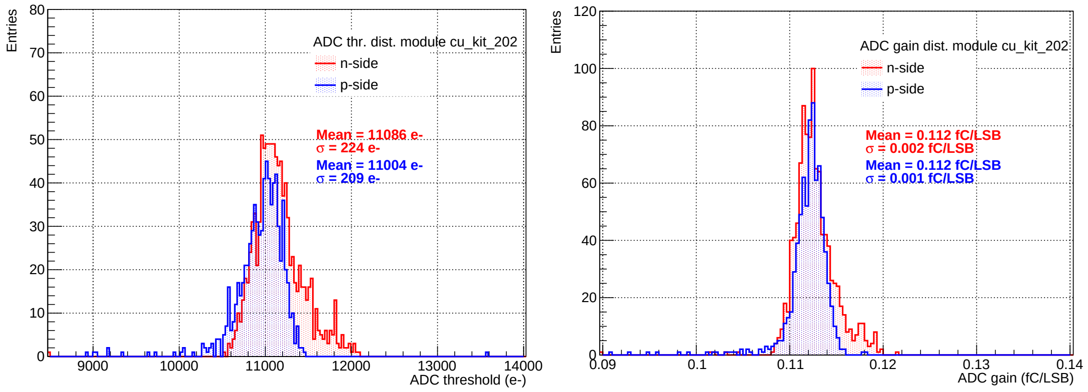

(a) ADC threshold distribution at calibration value.

(b) ADC gain distribution.

Figure 7.11: ADC threshold and ADC gain distribution over all channels of the module Cu_KIT_202.

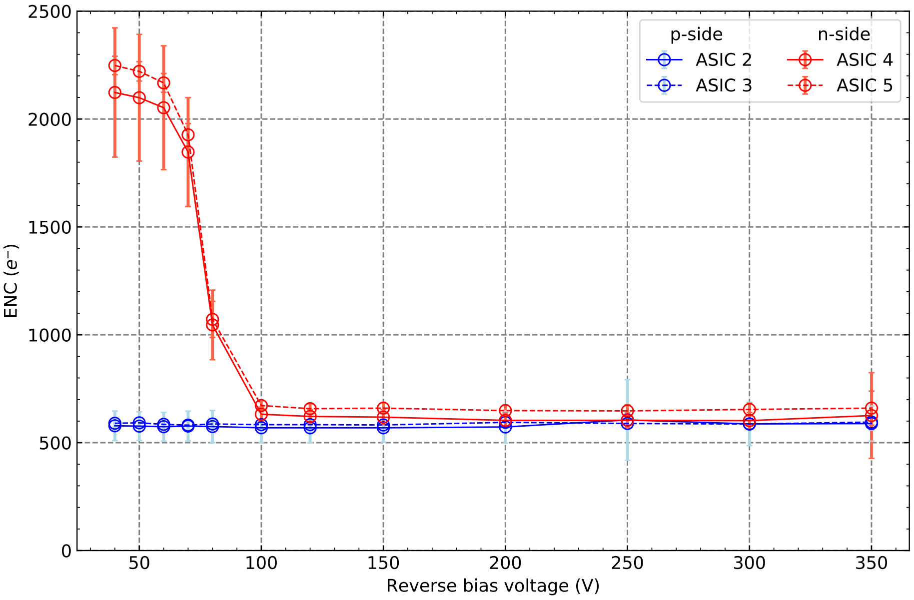

Figure 7.12: ENC–bias voltage characteristics shown for four selected ASICs of the copper module Cu_KIT_202, two ASICs per sensor-side.

hence the ENC values stay completely flat on the p-side. Looking at the n-side curve, full depletion appears to be reached in between 80 V to 100 V, in agreement with expectations.

7.2.4 Signal measurements with a radioactive ^{241}Am-source

In order to determine the absolute value of the signal size that allows us to calculate the SNR and the charge collection efficiency (CCE) of the copper module, measurements with an ^{241}Am

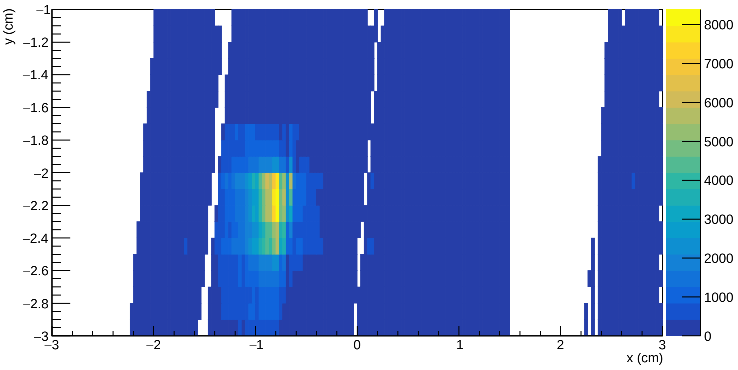

Figure 7.13: 2D map of the reconstructed hits from the ^{241}Am-source. The color code indicates the hits per bin.

α-source with an activity of 37 MBq have been performed. In addition to the α-particles, ^{241}Am emits characteristic X-rays with well-defined energies. The most intense peak in the γ-ray spectrum of ^{241}Am is located at 59.54 keV, with additional lower-intensity peaks at 13.9, 17.8, and 26.4 keV [125]. The source measurements are performed with the module mounted inside the previously shown test box (Figure 7.9), which allows accurate positioning of the source above the sensor in order to perform position-sensitive signal studies. Measurements with the ^{241}Am-source have been conducted at various ADC threshold levels of $v_{\text{ref,t}} = 48$ up to $v_{\text{ref,t}} = 52$. The available ^{241}Am-source is non-collimated and has a cylindrical shape with a radius $r \sim 1$ mm and a height $h \sim 9$ mm. It can be placed inside the test box directly above the sensor, or outside of the test box above a window made out of thin aluminium foil. In the former arrangement, the source must be placed flat to fit inside the box. The reconstructed hit map of a measurement run at $v_{\text{ref,t}} = 50$ with the source placed flat directly above the sensor is shown in Figure 7.13. The rectangular cross section of the source is well visible. Figure 7.14 shows the digi rate normalized to timeslices as a function of channel number for the same source run compared to a background run. The source spot is well reconstructed on both the p− and n-side with signal rates several orders of magnitude above the noise rates. The measured energy spectrum of the ^{241}Am-source is shown in Figure 7.15 for ASIC 13 (n-side) for threshold values of $v_{\text{ref,t}} = 52$, 50, and 48. The 59.54 keV γ-peak is well reconstructed. Since the ADC measures the signal above threshold, the peak position moves to larger values with decreasing threshold. Due to increasing noise pick-up, the peak broadens slightly towards lower threshold values. The shape of the γ-peak can be closely approximated by a Gaussian function sitting on a linear background [126]. A Gaussian fit to the measured spectra results in peak positions of 11.50, 13.40, and 15.65 ADC units, respectively. A linear fit to the peak positions as a function of $\text{v}_{\text{ref,t}}$ yields a slope of -1.01 ADC/$\text{v}_{\text{ref,t}}$. If we multiply this result with the gain of the ADC (0.112 fC/ADC), this transforms into 706 e^- per $\text{v}_{\text{ref,t}}$ unit. In order to verify the relation between charge and $\text{v}_{\text{ref,t}}$ units, two reference noise scans have been performed at $v_{\text{ref,t}} = 58$ and $v_{\text{ref,t}} = 52$. The ADC thresholds in those scans were found to be 11 045 e^- and 6966 e^-, respectively. A linear fit yields a slope of 680 $e^-/\text{v}_{\text{ref,t}}$, in good agreement

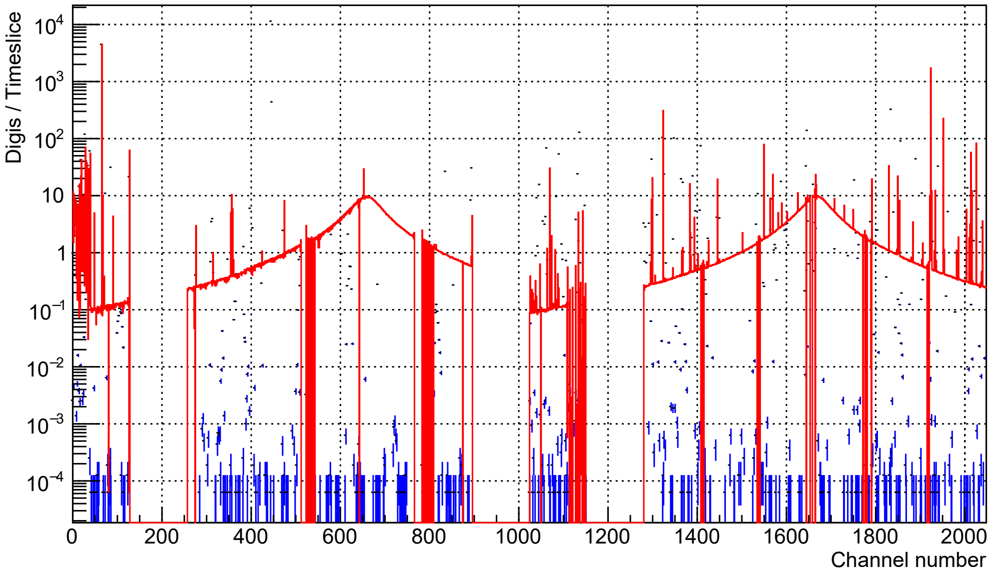

Figure 7.14: Distribution of digis normalized to timeslices as a function of channel number. The red curve shows a measurement with the ^{241}Am-source placed over the sensor, while the blue curve represents a background measurement. Channels 0–1023 correspond to the p-side and channels 1024–2047 to the n-side.

with the value extracted from the spectra. Extrapolating the threshold to lower values yields thresholds of 5606 e^- and 4246 e^- for $v_{\mathrm{ref,t}} = 50$ and 48, respectively.

In order to determine the SNR and the CCE, the meausurement of the 59.54 keV-peak must be converted from ADC units to charge. This requires precise knowledge of the ASIC calibration. The transfer function from ADC units to charge is

$$Q_m\,[\mathrm{e}^-] = 6241 \left[\frac{\mathrm{e}^-}{\mathrm{fC}}\right] \cdot \mathrm{Gain}\left[\frac{\mathrm{fC}}{\mathrm{ADC}}\right] \cdot (\mathrm{Peak}\,[\mathrm{ADC}] - 1) + \mathrm{Threshold}\,[\mathrm{e}^-]\,. \tag{7.3}$$

With the help of the transfer function (eq. (7.3) on page 107), the peak values can be expressed in electrons. The average signal of the three measurements shown in Figure 7.15 is 14 640 e^-. Finally, the SNR can be calculated

$$SNR = \frac{Q_m}{ENC} = \frac{14\,640\,\mathrm{e}^-}{670\,\mathrm{e}^-} \simeq 22\,.$$

With the knowledge of the signal charge, the CCE can be estimated. The expected charge created by the 59.54 keV-peak of the ^{241}Am-source is 59 540 eV/3.62 eV = 16 450 e^-. However, the measured charge will be lower than the created one because the input capacitance of the electronics is not infinitely large with respect to the detector capacitance C_d. The ratio of

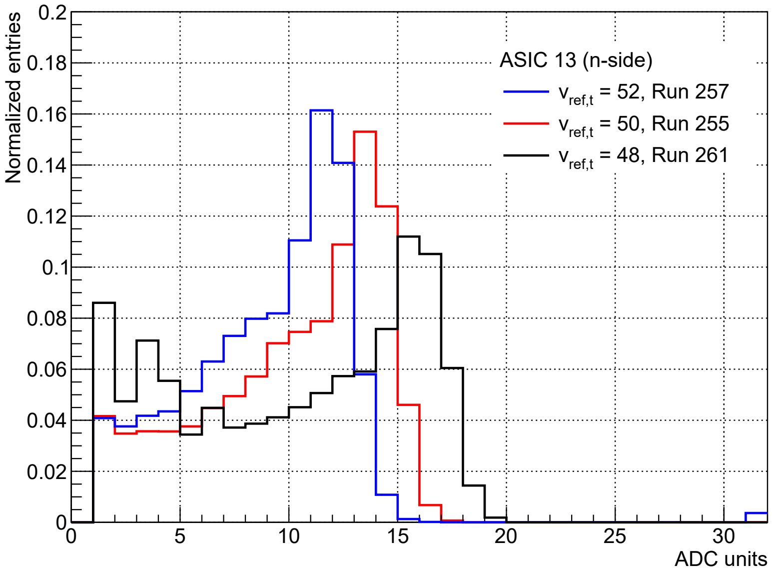

Figure 7.15: Measured energy spectrum of the ^{241}Am-source as a function of ADC units for ASIC 13 (n-side) for threshold values of $v_{\mathrm{ref,t}} = 52$, 50, and 48, corresponding to 6970, 5600, and 4250 e$^-$, respectively. The 59.54 keV γ-peak is well reconstructed.

charge arriving at the CSA input to the created charge is

$$Q_i/Q_s = \frac{1}{1+\frac{C_d}{C_i}}\,. \tag{7.4}$$

The detector capacitance C_d is given by the sum of the capacitance of the sensor and the microcable, which for module Cu_KIT_202 is $C_d = C_{mc} + C_s = 10.94\,\mathrm{pF}$. The dynamic input capacitance can be estimated using the open-loop–gain relationship, $C_i = A \cdot C_f$, where $A = 4.8\,\mathrm{kV\,V^{-1}}$ and $C_f = 100\,\mathrm{fF}$ for operation of the STS-XYTER in the STS mode. Inserting the values into eq. (7.4) on page 108 yields $Q_i/Q_s = 0.978$. The expected charge after performing the correction is 16 080 e$^-$. Finally, the ratio Q_m/Q_i represents the actual CCE, which in this particular case is 91 %. This result should be taken with some caution because the measurements lack statistics and certain behaviors of the ASICs, such as the differences in ADC gain and threshold between ASICs, are not fully understood. Still, this estimation gives confidence that STS modules based on the copper technology can achieve a good performance in SNR and CCE.

7.3 Comparison of aluminium and copper module technologies

Unfortunately, a direct, quantitative comparison of noise levels between the copper module Cu_KIT_202 and a module built with aluminium microcables is not possible, because the combination of microcable length and sensor size used in module Cu_KIT_202 does not exist in the final STS detector. However, comparing the measured noise levels with the expected ones for non-irradiated modules in both technologies, respectively, reveals a consistent picture. In both technologies, the measured noise levels are very close to the expected ones. It can be concluded that with regard to the noise behavior, the slightly increased capacitance of the copper microcable clearly is no showstopper.

Next to the noise, another essential parameter for good module performance is the overall channel yield. Too many broken channels negatively influence the spatial resolution, and thus momentum resolution of the detector. The aim is to have less than 1.5 % of broken channels [127]. At this stage, after many years of development, this benchmark is typically achieved by the aluminium modules. Considering the fact that it is the first functional copper module, the yield above 95 % for the module Cu_KIT_202 is a great achievement. With more experience, it should be possible to push this metric beyond 98.5 %.

It was never intended to build the whole STS from copper modules. It was, however, considered to have a mixed solution of copper and aluminium modules in the case of insufficient throughput of aluminium microcables for series production. In this scenario, the copper modules are best suited as the outermost modules on the ladders. If placed on the periphery, the copper microcables do not cross a single sensor on the ladder. Hence, the slightly higher material budget of the copper microcables does not notably affect the STS performance. Since there are 106 ladders employed in the STS, a total of $212/876 \simeq 24.2\,\%$ of the modules could be built in the copper technology in this way. Moreover, if placed only on the periphery, the higher thickness and stiffness of the copper microcables should not cause any complications during detector integration.

In the meantime, the manufacturing capabilities of the aluminium microcables at LTU Ltd. have advanced as well, and a sufficient throughput of high-quality microcables seems secured. Therefore, and because of the more advanced and refined stage of development, the STS team opts for building the full detector with modules in the aluminium technology.

8 Analysis of STS Detector Module in 2.7 GeV/c Proton Beam

It is of great importance to test the STS detector modules in a scenario resembling the final CBM environment as close as possible. Therefore, a subsample of the individual detectors of CBM are exposed to the products of a HIC in the mini CBM (mCBM) beam campaign at GSI. In mCBM, the STS detector is exposed to a particle shower comprising a multitude of particle species over a wide range of energies. This makes it highly difficult to pinpoint issues in the electronic readout or in the software reconstruction.

Therefore, specific detector investigations took place in test beam, using a simpler and cleaner environment. The STS team scheduled a beamtime at the Cooling Synchrotron (COSY) at the research center Jülich, Germany, in November 2019. COSY provided a pencil-like monochromatic beam of 2.7 GeV/c protons. Compared to mCBM, the identification of issues in the setup is facilitated considerably. Moreover, the COSY beamtime enabled a first-time evaluation of the full analysis software chain with real data and the evaluation of the full electronic readout chain of STS.

In the following, the experimental setup of the COSY beamtime is described in more detail. The noise behavior of the installed module is discussed before going into the details of the beamtime. The estimation of frontend time resolution is given before discussing the detector performance, including hit maps, cluster charge distributions, residuals, and hit detection efficiency.

8.1 COSY beamtime experimental setup

The experimental setup in the JESSICA cave at COSY is shown in Figure 8.1. It comprises one complete STS detector module placed inside the big aluminium shielding box in the middle of the image and two reference hodoscopes, one in front and one behind the STS. Both hodoscopes have 128 channels, 64 channels each in x− and y-direction with a position resolution of approximately 1 mm.

The interior of the STS module box is shown in Figure 8.2. It hosts a quarter C-frame functioning as a mechanical support structure, cooling infrastructure, the STS module mounted on a carbon support ladder, the C-ROB [128], and the power board. The FEBs are water-cooled to 16 °C with a Lauda Eco Gold laboratory thermostat.

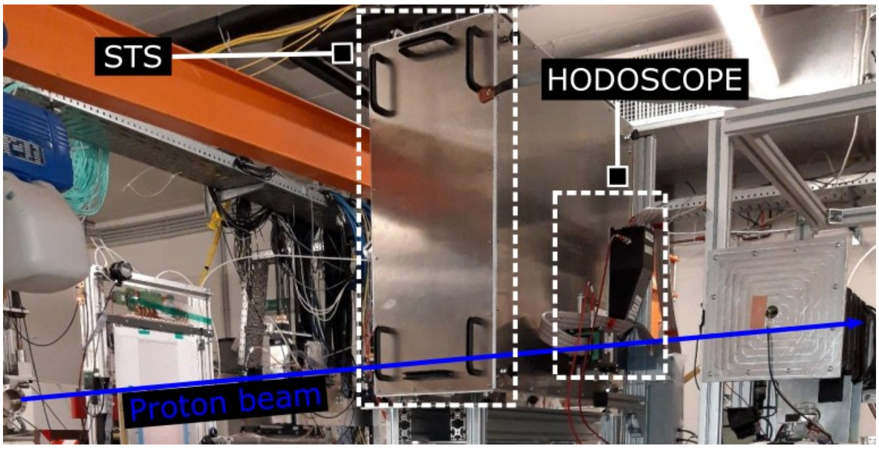

Figure 8.1: The experimental setup at the COSY beamtime in November 2019. The beam enters from the beam pipe in the bottom left. It passes a dosimetry foil, the first hodoscope, the STS module, and the second hodoscope. The front hodoscope is covered by the STS box.

The detector module installed at COSY consists of a 6.2 cm × 6.2 cm Hamamatsu sensor connected to 16 STS-XYTER2.1 readout ASICs via 45 cm long aluminium microcables. Two FEB-8—one for the p-side, one for the n-side—each host eight STS-XYTER2.1. The module has a wide shielding covering the sensor on both sides and no cutouts for the L-legs attaching the silicon to the carbon frame.

8.2 Evaluation of system noise

For a correct reconstruction of hits and tracks, a low noise level is essential. Neglecting the leakage current, the expected ENC for the COSY module related to the total capacitance can be parametrized as:

$$ENC = \underbrace{350\,\mathrm{e}^-}_{\text{ASIC}} + \left(\underbrace{0.35\,\frac{\mathrm{pF}}{\mathrm{cm}} \cdot 49\,\mathrm{cm}}_{\text{Microcable}} + \underbrace{1\,\frac{\mathrm{pF}}{\mathrm{cm}} \cdot 6.2\,\mathrm{cm}}_{\text{Sensor}} \right) \cdot 28.7\,\mathrm{e}^-/\mathrm{pF} = 1020\,\mathrm{e}^- \,. \tag{8.1}$$

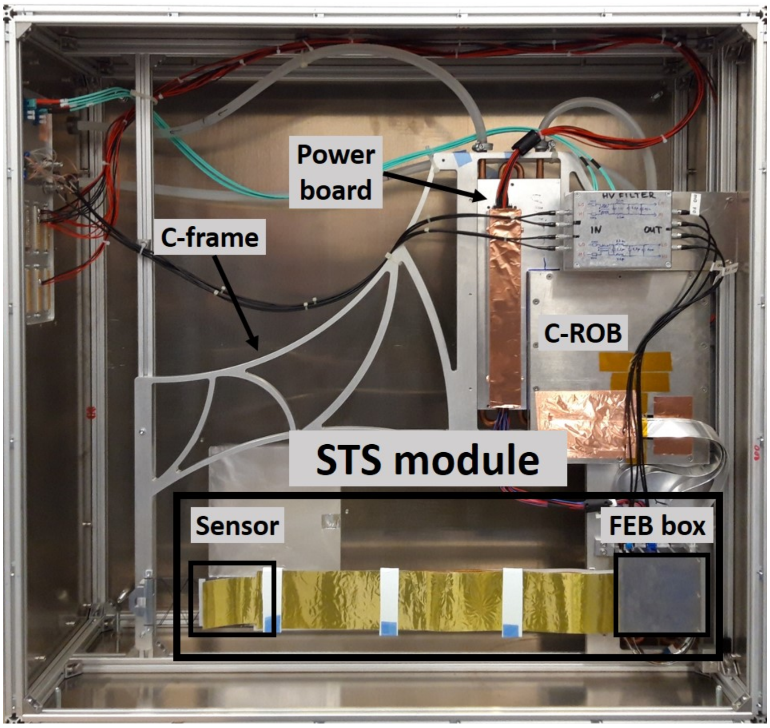

Figure 8.2: Interior of the STS module box used in the COSY beamtime.

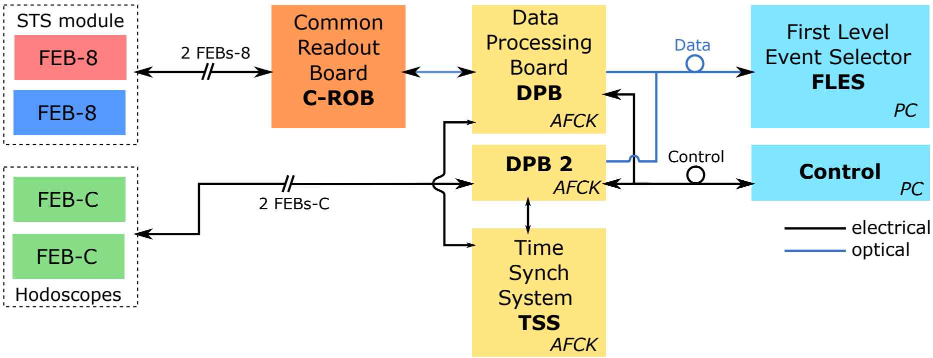

Figure 8.3: Readout chain of the COSY 2019 beamtime.

Hence, the target noise level for the beamtime was around 1000 e⁻. Figure 8.4 shows the measured ENC for all channels of the COSY module [113]. The increased ENC levels observed in the first 134 channels of the p-side correspond to the double-metal Z-strips that have a higher capacitance. The obtained noise levels are 1054 e⁻/1102 e⁻ for the n–/p-side. This is by far the best noise level that has been achieved so far for for STS in a full system with double-sided readout.

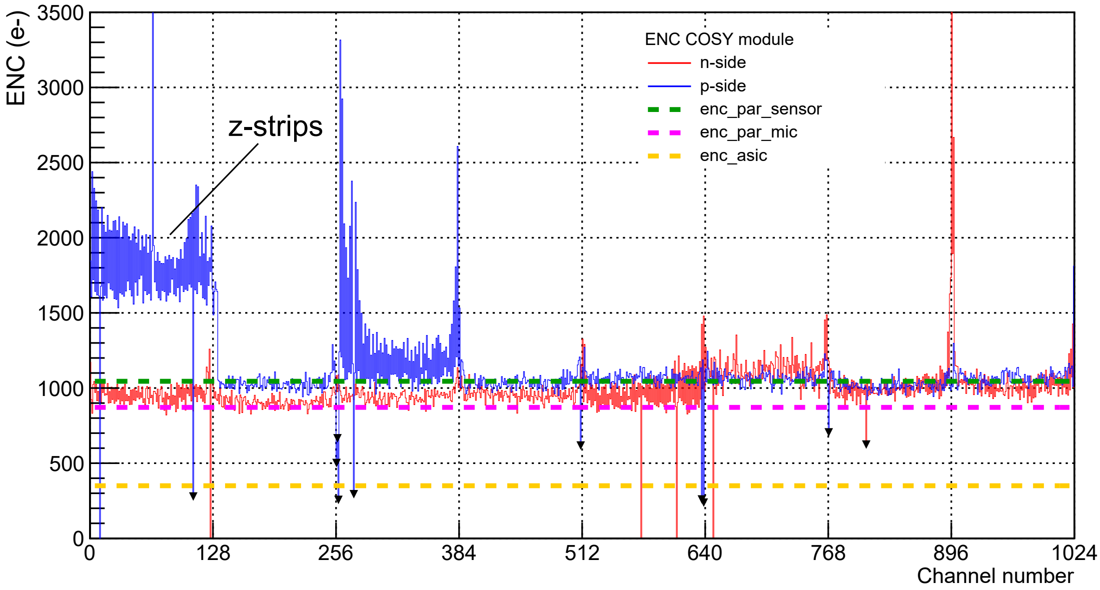

Figure 8.4: Overall noise level for all channels of the COSY module.

8.3 Analysis reconstruction chain

In order to understand the following sections, it is mandatory to introduce some specific nomenclature about the CBMRoot environment and the accompanying analysis and reconstruction chain. Figure 8.5 shows a basic block diagram of the individual data abstraction levels (data containers). The raw data is stored in multiple **.tsa** files per run. If a signal crosses the lowest discriminator threshold of the slow path, it will be digitized and processed further. The 5-bit amplitude, the 14-bit timestamp, the address (HODO A, STS p-side, STS n-side, or HODO B), and the channel number are stored as a so-called **digi**. All of this is done by the unpacker. Next, the CBM cluster finder algorithm combines digis with the same address in neighboring channels in a given time window into a **cluster**. To find the cluster position, first the amplitude is summed for all the digis in the cluster, then the center of gravity of the cluster is calculated by weighting the digis with their amplitude. Following the cluster finder, the CBM Hit Finder algorithm combines clusters from the p– and n-side of the sensor to a **hit**, if the position and time of the clusters match. Additionally, a threshold might be applied.

8.4 COSY proton beam characterization

The COSY accelerator provided a monochromatic, pencil-like proton beam with a momentum of 2.7 GeV/c. Figure 8.6 shows the spill structure of the beam. The rate of digis is plotted over time for all three systems for 10 min of runtime. One spill period is 80 s, including a 10 s off-spill period. The rate on the n-side of the STS is slightly lower than on the p-side because the lowest 20 discriminators of the ADC of ASIC 5 on the n-side were not firing. The

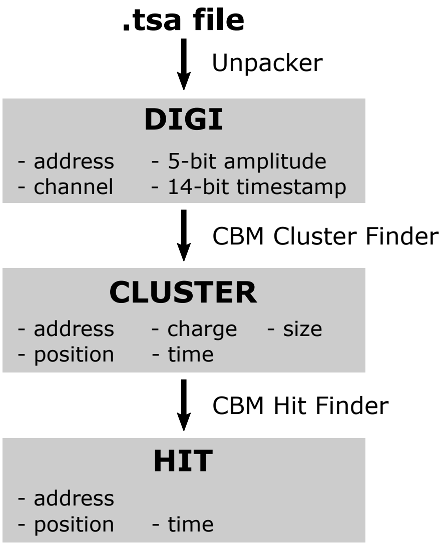

Figure 8.5: Basic CBMRoot analysis and reconstruction chain with the basic data containers: digis, clusters, and hits.

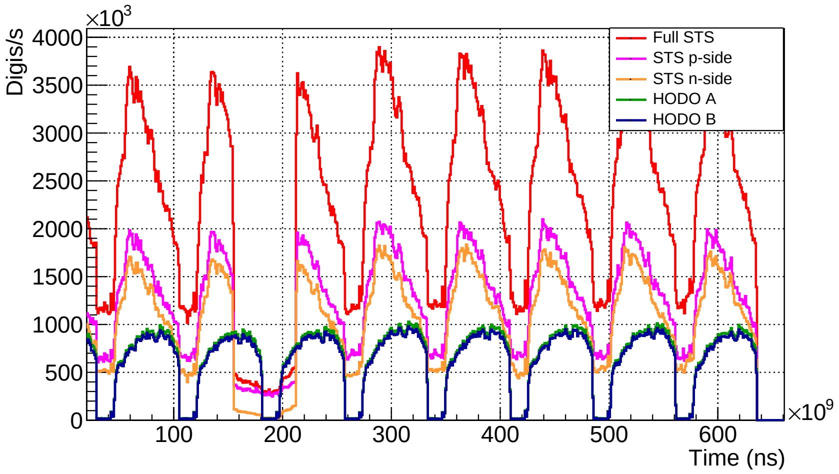

Figure 8.6: Spill structure of the COSY proton beam expressed by the digi rate over time for all three systems. Between 160 s and 220 s, the STS experienced data loss.

hodoscopes are operated in MUCH readout mode with a higher threshold, and thus collect less noise. The maximum hit rate is around 4 Mhits/s with an average rate of 250 khits/s. The size of the beam spot can be extracted from the hit distribution in the hodoscopes.

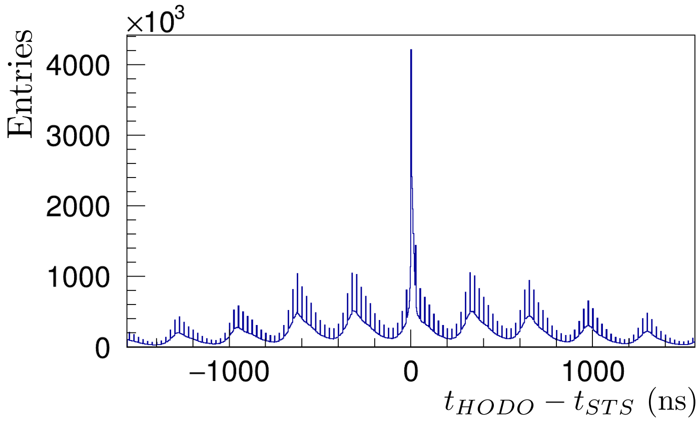

Figure 8.7: Digi rate as a function of time difference between the STS and the hodoscopes. The sharp peak reveals the time offset between the systems.

8.5 Correction of time offset jumps

Precise timing information of the hits in the hodoscopes and the STS is necessary to establish correct time correlations between the systems, which are necessary to determine the hit detection efficiency. In order to achieve the correct time calibration, one must first identify the time offset between the STS and hodoscopes. Figure 8.7 shows the digi rate over the time difference between the systems. It reveals a sharp peak—indicating the time offset between the STS and the hodoscopes—sitting on a complex background. The wave-like structure with a time period of around 300 ns originates from the COSY bunch structure. Additionally, sharp peaks are visible with a frequency of 40 MHz, presumably noise picked up by the microcables.

During the first stage of data analysis, jumps in the time offset between the hodoscopes and STS have been observed inside all of the runs, caused by a sudden change in time synchronization. Further analysis revealed that the jumps appear only in multiples of 800 ns which is one of the clock periods on the Data Processing Boards (DPB). There are two DPBs in the COSY readout chain (Figure 8.3), one for the hodoscopes and one for the STS data. The ASIC generates a 14-bit timestamp. On the DPB this timestamp is merged into a 32-bit timestamp for the digis. Out of the 32 bits, the lowest eight bit correspond to exactly 800 ns. It was found later that the time offset jumps indeed could be attributed to the sorting buffer and algorithm in the C-ROB firmware. Therefore, the problem is not originating at the ASIC level, but further downstream. The time jumps had never been observed in the more complex mCBM data, but they were observed on the following beam time. The findings of the COSY beamtime now allow for an offline correction of the mCBM data. No jumps in time offset have been observed between the hodoscopes.

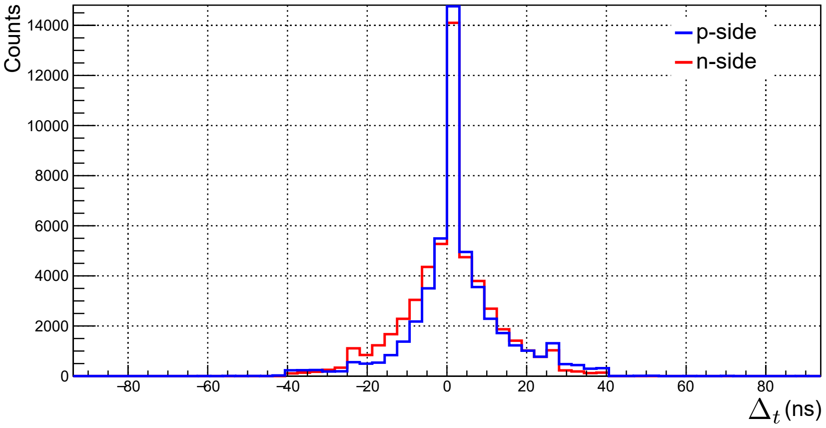

Figure 8.8: Time difference between digis in two-strip clusters for the n− and p-side.

In the meantime, the sorting algorithm has been fixed and no more time jumps have occurred ever since. Regarding the analysis of the COSY beamtime, the time jumps can be corrected for manually, as they can be easily identified.

8.6 Estimation of frontend time resolution

The total time resolution of the ASIC can be expressed by three uncorrelated uncertainties

$$\sigma_t^2 = \underbrace{\left(\frac{TS_{bin}}{\sqrt{12}}\right)^2}_{\text{timestamp}} + \underbrace{\left(\frac{\sigma_n}{\frac{dV}{dt}|V_{thr}}\right)^2}_{\text{jitter}} + \underbrace{\left(\frac{V_{thr}}{\frac{dV}{dt}}\right)^2}_{\text{time-walk}}, \tag{8.2}$$

where $TS_{bin} = 3.125\,\text{ns}$ is the width of one LSB of the fast discriminator, σ_n the noise level, V_{thr} the threshold of the fast discriminator, and dV/dt the slope of the leading edge. More details about the timing in the STS-XYTER ASIC can be found in [112].

Figure 8.8 shows histograms of the time difference in 2-strip cluster signals, separately for the p− and the n-side. The bin size of 3.125 ns corresponds to the size of one LSB of the ASIC timestamp. Considering that walk correction to the signal time has not yet been applied, the plot demonstrates an excellent time resolution of a few ns. Another way to estimate the time resolution is to plot the distribution of the time difference between hits in the STS and the best coincident hits in the hodoscopes, as shown in Figure 8.9. The Gaussian fit reveals $\sigma = 6.9\,\text{ns}$—an excellent upper limit on the time resolution given that here the time resolution of the hodoscopes is folded in as well. If we assume that the time resolution of the scintillating fiber hodoscopes is limited by the electronics, it should be comparable to the STS time resolution. Then, the resolution of the STS is $6.9\,\text{ns}/\sqrt{2} \sim 4.9\,\text{ns}$. Note that this result is before time-walk correction.

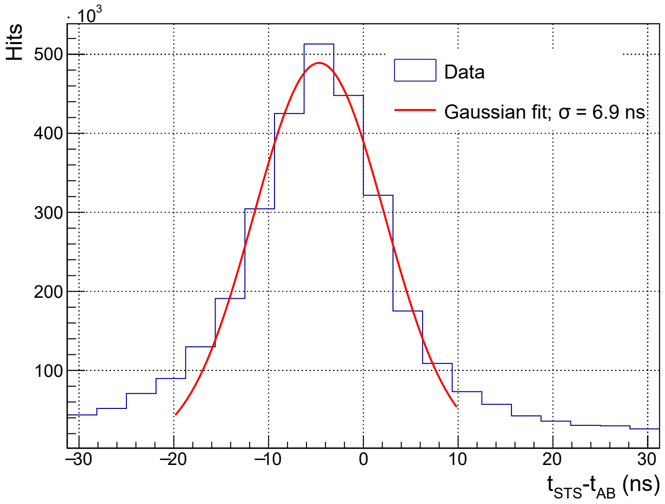

Figure 8.9: Time difference between hits in the STS and the best coincident hits in the hodoscopes.

8.7 Detector performance analysis

In this section, the performance of the detector module installed in the COSY beamtime is evaluated. First, the 3D hit map is reconstructed by establishing the best coincidence between the systems based on time information. Based on the the correlation of the best time coincident hits, the spatial resolution of the system as a whole is estimated. The position of the proton peak in ADC units is extracted from cluster charge distributions. Finally, the charge spectra are translated from ADC units into actual charge, which allows to estimate the SNR and CCE of the module.

8.7.1 Coincidence between the STS and hodoscopes

One of the primary tasks of the COSY data analysis was to reconstruct the beam spot in all three systems. During the beamtime, the STS sensor was shifted with respect to the hodoscopes. In order to understand the performance of the STS sensor, the coincidence with the hodoscope system has been studied, performing the following steps:

1. Correlate X and Y hit positions in HODO A and HODO B independently.
2. Find the best coincidence based on time information to reduce background.
3. Extrapolate the 2D hit coordinates of the hodoscopes in a straight track to the STS module.
4. Correlate X and Y hit positions in STS and the extrapolated HODO positions independently.
5. Find the best coincidence based on time information to reduce background.
6. Plot $\Delta X_{STS-HODO_{extr}}$ versus $\Delta Y_{STS-HODO_{extr}}$.

The described procedure is visualized in Figures 8.10 to 8.11 on pages 120–121. The top panel shows all possible combinations of hits between the hodoscopes separately for x and y. If one only correlates the hits with corresponding time information, one arrives at Figures 8.10c to 8.10d. Now, these best coincident hits are extrapolated to the STS plane by connecting them with a straight track. All possible combinations of hits of these extrapolated hits to the hits recorded in the STS are shown in Figures 8.10e to 8.10f. Regarding again only the hits with corresponding time information, one arrives at Figures 8.10g to 8.10h. The correlation between the STS and the exptrapolated hodoscope hits is also shown as a 2D map in Figure 8.11, before and after applying the time-based cut. Having established the best coincidence between the systems, the 3D hit map can be reconstructed. It is shown in Figure 8.12.

8.7.2 Residuals

From the coincidence of the STS with the hodoscope system, residuals in X and Y can be extracted. If one projects the 2D coincidence between the STS and the hodoscope systems separately in X and Y (Figure 8.11), a sharp peak is visible on top of a broad background, see Figure 8.13. A Gaussian fit gives the resolution in X (670 µm) and Y (233 µm). The resolution in Y is better than in X because the sensor was rotated by 90° during the beamtime. It is however important to note that the precision of the extrapolated signal is significantly lower than that of the sensor, as it is dominated by the hodoscope fiber resolution.

8.7.3 Cluster charge distributions

The relativistic kinetic energy of a particle is

$$E_{kin} = E - E_0 = \sqrt{p^2c^2 + m^2c^4} - mc^2\,. \tag{8.3}$$

COSY provided a monochromatic beam of protons ($m_p = 938.27\,\mathrm{GeV/c^2}$) with a momentum of $p = 2.7\,\mathrm{GeV/c}$, equivalent to a kinetic energy of $E_{kin} = 1.92\,\mathrm{GeV}$. The velocity of the protons is

$$v = c \cdot \sqrt{1 - \frac{1}{(E_{kin}/m_pc^2 + 1)^2}}\,, \tag{8.4}$$

which amounts to 0.9446 c.

The energy loss of fast, charged, and heavy particles during the passage of matter due to excitation and ionization is calculated with the Bethe formula (see eq. (2.15) on page 23). For protons with $\beta = 0.9446$ passing through silicon, the mean energy loss per path length, or linear stopping power, is $3.97\,\mathrm{MeV\,cm^{-1}}$. The most probable energy loss typically is a factor of 0.7 lower [129]. The average number of created e–h pairs in a Si sensor with a thickness of 320 µm is

$$\frac{dE}{dx} \cdot \frac{d}{I_0} = 3.97\,\frac{\mathrm{MeV}}{\mathrm{cm}} \cdot \frac{0.032\,\mathrm{cm}}{3.62\,\mathrm{eV}} = 35\,094\,, \tag{8.5}$$

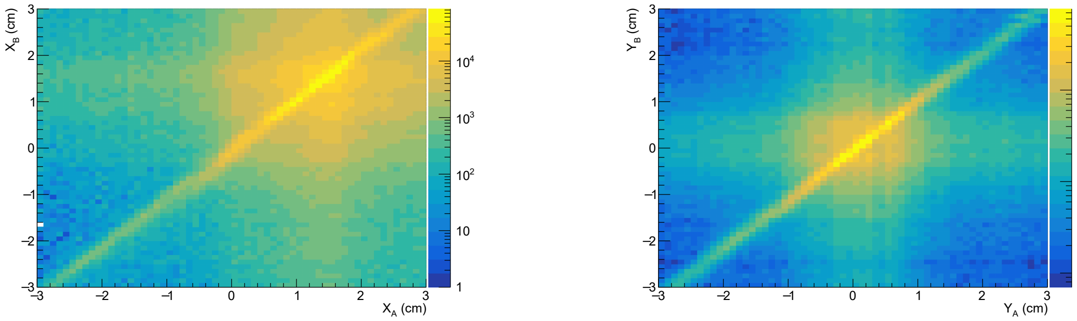

(a) HODO A–HODO B, X.

(b) HODO A–HODO B, Y.

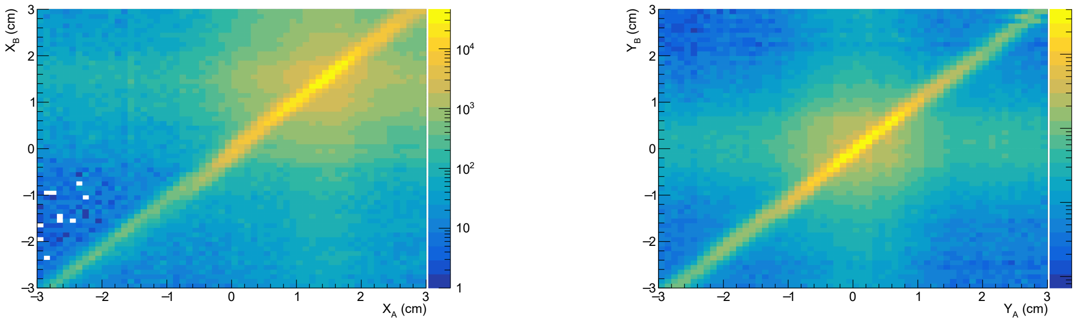

(c) Best coincidence HODO A–HODO B, X.

(d) Best coincidence HODO A–HODO B, Y.

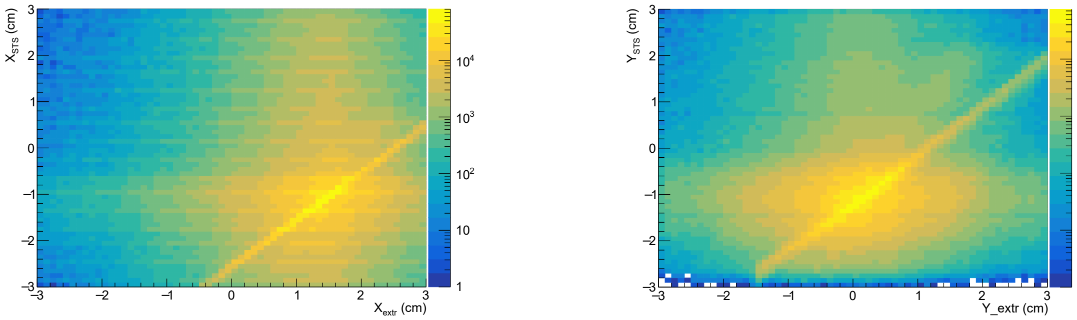

(e) STS–HODO extrapolated, X.

(f) STS–HODO extrapolated, Y.

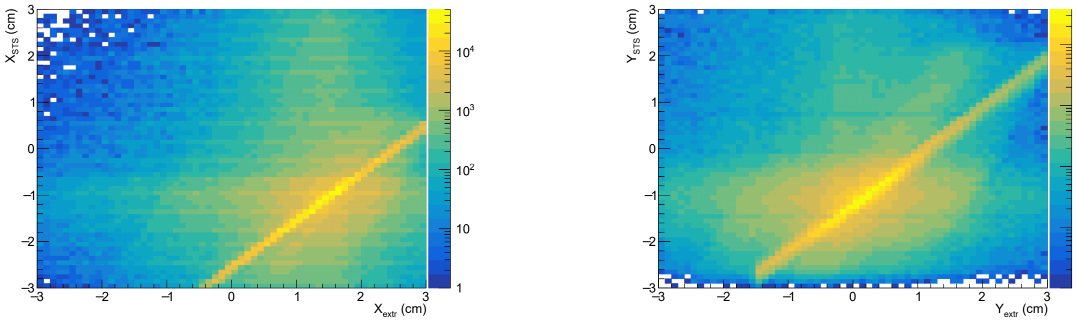

(g) Best coincidence STS–HODO extrapolated, X.

(h) Best coincidence STS–HODO extrapolated, Y.

Figure 8.10: Correlations between both the hodoscopes and the hodoscopes and the STS in X (left column) and Y (right column). The color code indicates the number of hits per bin. Note the log-scale.

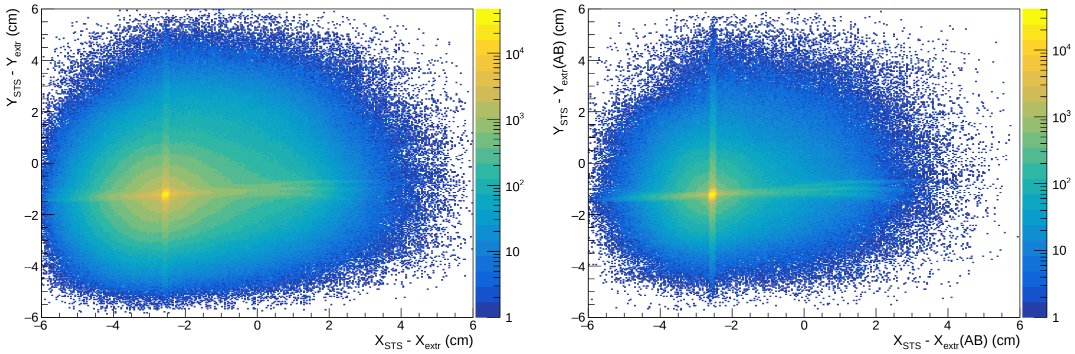

Figure 8.11: 2D correlation between STS and extrapolated hodoscope hits before and after time-based correction.

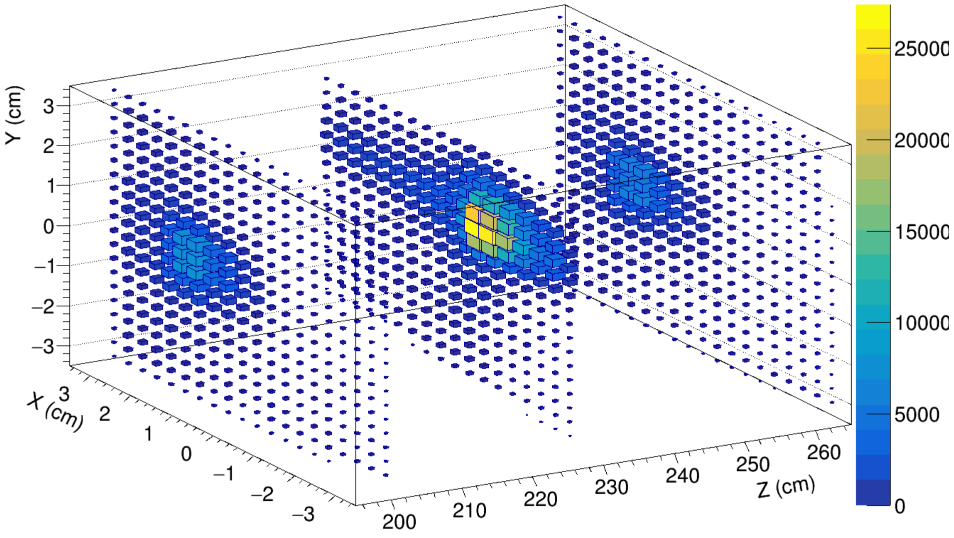

Figure 8.12: Reconstructed hit maps showing the beam spot in both hodoscopes and the STS. No transverse alignment corrections have been applied yet.

where d is the thickness of the material and I_0 is the ionization energy. Multiplying the result of eq. (8.5) on page 119 with the elementary charge yields a mean charge deposition of 5.6 fC and a most probable charge deposition of 3.9 fC in the STS sensor.

Figure 8.14 shows the measured cluster charge distribution of one-strip clusters in ADC units. The 2.7 GeV/c-proton peak is beautifully reconstructed. The energy loss distribution of heavy particles in thin absorbers deviates from a Gaussian because of the possibility of large energy transfers in a single collision [130]. The resulting high-energy tail leads to an asymmetric shape that can be described by a Landau distribution. In order to fit the data

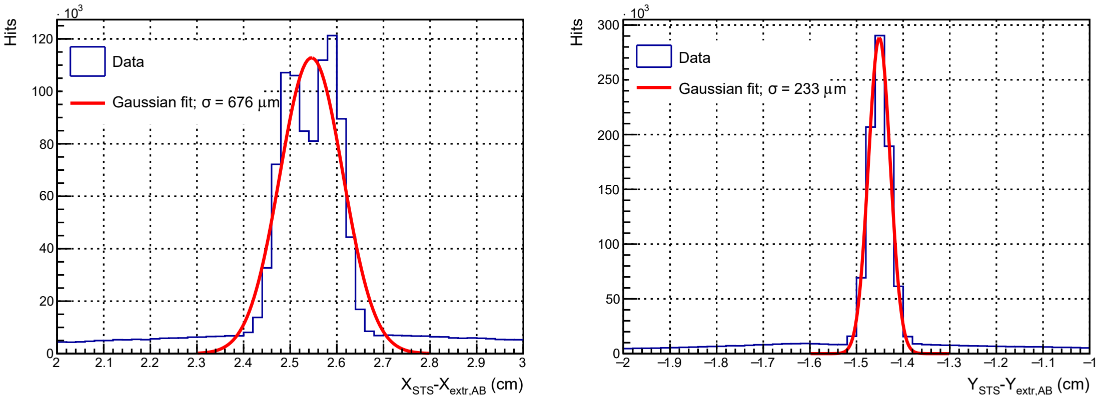

Figure 8.13: Spatial resolution in X and Y extracted from projections of the 2D correlation in Figure 8.11. The resolution is limited by the resolution of the scintillating fiber hodoscopes.

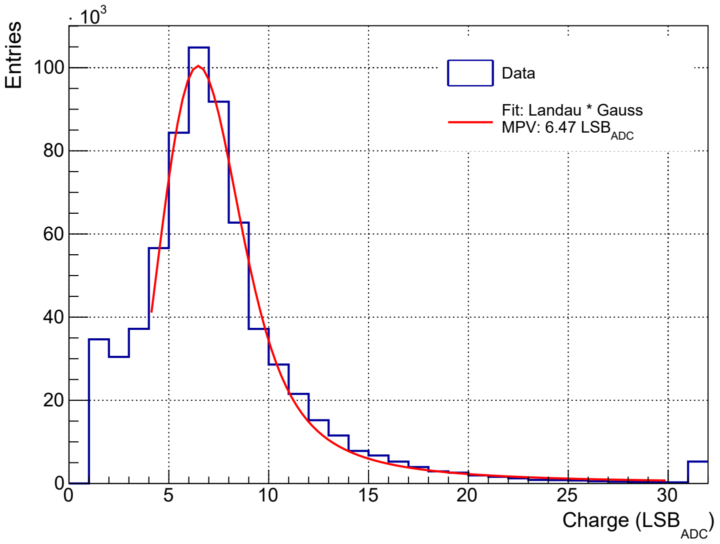

Figure 8.14: Cluster charge distribution of 1-strip clusters in ADC units. A Landau distribution convoluted with a Gaussian describes the data well.

correctly, the Gaussian detector response has to be factored in as well. Hence, a convolution of a Landau distribution with a Gaussian describes the data well, as shown in Figure 8.14. The energy calibration—the conversion from ADC units to actual charge—is performed in detail in Section 8.7.4.

8.7.4 Signal-to-noise ratio

Like in the case of the copper module described in section 7.2.4 on page 105, the energy spectrum shown in Figure 8.14 must be converted from ADC units to charge. The transfer function for the COSY module has been determined at $v_{ref,t} = 58$ for both polarities

$$\text{N: } Q_n\,[\text{ampcal}] = 6.98\left[\frac{\text{ampcal}}{\text{ADC}}\right]\cdot(\text{Peak}\,[\text{ADC}] - 1) + 14.82\,[\text{ampcal}]\,, \tag{8.6}$$

$$\text{P: } Q_p\,[\text{ampcal}] = 7.19\left[\frac{\text{ampcal}}{\text{ADC}}\right]\cdot(\text{Peak}\,[\text{ADC}] - 1) + 13.08\,[\text{ampcal}]\,. \tag{8.7}$$

For this analyis, ASIC 6 (n-side) and ASIC 13 (p-side) are considered, because they are connected to the sensor strips that are in the center of the proton beam. During the beamtime, ASIC 13 was calibrated at $v_{ref,t} = 58$ and ASIC 6 at $v_{ref,t} = 56$. Hence, the offset in ASIC 6 has to be adjusted

$$\text{Offset}_{\text{adj}}\,[\text{ampcal}] = 14.82\,[\text{ampcal}] + 2\left[\text{V}_{\text{ref,t}}\right]\cdot 0.29\left[\frac{\text{ADC}}{\text{V}_{\text{ref,t}}}\right]\cdot 6.98\left[\frac{\text{ampcal}}{\text{ADC}}\right] = 10.77\,.$$

From the Landau–Gaussian fit to the charge distribution, peak positions of 7.573 ± 0.965 ADC and 8.053 ± 1.002 ADC are determined for the n– and p-side, respectively. Hence, the signal charges are

$$Q_n = 6.98\left[\frac{\text{ampcal}}{\text{ADC}}\right]\cdot 7.573\,\text{ADC} + 10.77\,\text{ampcal} = 63.63\,\text{ampcal} = 22\,250\,\text{e}^-\,,$$
$$Q_p = 7.19\left[\frac{\text{ampcal}}{\text{ADC}}\right]\cdot 8.053\,\text{ADC} + 13.08\,\text{ampcal} = 70.98\,\text{ampcal} = 24\,820\,\text{e}^-\,.$$

The charge resolution can be extracted from the sigma of the fits

$$\sigma_{Q,n} = 0.965\,\text{ADC}\cdot 6.98\left[\frac{\text{ampcal}}{\text{ADC}}\right] = 6.74\,\text{ampcal} = 2360\,\text{e}^-\,,$$
$$\sigma_{Q,p} = 1.002\,\text{ADC}\cdot 7.19\left[\frac{\text{ampcal}}{\text{ADC}}\right] = 7.20\,\text{ampcal} = 2520\,\text{e}^-\,.$$

Finally, the SNR can be calculated

$$SNR_n = \frac{22\,250\,\text{e}^-}{1050\,\text{e}^-} \sim 21\,,$$
$$SNR_p = \frac{24\,820\,\text{e}^-}{1100\,\text{e}^-} \sim 23\,.$$

The effect of the SNR on reconstruction efficiency and momentum resolution of the full detector has been studied in [131], using simulations based on a realistic detector response model [132]. There, it has been shown that the system performance deteriorates rapidly for SNR values below 10 and ENC levels above 1500 e$^-$. Clearly, the COSY module performs excellently.

8.7.5 Charge collection efficiency

With the knowledge of the signal charge, the CCE of the module can be estimated. The MPV of created charge by the COSY protons is $35\,090\,\mathrm{e}^- \cdot 0.73 = 25\,620\,\mathrm{e}^-$. Again, this value has to be corrected for capacitive charge sharing with eq. (7.4) on page 108. For the COSY module, the sum of the capacitance of the sensor and the microcable is $C_d = C_{mc} + C_s = 21.95\,\mathrm{pF}$. Hence, $Q_i/Q_s = 0.956$, and thus the expected measured charge is $24\,490\,\mathrm{e}^-$. Comparing this to the average of the signal measurements on the p– and n-side, the CCE is $Q_m/Q_i \sim 96\,\%$. Again, this result should be taken with some caution because the measurements lack statistics and certain behaviors of the ASIC, such as the differences in ADC gain and threshold between the p– and n-side, are not fully understood.

8.8 Summary

In order to test the STS detector in a well-known environment, the STS team scheduled a beamtime at the Cooling Synchrotron at the research center Jülich, Germany, in November 2019. COSY provided a pencil-like monochromatic beam of 2.7 GeV/c protons. The COSY beamtime enabled a first-time evaluation of the full analysis software chain with real data and the evaluation of the full electronic readout chain of STS. The targeted STS system noise of $\sim 1000\,\mathrm{e}^-$ was achieved, in good agreement with theoretical expectations. With only a few unconnected channels (<1 %), some differences among odd/even channels are attributed to the routing of microcables and are subject to ongoing optimizations. Having corrected for jumps in the time offset between the STS and the hodoscopes, an excellent time resolution of a few nanoseconds was demonstrated before correcting for walk.

After finding the best coincidence between the systems based on the time information, the hit maps of the beam particles could be successfully reconstructed in all three systems. The position resolution of a few hundred µm is also in line with expectations, as it is limited by the fiber hodoscope resolution. The charge distributions of 1-strip clusters show a clear separation between noise and the proton signal peak, with an SNR larger 20 for the p– and n-side. The charge collection efficiency was estimated to be ~96 %. Due to intermediate problems with the reconstruction chain and due to time constraints, the hit efficiency and tracking efficiency of the STS module could not be determined. In any case, these figures of merit are better determined with more than one module.

To summarize, the COSY beamtime in 2019 was a success and provided valuable insights into the STS detector performance operated with the full electronic readout chain in a particle beam environment.

9 Conclusion

The ambitious physics goals of the CBM experiment call for unprecedented interaction rates, a novel free-streaming readout concept, and a well thought-out design of the CBM subdetectors. Due to the challenging design of the STS detector modules and the sheer amount of 1200 modules (including spares) to be built, STS module production is distributed to three international production centers: GSI (Darmstadt), KIT (Karlsruhe), and JINR (Dubna, Russia). The Institute for Data Processing and Electronics (IPE) at KIT will assemble 500 STS modules in a three-year production phase from 2021–2023.

The core of this work relates to the functional building block of the STS—the detector module. The main goal was to develop and characterize an alternative module assembly technology based on custom-designed copper microcables connecting the silicon microstrip sensors with the STS-XYTER readout ASIC. A low-mass double-layered copper microcable on the edge of modern fabrication technology was developed and thoroughly characterized.

Based on the copper microcable, a novel high-density interconnection technology has been developed, comprising fine-grain solder paste printing on the microcable and gold stud bumping on the die. The technology combines a high automation capability with good mechanical and electrical properties, therefore representing an interesting technology also for future detector systems. The gold stud–solder interconnection technology has been continually refined in response to encountered challenges. The developed and optimized process steps include the gold stud bumping, solder paste printing, solder paste reflow, microcable–die flip-chip interconnection, underfill application, and die attach. Even for our experienced industrial partners, the fabrication of the fine-pitch microcable proved to be a major challenge. Over the course of several iterations, the microcable design, fabrication process, and laser singulation could be optimized.

Another core part of this work was the development and construction of a fully customized bonding machine for the STS modules in hardware and software. Key features of the machine include four step motors with a sub-micron step resolution, a dual-camera pattern recognition system, a heatable, temperature-controlled bond head and sensor plate, as well as tailor-made mechanical supports for the STS detector modules. The machine can acommodate each of the four sensor sizes employed in the STS and is the foundation for the assembly of full detector modules in the copper technology. A third cornerstone of this work was the testing and characterization of the STS-XYTER2.1 readout ASIC. The STS-XYTER2.1 was extensively characterized with a particular emphasis on the quantitative noise performance of the chip. The main findings include:

- The slow and fast shaper gain are 29 mV fC^{-1}/30 mV fC^{-1} and 46 mV fC^{-1}/49 mV fC^{-1} (e/h), respectively.
- The CSA fast reset works as expected. Fast reset decay times below 20 ns have been measured for electron polarity.
- The ASIC-internal pulse generator expresses excellent linearity (INL = 2.6 mV).
- Thanks to the ability to choose between four different dynamic ranges of the ADC global threshold resolution, the resolution could be improved from ~2000 e$^-$ to 182 e$^-$/161 e$^-$ (e/h).
- The noise dependence on input load capacitance was found to be 21.7 e$^-$/pF and 28.7 e$^-$/pF for electrons and holes, respectively.
- The overall noise level is practically independent of shaper peaking time, a consistent finding for various setups of different input capacitance.

In radiation tests with 50 MeV protons and a TID of 10 kGy with the ASIC in a non-powered state, no indications of damage to the chip and interconnects could be observed.

Based on the aforementioned work, small-scale and full-scale detector modules in the copper technology were built. Small-scale modules comprise one sensor with one copper microcable per sensor side, each connected to a STS-XYTER2.1 readout ASIC, which in turn is wire bonded to a FEB-C. They allow one to accumulate first experience in the full assembly chain, including the ASIC–microcable, chipcable–sensor, and ASIC–FEB bondings, with all the associated gluing and handling steps, all while reducing the usage of resources. For two such modules, a total of 14 out of the 512 channels appeared to be not properly connected, corresponding to a 97.3 % yield. The overall ENC level of individual channels was found to be comparable to the aluminium technology.

Despite the challenges faced during assembly, especially during the die attach, a full module could be built in the copper technology. This module was tested extensively in the laboratory. A bias voltage scan revealed low noise levels below 700 e$^-$, in line with expectations. The channel yield of the module was estimated to be approximately 95 %. Signal measurements with a radioactive ^{241}Am-source allowed us to estimate the signal-to-noise ratio (~ 22) and charge collection efficiency (~ 91 %) of the module. These values give us confidence that STS modules based on the copper technology can achieve a good performance, comparable to the aluminium modules. Due to the more advanced development of the aluminium technology, as well as the slightly increased material budget, capacitance, and stiffness of the copper microcable, the copper technology is only foreseen—if need be—to be installed in the outermost modules of the STS.

A complete detector module consisting of a 6.2 cm × 6.2 cm Hamamatsu sensor connected to 16 STS-XYTER2.1 readout ASICs via 49 cm long aluminium microcables, and two FEBs-8, was subjected to a 2.7 GeV/c proton beam in the course of a beamtime campaign at COSY at the research center Jülich, Germany, in November 2019. The beamtime enabled a first-time evaluation of the full analysis software chain with real data and the evaluation of the full electronic readout chain of STS. The targeted STS system noise of ~1000 e$^-$ was achieved. An excellent time resolution of a few nanoseconds was demonstrated. The hit maps of the beam particles could be successfully reconstructed in the STS and the two reference scintillating fiber hodoscopes. The obtained position resolution of the full system of a few hundred µm is in line with expectations, as it is limited by the fiber hodoscope resolution. The charge distributions of 1-strip clusters show a clear separation between noise and the proton signal peak, with an SNR above 20 for both the p– and n-side. The charge collection efficiency was estimated to be $\sim 96\,\%$.

In summary, this thesis covered a variety of topics surrounding the STS detector module, including the interconnection technologies, the microcables, the readout ASIC, as well as the assembly, characterization, and analysis of full detector modules in the laboratory and in beam tests. Future detector systems can build upon the experiences made in the development of a novel high-density interconnection technology for silicon particle trackers. Valuable experience in module assembly was brought to KIT, which will be immensely helpful for STS series production. The results of the extensive characterization of the STS-XYTER2.1 readout ASIC entered the development of the next and final ASIC revision v2.2. Data analysis of a full STS module in beam brought valuable insight into the system performance under realistic running conditions, essential for understanding the data in more complex particle environments such as mCBM and, of course, the final CBM experiment.

Bibliography

[1] F. Wilczek. “QCD Made Simple”. In: *Physics Today* 53.8 (2000), pp. 22–28. DOI: 10.1063/1.1310117.

[2] A. Deur, S. J. Brodsky, and G. F. de Teramond. “The QCD Running Coupling”. In: *Progress in Particle and Nuclear Physics* 90.5 (2016), pp. 1–74. DOI: 10.1016/j.ppnp.2016.04.003.

[3] P. Skands. “Introduction to QCD”. In: *CERN-PH-TH-* (2013), pp. 341–420. DOI: 10.1142/9789814525220{\textunderscore}0008.

[4] M. Tanabashi et al. “Review of Particle Physics”. In: *Physical Review D* 98.3 (2018), p. 030001. DOI: 10.1103/PhysRevD.98.030001.

[5] D. J. Gross and F. Wilczek. “Ultraviolet Behavior of Non-Abelian Gauge Theories”. In: *Physical Review Letters* 30.26 (1973), pp. 1343–1346. DOI: 10.1103/PhysRevLett.30.1343.

[6] H. D. Politzer. “Reliable Perturbative Results for Strong Interactions?” In: *Physical Review Letters* 30.26 (1973), pp. 1346–1349. DOI: 10.1103/PhysRevLett.30.1346.

[7] S. Sarkar, H. Satz, and B. Sinha, eds. *The physics of the Quark-Gluon Plasma: Introductory lectures.* Vol. 785. Lecture notes in physics. Heidelberg: Springer, 2010. DOI: 10.1007/978-3-642-02286-9.

[8] A. Bazavov et al. “Chiral and deconfinement aspects of the QCD transition”. In: *Physical Review D* 85.5 (2012). DOI: 10.1103/PhysRevD.85.054503.

[9] M. Gyulassy and L. McLerran. “New forms of QCD matter discovered at RHIC”. In: *Nuclear Physics A* 750.1 (2005), pp. 30–63. DOI: 10.1016/j.nuclphysa.2004.10.034.

[10] I. Arsene et al. “Quark–gluon plasma and color glass condensate at RHIC? The perspective from the BRAHMS experiment”. In: *Nuclear Physics A* 757.1-2 (2005), pp. 1–27. DOI: 10.1016/j.nuclphysa.2005.02.130.

[11] B. Abelev et al. “Pion, kaon, and proton production in central Pb-Pb collisions at $\sqrt{s_{NN}} = 2.76$ TeV”. In: *Physical review letters* 109.25 (2012), p. 252301. DOI: 10.1103/PhysRevLett.109.252301.

[12] J. Stachel et al. “Confronting LHC data with the statistical hadronization model”. In: *Journal of Physics: Conference Series* 509.1 (2014), p. 012019. DOI: 10.1088/1742-6596/509/1/012019.

[13] T. Ablyazimov et al. “Challenges in QCD matter physics –The scientific programme of the Compressed Baryonic Matter experiment at FAIR”. In: *The European Physical Journal A* 53.3 (2017), pp. 1–14. DOI: 10.1140/epja/i2017-12248-y.

[14] K. Kashiwa et al. “Critical endpoint in the Polyakov-loop extended NJL model”. In: *Physics Letters B* 662.1 (2008), pp. 26–32. DOI: `10.1016/j.physletb.2008.01.075`.

[15] B. Friman. *The CBM physics book: Compressed baryonic matter in laboratory experiments.* Vol. 814. Lecture notes in physics. Berlin: Springer, 2011. DOI: `10.1007/978-3-642-13293-3`.

[16] Y. Nambu and G. Jona-Lasinio. “Dynamical Model of Elementary Particles Based on an Analogy with Superconductivity. I”. In: *Physical Review* 122.1 (1961), pp. 345–358. DOI: `10.1103/PhysRev.122.345`.

[17] K. Fukushima and T. Hatsuda. “The phase diagram of dense QCD”. In: *Reports on Progress in Physics* 74.1 (2011), p. 014001. DOI: `10.1088/0034-4885/74/1/014001`.

[18] T. Galatyuk. “HADES overview”. In: *Nuclear Physics A* 931 (2014), pp. 41–51. DOI: `10.1016/j.nuclphysa.2014.10.044`.

[19] L. McLerran. “Quarkyonic Matter and the Revised Phase Diagram of QCD”. In: *Nuclear Physics A* 830.1-4 (2009), pp. 709c–712c. DOI: `10.1016/j.nuclphysa.2009.10.063`.

[20] M. G. Alford et al. “Color superconductivity in dense quark matter: Reviews of Modern Physics, 80(4), 1455-1515”. In: *Reviews of Modern Physics* 80.4 (2008), pp. 1455–1515. DOI: `10.1103/REVMODPHYS.80.1455`.

[21] H. Heiselberg. “Phases of dense matter in neutron stars”. In: *Physics Reports* 328.5-6 (2000), pp. 237–327. DOI: `10.1016/S0370-1573(99)00110-6`.

[22] G. Baym et al. “From hadrons to quarks in neutron stars: a review”. In: *Reports on progress in physics. Physical Society (Great Britain)* 81.5 (2018), p. 056902. DOI: `10.1088/1361-6633/aaae14`.

[23] M. Orsaria et al. “Quark deconfinement in high-mass neutron stars”. In: *Physical Review C* 89.1 (2014). DOI: `10.1103/PhysRevC.89.015806`.

[24] G. Baym. “Confinement of quarks in nuclear matter”. In: *Physica A: Statistical Mechanics and its Applications* 96.1-2 (1979), pp. 131–135. DOI: `10.1016/0378-4371(79)90200-0`.

[25] T. Çelik, F. Karsch, and H. Satz. “A percolation approach to strongly interacting matter”. In: *Physics Letters B* 97.1 (1980), pp. 128–130. DOI: `10.1016/0370-2693(80)90564-X`.

[26] H. Satz. “Deconfinement and percolation”. In: *Nuclear Physics A* 642.1-2 (1998), pp. c130–c142. DOI: `10.1016/S0375-9474(98)00508-9`.

[27] Edmond Iancu. *Multiparticle Dynamics in the LHC Era.* 2011.

[28] F. Gelis et al. “The Color Glass Condensate”. In: *Annual Review of Nuclear and Particle Science* 60.1 (2010), pp. 463–489. DOI: `10.1146/annurev.nucl.010909.083629`.

[29] T. Lappi and L. McLerran. “Some features of the glasma”. In: *Nuclear Physics A* 772.3-4 (2006), pp. 200–212. DOI: `10.1016/j.nuclphysa.2006.04.001`.

[30] J. Berges, J.-P. Blaizot, and F. Gelis. “EMMI rapid reaction task force on ‘Thermalization in non-Abelian plasmas’”. In: *Journal of Physics G: Nuclear and Particle Physics* 39.8 (2012), p. 085115. DOI: `10.1088/0954-3899/39/8/085115`.

[31] U. W. Heinz. *Concepts of heavy ion physics: arXiv:hep-ph/0407360*. 2004.

[32] W. Israel and J. M. Stewart. "Transient relativistic thermodynamics and kinetic theory". In: *Annals of Physics* 118.2 (1979), pp. 341–372. DOI: `10.1016/0003-4916(79)90130-1`.

[33] P. Senger. "Exploring Cosmic Matter in the Laboratory—The Compressed Baryonic Matter Experiment at FAIR". In: *Particles* 2.4 (2019), pp. 499–510. DOI: `10.3390/particles2040031`.

[34] W. Henning. "FAIR — An International Accelerator Facility for Research with Ions and Antiprotons". In: *AIP Conference Proceedings*, pp. 3–5. DOI: `10.1063/1.1949487`.

[35] I. C. Arsene et al. "Dynamical phase trajectories for relativistic nuclear collisions". In: *Physical Review C* 75.3 (2007). DOI: `10.1103/PhysRevC.75.034902`.

[36] U. Heinz and R. Snellings. "Collective Flow and Viscosity in Relativistic Heavy-Ion Collisions". In: *Annual Review of Nuclear and Particle Science* 63.1 (2013), pp. 123–151. DOI: `10.1146/annurev-nucl-102212-170540`.

[37] J. Steinheimer et al. "Examination of directed flow as a signal for a phase transition in relativistic nuclear collisions". In: *Physical Review C* 89.5 (2014), p. 054913. DOI: `10.1103/PhysRevC.89.054913`.

[38] P.F Kolb et al. "Elliptic flow at SPS and RHIC: from kinetic transport to hydrodynamics". In: *Physics Letters B* 500.3-4 (2001), pp. 232–240. DOI: `10.1016/S0370-2693(01)00079-X`.

[39] P. M. Hohler and R. Rapp. "Is ϱ–meson melting compatible with chiral restoration?" In: *Physics Letters B* 731 (2014), pp. 103–109. DOI: `10.1016/j.physletb.2014.02.021`.

[40] C. Gale and J. I. Kapusta. "Vector dominance model at finite temperature". In: *Nuclear Physics B* 357.1 (1991), pp. 65–89. DOI: `10.1016/0550-3213(91)90459-B`.

[41] R. Rapp and H. van Hees. "Thermal dileptons as fireball thermometer and chronometer". In: *Physics Letters B* 753 (2016), pp. 586–590. DOI: `10.1016/j.physletb.2015.12.065`.

[42] T. Galatyuk et al. "Thermal dileptons from coarse-grained transport as fireball probes at SIS energies". In: *The European Physical Journal A* 52.5 (2016), p. 586. DOI: `10.1140/epja/i2016-16131-1`.

[43] T. Galatyuk. *Town meeting: Relativistic Heavy Ion Physics: FAIR : CBM*. CERN, 2018.

[44] X. Luo. "Energy Dependence of Moments of Net-Proton and Net-Charge Multiplicity Distributions at STAR". In: *PoS(CPOD2014)019* (2014).

[45] J. Thäder. "Higher Moments of Net-Particle Multiplicity Distributions". In: *Nuclear Physics A* 956 (2016), pp. 320–323. DOI: `10.1016/j.nuclphysa.2016.02.047`.

[46] A. Andronic et al. *Production of light nuclei, hypernuclei and their antiparticles in relativistic nuclear collisions*. Vol. 697. 2011. DOI: `10.1016/j.physletb.2011.01.053`.

[47] R. F. Pierret. *Advanced semiconductor fundamentals*. 2. ed. Vol. 6. Modular series on solid state devices. Upper Saddle River, NJ: Pearson Education, 2003.

[48] S. M. Sze and Kwok K. Ng. *Physics of semiconductor devices*. 3. ed. Hoboken, NJ: Wiley-Interscience, 2007. DOI: `10.1002/0470068329`.

[49] W. Shockley and W. T. Read. “Statistics of the Recombinations of Holes and Electrons: Physical Review, 87(5), 835-842”. In: *Physical Review* 87.5 (1952), pp. 835–842. DOI: `10.1103/PHYSREV.87.835`.

[50] M. Rudan. *Physics of semiconductor devices.* Second edition. Cham: Springer, 2018.

[51] F. Hartmann. *Evolution of Silicon Sensor Technology in Particle Physics.* Second edition. Vol. 275. Springer Tracts in Modern Physics. Cham: Springer, 2017. DOI: `10.1007/978-3-319-64436-3`.

[52] E. A. Burke. “Energy Dependence of Proton-Induced Displacement Damage in Silicon”. In: *IEEE Transactions on Nuclear Science* 33.6 (1986), pp. 1276–1281. DOI: `10.1109/TNS.1986.4334592`.

[53] Griffin, P. J. et al. *SAND92-0094.* 1993.

[54] A.Yu. Konobeyev, Yu.A. Korovin, and V. N. Sosnin. “Neutron displacement cross-sections for structural materials below 800 MeV”. In: *Journal of Nuclear Materials* 186.2 (1992), pp. 117–130. DOI: `10.1016/0022-3115(92)90328-I`.

[55] M. Huhtinen and P. A. and Aarnio. *Estimation of pion induced displacement damage in silicon.* 1993.

[56] M. Huhtinen and P. A. Aarnio. “Pion induced displacement damage in silicon devices”. In: *Nuclear Instruments and Methods in Physics Research Section A: Accelerators, Spectrometers, Detectors and Associated Equipment* 335.3 (1993), pp. 580–582. DOI: `10.1016/0168-9002(93)91246-J`.

[57] G. P. Summers et al. “Damage correlations in semiconductors exposed to gamma, electron and proton radiations”. In: *IEEE Transactions on Nuclear Science* 40.6 (1993), pp. 1372–1379. DOI: `10.1109/23.273529`.

[58] S. R. Messenger et al. “Limits to the application of NIEL for damage correlation”. In: *IEEE Transactions on Nuclear Science* 51.6 (2004), pp. 3201–3206. DOI: `10.1109/TNS.2004.839152`.

[59] M. Huhtinen. “Simulation of non-ionising energy loss and defect formation in silicon”. In: *Nuclear Instruments and Methods in Physics Research Section A: Accelerators, Spectrometers, Detectors and Associated Equipment* 491.1-2 (2002), pp. 194–215. DOI: `10.1016/S0168-9002(02)01227-5`.

[60] H. Spieler. *Semiconductor detector systems.* Reprint. (twice). Vol. 12. Oxford science publications. Oxford: Oxford Univ. Press, 2009.

[61] S. Ramo. “Currents Induced by Electron Motion”. In: *Proceedings of the IRE* 27.9 (1939), pp. 584–585. DOI: `10.1109/JRPROC.1939.228757`.

[62] W.M.C. Sansen and Z. Y. Chang. “Limits of low noise performance of detector readout front ends in CMOS technology”. In: *IEEE Transactions on Circuits and Systems* 37.11 (1990), pp. 1375–1382. DOI: `10.1109/31.62412`.

[63] G. Casse. *Development of p-type detectors for present LHC and luminosity upgrades.* Vol. 579. 2007. DOI: `10.1016/j.nima.2007.05.257`.

[64] P. Holl et al. "A double-sided silicon strip detector with capacitive readout and a new method of integrated bias coupling". In: *IEEE Transactions on Nuclear Science* 36.1 (1989), pp. 251–255. DOI: `10.1109/23.34444`.

[65] P. Weilhammer. "Double-sided Si strip sensors for LEP vertex detectors". In: *Nuclear Instruments and Methods in Physics Research Section A: Accelerators, Spectrometers, Detectors and Associated Equipment* 342.1 (1994), pp. 1–15. DOI: `10.1016/0168-9002(94)91403-6`.

[66] Tetyana Galatyuk. *Future facilities for high-μ_B physics.* Vol. 982. 2019. DOI: `10.1016/j.nuclphysa.2018.11.025`.

[67] A. Malakhov and A. Shabunov. *Technical Design Report for the CBM Superconducting Dipole Magnet.* 2013.

[68] P. Klaus et al. "Status of the vertex detector program of the CBM experiment at FAIR". In: *Nuclear Instruments and Methods in Physics Research Section A: Accelerators, Spectrometers, Detectors and Associated Equipment* 936 (2019), pp. 705–706. DOI: `10.1016/j.nima.2018.09.092`.

[69] J. Heuser et al. *[GSI Report 2013-4] Technical Design Report for the CBM Silicon Tracking System (STS).* 2013.

[70] J. Adamczewski-Musch et al. "The CBM RICH detector". In: *Journal of Instrumentation* 11.05 (2016), pp. C05016–C05016. DOI: `10.1088/1748-0221/11/05/C05016`.

[71] CBM Collaboration. *Technical Design Report for the CBM : Muon Chambers (MuCh).* 2015.

[72] CBM Collaboration. *The Transition Radiation Detector of the CBM Experiment at FAIR : Technical Design Report for the CBM Transition Radiation Detector (TRD).* 2018.

[73] N. Herrmann. *Technical Design Report for the CBM Time-of-Flight System (TOF).* 2014.

[74] F. Guber and I. Selyuzhenkov. *Technical Design Report for the CBM Projectile Spectator Detector (PSD).* 2015.

[75] V. Akishina et al., eds. *FLES - First Level Event Selection Package for the CBM Experiment: Deutsches Elektronen-Synchrotron, DESY, Hamburg.* 2015. DOI: `10.3204/DESY-PROC-2014-05/4`.

[76] J. M. Heuser, U. Frankenfeld and the STS workgroup. *Production Readiness Review for the STS Carbon Fiber Ladders.* 2019.

[77] S. Mehta et al. "STS ladder assembly". In: *CBM Progress Report 2018*, p. 26.

[78] J. M. Heuser and the STS workgroup. *Description of the STS microstrip sensors for series production.* 2019.

[79] STS workgroup. *Production Readiness Review for the Silicon Sensors of the CBM Silicon Tracking System.* Ed. by J. M. Heuser, V. Pugatch, H. R. Schmidt. 2019.

[80] I. Panasenko et al. "Electrical qualification of the microstrip sensors for mSTS". In: *CBM Progress Report 2018.*

[81] E. Lavrik, I. Panasenko, and H. R. Schmidt. *Advanced Methods for the Optical Quality Assurance of Silicon Sensors.* 2019. DOI: `10.1016/j.nima.2018.10.210`.

[82] E. Lavrik et al. “High-precision contactless optical 3D-metrology of silicon sensors”. In: *Nuclear Instruments and Methods in Physics Research Section A: Accelerators, Spectrometers, Detectors and Associated Equipment* 935 (2019), pp. 167–172. DOI: `10.1016/j.nima.2019.04.039`.

[83] D. Pitzl et al. “Type inversion in silicon detectors”. In: *Nuclear Instruments and Methods in Physics Research Section A: Accelerators, Spectrometers, Detectors and Associated Equipment* 311.1-2 (1992), pp. 98–104. DOI: `10.1016/0168-9002(92)90854-W`.

[84] E. Barberis et al. “Capacitances in silicon microstrip detectors”. In: *Nuclear Instruments and Methods in Physics Research Section A: Accelerators, Spectrometers, Detectors and Associated Equipment* 342.1 (1994), pp. 90–95. DOI: `10.1016/0168-9002(94)91414-1`.

[85] R. Sonnenblick et al. “Electrostatic simulations for the design of silicon strip detectors and front-end electronics”. In: *Nuclear Instruments and Methods in Physics Research Section A: Accelerators, Spectrometers, Detectors and Associated Equipment* 310.1-2 (1991), pp. 189–191. DOI: `10.1016/0168-9002(91)91023-O`.

[86] K. Kasinski et al. “STS-XYTER, a high count-rate self-triggering silicon strip detector readout IC for high resolution time and energy measurements”. In: *2014 IEEE Nuclear Science Symposium and Medical Imaging Conference (NSS/MIC).* 2014, pp. 1–6. DOI: `10.1109/NSSMIC.2014.7431048`.

[87] A. S. Brogna et al. “N-XYTER, a CMOS read-out ASIC for high resolution time and amplitude measurements on high rate multi-channel counting mode neutron detectors”. In: *Nuclear Instruments and Methods in Physics Research Section A: Accelerators, Spectrometers, Detectors and Associated Equipment* 568.1 (2006), pp. 301–308. DOI: `10.1016/j.nima.2006.06.001`.

[88] K. Kasinski et al. “Characterization of the STS/MUCH-XYTER2, a 128-channel time and amplitude measurement IC for gas and silicon microstrip sensors”. In: *Nuclear Instruments and Methods in Physics Research Section A: Accelerators, Spectrometers, Detectors and Associated Equipment* 908 (2018), pp. 225–235. DOI: `10.1016/j.nima.2018.08.076`.

[89] K. Kasinski et al. *SMX2 and SMX2.1 Manual v2.0.* 2018.

[90] A.R.Rodriguez, J. Lehnert, O.M. Rodriguez. “ADC response and noise levels in the STS-XYTER v2 ASIC”. In: *CBM Progress Report 2017*, pp. 28–29.

[91] V. M. Borshchov et al. “Towards production of ultra-lightmicrocables for the STS detector modules”. In: *CBM Progress Report 2017*, p. 36.

[92] C. Simons et al. “Assembly of modules for mSTS applying complete quality assurance”. In: *CBM Progress Report 2018*, pp. 16–17.

[93] D. Soyk et al. “Capacitance studies of the CBM STS microcable stack-up”. In: *CBM Progress Report 2016*, pp. 44–45.

[94] C. Simons et al. “Development of a workflow for the CBM-STS module-assembly”. In: p. 38.

[95] C. Simons et al. “Assembly of dummy modules for the STS demonstrator of unit 7”. In: *CBM Progress Report 2016*, p. 48.

[96] STS workgroup. *STS Module and Ladder Assembly.* Ed. by H.R. Schmidt and J.M. Heuser.

[97] P. Koczoń et al. “Irradiation tests on the 1.8 V final prototype LDOs delivered by SCL Chandigarh/India”. In: *CBM Progress Report 2018*, pp. 29–30.

[98] P. Pfistner et al. “Novel production method for large double-sided microstrip detectors of the CBM Silicon Tracking System at FAIR”. In: *Proceedings of Topical Workshop on Electronics for Particle Physics — PoS(TWEPP2018)* (), p. 144. DOI: `10.22323/1.343.0144`.

[99] P. Pfistner et al. “Novel high-density interconnection technology for the CBM Silicon Tracking System”. In: *Journal of Instrumentation* 14.09 (2019), P09027–P09027. DOI: `10.1088/1748-0221/14/09/P09027`.

[100] T. Blank et al. “Investigation on low mass copper flex micro-cables for the STS detector”. In: *CBM Progress Report 2016*, pp. 42–43.

[101] Particle Data Group, https://pdg.lbl.gov/2020/AtomicNuclear Properties/index.html.

[102] T.i Tsuchiya and T. Okuyama. “Ultra-Low CTE Polyimide Film for Flexible Substrates”. In: *AM-FPD 19.* [Japan]: [International Society of Functional Thin Film Materials and Devices], 2019, pp. 1–3. DOI: `10.23919/AM-FPD.2019.8830605`.

[103] G. Qian et al. “Superheat-resistant polyimides with ultra-low coefficients of thermal expansion”. In: *Polymer* 196 (2020), p. 122482. DOI: `10.1016/j.polymer.2020.122482`.

[104] T. Blank et al. “Novel module production methods for the CMS pixel detector, upgrade phase I”. In: *Journal of Instrumentation* 10.02 (2015), p. C02021.

[105] M. Caselle et al. “Low-cost bump-bonding processes for high energy physics pixel detectors”. In: *Journal of Instrumentation* 11.01 (2016), p. C01050.

[106] R. Durairaj et al. “Rheological characterisation and printing performance of Sn/Ag/Cu solder pastes”. In: *Materials and Design* 30.9 (2009), pp. 3812–3818.

[107] A.E. Marks. “Characterisation of lead-free solder pastes and their correlation with the stencil printing process performance”. PhD thesis. University of Greenwich, UK.

[108] R. Aspandiar. *Voids in solder joints.* 2018.

[109] K. Rajewski. “SMT process recommendations. Defect minimization methods for a no-clean SMT process”. In: *IEEE Technical Applications Conference and Workshops. Northcon/95. Conference Record.* 1995, pp. 354–362. DOI: `10.1109/NORTHC.1995.485096`.

[110] C.Y. Huang. “The investigation of the capillary flow of underfill materials”. In: *Microelectronics International* 19.1 (2002), pp. 23–29. DOI: `10.1108/13565360210417754`.

[111] Patrick Pfistner et al. “Automated assembly of large double-sided microstrip detectors of the CBM Silicon Tracking System at FAIR”. In: *Proceedings of Topical Workshop on Electronics for Particle Physics — PoS(TWEPP2019)* 2019 (), p. 72. DOI: `10.22323/1.370.0072`.

[112] A. Rodriguez Rodriguez. “The CBM Silicon Tracking System front-end electronics: from bare ASIC to detector characterization, commissioning and performance”. PhD thesis. Frankfurt am Main: Johann-Wolfgang Goethe - Universität, 2019.

[113] A. Toia et al. “Performance studies of prototype STS modules”. In: *CBM Progress Report 2020*, pp. 32–35.

[114] K. Kasinski et al. “Towards STS-XYTERv2.1, a new STS/MUCH prototype readout chip”. In: *CBM Progress Report 2017*, pp. 30–31.

[115] W. Zubrzycka et al. “STS-XYTER2.1, a revised prototype readout ASIC for the STS and MUCHdetectors”. In: *CBM Progress Report 2018*, p. 14.

[116] F. Switakowski. *AMC FMC carrier kintex (AFCK), https://ohwr.org/project/afck.*

[117] W. M. Zabołotny et al. “Design of versatile ASIC and protocol tester for CBM readout system”. In: *Journal of Instrumentation* 12.02 (2017), pp. C02060–C02060. DOI: `10.1088/1748-0221/12/02/C02060`.

[118] C. Ghabrous Larrea et al. “IPbus: a flexible Ethernet-based control system for xTCA hardware”. In: *Journal of Instrumentation* 10.02 (2015), pp. C02019–C02019. DOI: `10.1088/1748-0221/10/02/C02019`.

[119] W. Zubrzycka and K. Kasinski. “Noise considerations for the STS/MUCH readout ASIC”. In: *CBM Progress Report 2017*, pp. 32–33.

[120] Z. Y. Chang and W. M. C. Sansen. *Low-Noise Wide-Band Amplifiers in Bipolar and CMOS Technologies.* Vol. 117. The Springer International Series in Engineering and Computer Science, VLSI, Computer Architecture and Digital Signal Processing. Boston, MA: Springer, 1991. DOI: `10.1007/978-1-4757-2126-3`.

[121] I. Panasenko et al. “Microcable quality assurance: capacitance measurements”. In: *CBM Progress Report 2016*, p. 46.

[122] I. Panasenko et al. “Sensor quality assurance: capacitance measurements”. In: *CBM Progress Report 2016*, pp. 24–25.

[123] F. Guarino, C. Hauviller, M. Tavlet. *Compilation of radiation damage test data: Part IV: Adhesives.* Ed. by CERN. 2001.

[124] C. J. Schmidt, J. Lehnert, and K. Kasinski. “New and final ASIC STS-XYTER Version 2.2”. In: *CBM Progress Report 2020*, p. 28.

[125] F. J. Ramírez-Jiménez. “X-Ray Spectroscopy with PIN diodes”. In: *AIP Conference Proceedings* 857.1 (2006), pp. 121–133. DOI: `10.1063/1.2359248`.

[126] L. C. Longoria et al. “Analytical peak fitting for gamma-ray spectrum analysis with Ge detectors”. In: *Nuclear Instruments and Methods in Physics Research, Section A* 299.1-3 (1990), pp. 308–312.

[127] STS workgroup. *STS Module and Ladder EDR: Questions & Answers.* Ed. by H.R. Schmidt and J.M. Heuser.

[128] J. Lehnert and D. Gottschalk. “Development and test of the CBM Common Readout Board (CROB)”. In: *CBM Progress Report 2017*, p. 45.

[129] D. E. Groom and S. R. Klein. “Passage of particles through matter”. In: *The European Physical Journal C* 15.1-4 (2000), pp. 163–173. DOI: `10.1007/BF02683419`.

[130] William R. Leo. *Techniques for Nuclear and Particle Physics Experiments: A How-to Approach.* Second Revised Edition. Berlin and Heidelberg: Springer, 1994. DOI: `10.1007/978-3-642-57920-2`.

[131] H. Malygina. “Hit reconstruction for the Silicon Tracking System of the CBM experiment”. PhD thesis. Frankfurt am Main: Johann-Wolfgang Goethe - Universität, 2018.

[132] H. Malygina and V. Friese. “A precision device needs precise simulation: Software description of the CBM Silicon Tracking System”. In: *Journal of Physics: Conference Series* 898.GSI-2017-01795 (2017). DOI: `10.1088/1742-6596/898/4/042022`.

List of Acronyms

A

ADC **A**nalog-to-**D**igital **C**onverter

ASIC **A**pplication **S**pecific **I**ntegrated **C**ircuit

C

C-ROB **C**ommon **R**ead**O**ut **B**oard

CBM **C**ompressed **B**aryonic **M**atter

CCE **C**harge **C**ollection **E**fficiency

CGC **C**olor **G**lass **C**ondensate

CiS Forschungsinstitut für Mikrosensorik GmbH

CMOS **C**omplemtary **M**etal **O**xide **S**emiconductor

COSY **CO**oling **SY**nchrotronn

CSA **C**harge **S**ensitive **A**mplifier

CTE **C**oefficient of **T**hermal **E**xpansion

Cu_KIT_202 Copper module with 20 cm microcables and 62 mm × 22 mm sensor

D

DAQ **D**ata **A**c**Q**uisition

DPB **D**ata **P**rocessing **B**oard

E

ENC **E**quivalent **N**oise **C**harge

EOS **E**quation **O**f **S**tate

ESD **E**lectro**S**tatic **D**ischarge

F

FAIR **F**acility for **A**ntiproton and **I**on **R**esearch

FEB **F**ront **E**nd **B**oard

FEB-8 Front End Board hosting eight STS-XYTER

FEB-B Front End Board type B used for testing of the STS-XYTER2

FEB-C Front End Board type C used for testing of the STS-XYTER2.1

FLES **F**irst **L**evel **E**vent **S**elector

FPGA **F**ield **P**rogrammable **G**ate **A**rray

G

GBT **G**iga**B**it **T**ransceiver

GSI **G**esellschaft für **S**chwer**I**onenforschung

H

HADES **H**igh **A**cceptance **D**i-**E**lectron **S**pectrometer

HEP **H**igh **E**nergy **P**hysics

HIC **H**eavy **I**on **C**ollision

HV **H**igh **V**oltage

I

IFED Register controlling the feedback resistance in the STS-XYTER

INL **I**ntegral **N**on-**L**inearity

L

LDO **L**ow **D**rop**O**ut voltage regulator

LHC **L**arge **H**adron **C**ollider

LQCD **L**attice **QCD**

LV **L**ow **V**oltage

M

mCBM **m**ini **CBM** experiment

MIP **M**inimum **I**onizing **P**article

MPV **M**ost **P**robable **V**alue

MUCH **MU**on **CH**amber

MVD **M**icro **V**ertex **D**etector

N

n3NJL SU(**3**) **N**ambu-**J**ona-**L**asinio model with repulsive vector interactions

NIEL **N**on-**I**onizing **E**nergy **L**oss

P

PCB **P**rinted **C**ircuit **B**oard

PI **P**oly**I**mide

PSC **P**olarity **S**election **C**ircuit

PSD **P**rojectile **S**pectator **D**etector

PT **P**hase **T**ransition

Q

QCD **Q**uantum **C**hromo**D**ynamics

QGP **Q**uark **G**luon **P**lasma

R

RHIC **R**elativistic **H**eavy **I**on **C**ollider

RICH **R**ing **I**maging **C**herenkov

S

SCL **S**emi**C**onductor **L**aboratory in Chandigarh, India

SEU **S**ingle **E**vent **U**pset

SIS **S**chwer-**I**onen-**S**ynchrotron

SNR **S**ignal-to-**N**oise **R**atio

SPS **S**uper **P**roton **S**ynchrotron

STAR **S**olenoidal **T**racker **A**t **R**HIC

STS **S**ilicon **T**racking **S**ystem

STS-XYTER STS readout ASIC

T

TAB **T**ape **A**utomated **B**onding

TID **T**otal **I**onizing **D**ose

TOF **T**ime **O**f **F**light

TRD **T**ransition **R**adiation **D**etector

V

$\mathbf{v_{ref,t}}$ Register controlling the ADC threshold